Title
Cardiomyocyte Regeneration and the Potential Role of Neonatal Systemic Factors

Author
Nguyen, Ngoc

Publication Date
2021

Peer reviewed|Thesis/dissertation

UNIVERSITY OF CALIFORNIA

Los Angeles

Cardiomyocyte Regeneration and the Potential Role of Neonatal Systemic Factors

A dissertation submitted in partial satisfaction of the

requirements for the degree Doctor of Philosophy

in Molecular, Cellular, and Integrative Physiology

by

Ngoc Bao Nguyen

2021

ABSTRACT OF THE DISSERTATION

Cardiomyocyte Regeneration and the Potential Role of Neonatal Systemic Factors

by

Ngoc Bao Nguyen

Doctor of Philosophy in Molecular, Cellular, and Integrative Physiology

University of California, Los Angeles, 2021

Professor Reza Ardehali, Chair

There are tremendous health and financial burdens attributed to cardiovascular disease. The most common type, known as ischemic heart disease, is due to plaque buildup within the coronary arteries that supply the myocardium with oxygen and nutrients. Reduction or blockage of blood flow can lead to irreversible loss of cardiomyocytes, the main building blocks of the heart, with estimates placing that loss to upward of a billion cells. Despite medical therapy, the majority of patients eventually progress to heart failure, in which the main challenge for the development of therapeutic strategies is the limited regenerative ability of the adult mammalian heart. Our dissertation takes a multi-faceted approach in understanding cardiac regeneration and exploring whether neonatal systemic factors could be the gateway to a new therapy for ischemic heart disease. We report the development of a multi-colored mouse reporter system that enables deeper understanding of the cellular mechanisms driving early cardiac tissue formation. We apply a bioengineering approach to develop biodegradable and biocompatible nanoparticles as a new tool for clonal expansion analysis of cardiac cells. And lastly, we examined the proteomic profile of neonatal plasma in order to identify potential “pro-youthful” factors that may prevent irreversible

myocardial damage. We hope that our body of work pushes forward the field of cardiac regeneration and sets the stage for the development of therapeutic interventions to prevent the progression to heart failure after an acute myocardial infarction.

The dissertation of Ngoc Bao Nguyen is approved.

James N. Weiss

Thomas M. Vondriska

Xia Yang

Jason Ernst

Reza Ardehali, Committee Chair

University of California, Los Angeles

2021

TABLE OF CONTENTS

LIST OF FIGURES

LIST OF TABLES

LIST OF ACRONYMS

CMs	cardiomyocytes
CVD	cardiovascular disease
ECs	endothelial cells
EF	ejection fraction
FACS	fluorescence activated cell sorting
HUVECs	human umbilical vein endothelial cells
I/R	ischemia-reperfusion
iTRAQ	isobaric tag for relative and absolute quantitation
LAD	left anterior descending artery
LV	left ventricle
MI	myocardial infarction
NP	nanoparticle
NRVMs	neonatal rat ventricular myocytes
OH-Tam	hydroxytamoxifen
PBS	phosphate buffered saline

ACKNOWLEDGEMENTS

There is an expression that begins “It takes a village…” and that cannot be truer when it comes to the individuals that deserve recognition for their contribution to my development as a scientist. First, I would like to thank the members of my PhD Committee, for whom I am extremely grateful and honored to have. Dr. Reza Ardehali, for providing me with the opportunity to be part of his lab both as a Sarnoff Fellow and a graduate student. I have learned so much and am not too surprised that the road has led me back again to research. Dr. James Weiss, who is now retired but kind enough to continue serving on his last student committee, for his calm wisdom and always having a grasp of the broader picture. Dr. Thomas Vondriska, from whom I learned the tricks and skills of grant writing and who has always supported my learning by offering the entirety of his resources. Dr. Jason Ernst, for his expertise in bioinformatics that was critical for publishing our Rainbow paper and for all of his advice in solving our sequencing analysis questions. And finally, Dr. Xia Yang, whose expertise in network biology and bioinformatics have provided us with better tools and knowledge to dig deeper into our datasets for meaningful results. Second, I would like to acknowledge the past and present members of the Ardehali lab, who have been the best colleagues and friends that I could have asked for. I could not have made it without you guys – especially Arash and Shuin for being my sounding block and for our tennis/hiking adventures. Third, I want to acknowledge the Sarnoff Fellowship for having such a pivotal influence in my career. I am grateful for the opportunity to be a part of a network of great scientists and role models. And to my former research advisors Drs. Rong Tian, Mei Speer, and Cecilia Giachelli for igniting my love of research and curiosity for science. I have also been lucky to have support from fellowships that have greatly reduced the financial burden of graduate training. And finally, but most importantly, to my family and friends, who have always been by my side and supported all the endeavors that I have undertaken. None of this is meaningful nor possible without you.

CURRICULUM VITAE

EDUCATION

University of Washington School of Medicine, Seattle, WA 08/2013 – present
Doctor of Medicine

University of California, Los Angeles, CA 09/2017 – anticipated 03/2021
Doctor of Philosophy in Molecular, Cellular, and Integrative Physiology

University of Washington, Seattle, WA 09/2005 – 03/2010
Bachelor of Science in Bioengineering, Department of Engineering Honors

PUBLICATION

1. **Nguyen NB**, Zhao P, Pezhouman A, Park S, Qiao R, Pelligrini M, Horvath S, Ardehali R. Protective effects of neonatal plasma in cardiac ischemia-reperfusion injury. In preparation.

2. Pezhouman A*, Engel LJ*, **Nguyen NB***, Skelton RJP, Gilmore WB, Sahoo D, Zhao P, Elliott DA, Ardehali R. Isolation of heart field specific cardiomyocytes provides a platform for safe cardiac regenerative therapy. *Cardiovascular Research*. Accepted March 2021.

3. Lu A, Fei Z, Haghani A, et al. Universal DNA methylation age across mammalian tissues. Submitted January 2021.

4. **Nguyen NB**, Fernandez GE, Ding Y, Hsiai T, Ardehali R. *In vivo* clonal analysis of cardiomyocytes. *Methods in Molecular Biology*. January 2021. PMID: 32857378

5. Pezhouman A, **Nguyen NB**, Shevtsov A, Qiao R, Ardehali R. *In Vitro* Generation of Heart Field Specific Cardiomyocytes. *Methods in Molecular Biology.* Submitted September 2020.

6. He L, **Nguyen NB**, Ardehali R, Zhou B. Heart regeneration by endogenous stem cells and cardiomyocyte proliferation: controversy, fallacy, and progress. *Circulation*. March 2020. PMID: 32687441

7. **Nguyen NB***, Chen CH*, Zhang Y, Zhao P, Wu B, Ardehali R. Tissue-specific targeting of poly(lactic-co-glycolic acid) nanoparticles. *Nanomedicine: Nanotechnology, Biology, and Medicine*. July 2019. PMID: 31026512; PMCID: PMC6599573.

8. Park S, **Nguyen NB**, Pezhouman A, Ardehali R. Cardiac fibrosis: potential therapeutic targets. *Translational Research.* July 2019. PMID: 30930180; PMCID: PMC6545256

9. Sereti KI*, **Nguyen NB***, Kamran P*, Zhao P, Ranjbarvaziri S, Park S, Sabri S, Engel JL, Sung K, Kulkami RP, Ding Y, Hsiai TK, Plath K, Ernst J, Sahoo D, Mikkola H, Iruela-Arispe L, Ardehali R. Clonal analysis of cardiomyocyte generation during development and injury. *Nature Communications*. February 2018. PMID: 29467410; PMCID: PMC5821855.

10. Ranjbarvaziri S, Park S, **Nguyen NB**, Gilmore WB, Ardehali R. Generation of Nkx2-5/CreER transgenic mice for inducible Cre expression in developing hearts. *Genesis*. August 2017. PMID: 28589709; PMCID: PMC5568924

11. Lin ME, Chen T, Wallingford MC, **Nguyen NB**, Yamada S, Sawangmake C, Zhang J, Speer MY, Giachelli CM. Runx2 Deletion in Smooth Muscle Cells Inhibits Vascular Osteochondrogenesis and Calcification but not Atherosclerotic Lesion Formation. Sep 2016, *Cardiovascular Research*. PMID: 27671804; PMCID: PMC5079276

12. **Nguyen NB**, Naik V, and Speer MY. Diabetes mellitus accelerates cartilaginous metaplasia and calcification in atherosclerotic vessels of LDLr mutant mice. March 2013, *Cardiovascular Pathology*. PMID: 22818582; PMCID: PMC3481013

13. Naik V, Leaf EM, Hu JH, Yang HY, **Nguyen NB**, Giachelli CM, Speer MY. Sources of cells that contribute to atherosclerotic intimal calcification: an in vivo genetic fate mapping study. May 2012, *Cardiovascular Research*. PMID: 22436847; PMCID: PMC3353803

* These authors contributed equally

FELLOWSHIP SUPPORT

Ruth L. Kirschstein Predoctoral F31 Individual NRSA 09/2018-present
"Protective effects of neonatal plasma in ischemic heart disease"
This project aims to understand the protective effects of neonatal plasma after ischemia-reperfusion injury

UCLA Ursula Mandel Graduate Fellowship 09/2018-09/2019
This fellowship provides stipend support for doctoral students in fields related to medicine

American Heart Association Predoctoral Fellowship 07/2018-09/2018
"Protective effects of neonatal plasma in ischemic heart disease"
This project aims to understand the protective effects of neonatal plasma after ischemia-reperfusion injury

UCLA Jennifer S. Buchwald Graduate Fellowship in Physiology 09/2017-09/2018
This endowment provides financial support toward tuition and fees for graduate students, preferably women or minorities, in their first year in the Department of Physiology

CHAPTER 1: INTRODUCTION

1.1. BACKGROUND

1.1.1. Ischemic heart disease and ischemia-reperfusion injury

Cardiovascular disease (CVD) is the leading cause of morbidity and mortality worldwide, accounting for an estimated 17.9 million deaths annually[1-3]. The most common type of CVD, known as ischemic heart disease, is due to plaque buildup within the coronary arteries that supply the myocardium with oxygen and nutrients. Reduction or blockage of blood flow through the coronaries during myocardial infarction (MI) leads to a dramatic and irreversible loss of cardiomyocytes, with estimates placing that loss to upward of a billion cells[4]. Due to the limited regenerative capacity of the heart, the remaining cardiomyocytes are unable to remuscularize and restore lost cells. The mainstay of clinical therapy is early and successful cardiac reperfusion through thrombolytic therapy[5, 6], percutaneous coronary intervention[7, 8], or coronary artery bypass grafting[9], all of which helps to preserve cardiac function and limit irreversible damage to the myocardium. However, restoration of coronary blood flow after a period of ischemia may precipitate further damage, termed ischemia-reperfusion (I/R) injury. While medications such as β-blockers, ACE-inhibitors, and aldosterone antagonists can slow the decline in heart function, majority of patients eventually develop heart failure, requiring mechanical circulatory support or heart transplantation[10, 11]. Thus, there is a great need to develop therapies that can prevent, reduce, or even reverse myocardial damage and the progression to heart failure.

1.1.2. Emerging therapeutic strategies for ischemic heart disease

Within the past few decades, several therapeutic strategies for regenerating cardiac muscle have been investigated (**Figure 1.1**). The first of these are the use of either endogenous or exogenous stem cells that can be differentiated into cardiomyocytes as an approach to increase cell number. The use of endogenous stem cells was deemed a possibility after a groundbreaking study by Orlic et al. showed that c-Kit+ hematopoietic cells from murine bone marrow can

differentiate into smooth muscle, endothelial, and cardiomyocytes to regenerate injured myocardium[12]. They also provided additional evidence of human BMCs differentiating into cardiomyocytes during adulthood[13]. This finding sparked a series of studies and clinical trials looking into the potential of bone marrow as a source of circulating cardiac progenitors[14-17]. Despite its initial promise, later studies were unable to show the ability of c-Kit+ cells to differentiate into cardiomyocytes[18-21], which shifted the field toward the use of exogenous stem cells for transplantation. In this application, stem cells are differentiated into cardiac progenitors and/or cardiomyocytes *in vitro* prior to being transplanted to the heart, where they would ideally engraft and replace damaged tissue[22]. Methods have been developed to differentiate different types of stem cells such as human embryonic and induced pluripotent stem cells using various small molecule inhibitors[23-31]. While studies have shown promise of this approach in improving cardiac function and decreasing infarct scar sizes, many challenges remain in this field, including: (1) determining the appropriate cell type that can effectively engraft with host tissue, (2) improving survival and retention of the transplanted cells, (3) determining optimal time for cell transplantation after cardiac injury, and (4) development of clinically-relevant large animal models that can closely recapitulate human physiology[32-36].

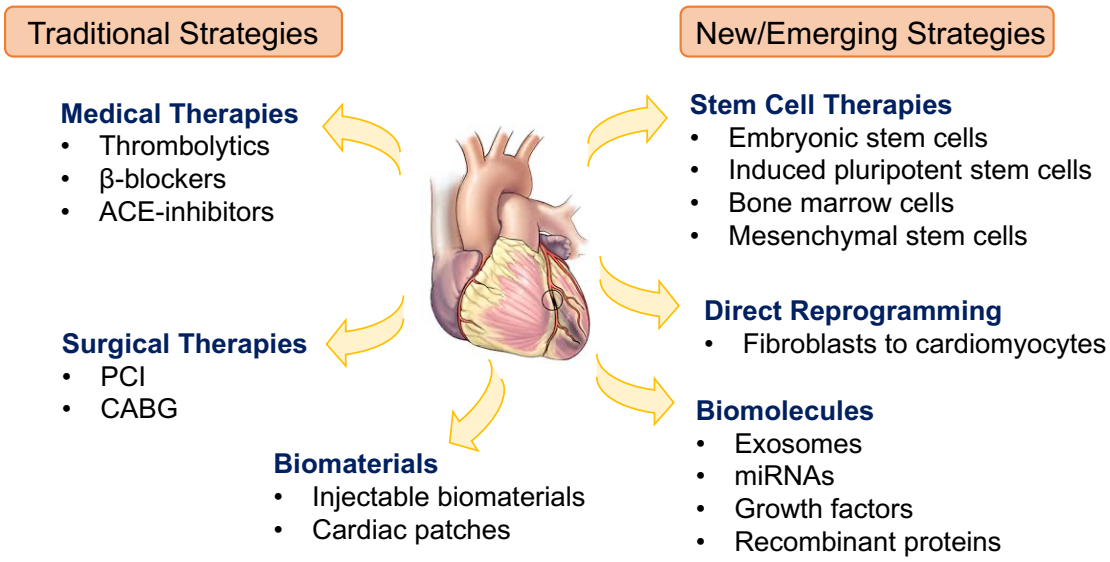

Figure 1.1: Traditional and emerging therapeutic strategies for ischemic heart disease.

A second category is the direct reprogramming of fibroblasts into cardiomyocytes[37-43]. This approach harnesses the abundance of endogenous fibroblasts in the heart to regenerate lost cardiomyocytes after ischemic injury. The advantage to this is two-fold, in that fibroblasts are one of the key players contributing to scar formation and thus, reprogramming them into cardiomyocytes would also reduce their contribution to extracellular matrix deposition. Prior to the discovery by Yamanaka of epigenetic reprogramming using 4 factors (Oct3/4, Sox2, c-Myc, and Klf4), adult somatic cells, such as fibroblasts, were thought to be terminally differentiated and unable to revert to a pluripotent state[44]. Investigators utilized this potential to design a therapy that would address cardiac repair from two directions. While this approach was shown to achieve beneficial results, it suffers from similar challenges to exogenous stem cell transplantation. There is a need to better determine whether the heterogeneity of fibroblast subtypes renders one more effective than the other in being reprogrammed and whether different combinations of transcription factors could be used to generate more mature cardiomyocytes from both *in vitro* and *in vivo* reprogramming[43].

Another strategy, and one relevant to this dissertation, is looking at ways to stimulate endogenous cardiomyocyte proliferation. Years of research has led to a general consensus that the existence of endogenous cardiac stem cells is very limited and unlikely to be a source of cardiac regeneration[45-47]. The focus has now shifted toward finding ways to induce the proliferation of existing cardiomyocytes through the use of various biomolecules such as exosomes[48-52], miRNAs[53-55], cell cycle regulators[56-61], and growth factors[62-64]. Several lines of evidence have made this a promising approach to pursue. Studies have shown that fetal and neonatal cardiomyocytes are capable of proliferation[65-67] and even adult hearts of newt[68] and zebrafish[69] have the ability to fully regenerate after injury. Early studies looking at ^{14}C incorporation show that adult human cardiomyocytes renew at a rate of 1% annually at the age of 20, with gradual decrease to 0.3% at the age of 75[70]. While this may be a low turnover rate and reflects the challenge of therapies for ischemic heart disease, it also highlights the innate

proliferative potential of cardiomyocytes waiting to be unlocked and manipulated for cardiac regeneration. One limitation linked with understanding the proliferative potential of cardiomyocytes is the development of tools that enables accurate and direct measurement of cellular proliferation. **Chapters 2** and **3** of this dissertation highlights our work in generating and characterizing the "Rainbow" mouse model and development of a targeted nanoparticle delivery system to better understand the cellular mechanisms driving cardiogenesis and for clonal expansion analysis of cardiac cell types.

A final approach relating to this dissertation stems from early studies using parabiosis as a model to examine effects of shared circulation. Parabiosis, derived from the Greek words, "*para*" - "alongside" and "*bios*" - "life", is a surgical method invented in 1864 by Paul Bert[71]. This procedure involves joining two mice at the midline such that they develop vascular anastomoses, creating a shared circulation over time. This technique was first applied to the study of aging by Clive McCay at Cornell University in the 1950s, in which he joined an old and young mouse together and found that cartilage of the old mouse appeared much younger than expected[72]. However, the use of this approach lost its popularity by the 1970s due to high mortality rates likely arising from immune rejection[71]. It took until the early 2000s for parabiosis to be revived, when investigators at Stanford applied this approach to study the influence of systemic factors on aged progenitor cells within skeletal muscle and liver[73]. The renewed interest in parabiosis has led researchers to explore whether young blood may contain "pro-regenerative" factors that contribute to partial reversion of age-related diseases[73-77]. In **Chapter 4** of this dissertation, we apply concepts of this approach with current understanding of cardiac development to examine whether young systemic factors could be the gateway to a new therapy for ischemic heart disease.

1.2. OBJECTIVES OF DISSERTATION

This dissertation takes a multi-faceted approach in understanding and developing tools to examine the proliferative potential of cardiomyocytes and to uncover whether neonatal plasma

contain “pro-youthful” factors that promote regeneration of the heart after ischemic injury. **Chapter 2** covers our work in understanding the proliferative potential of cardiomyocytes during early mouse heart development as well as response after injury using a multi-colored genetic labeling mouse reporter system called Rainbow. We used this system to directly quantify the clonal expansion of cardiac progenitors and cardiomyocytes to better understand the cellular mechanisms driving early cardiac tissue formation. **Chapter 3** describes our work using a bioengineering approach to develop biodegradable and biocompatible nanoparticles that are loaded with tamoxifen and capable of activating Cre recombinase in a targeted manner. We show that this system provides a versatile, time-, and cost-effective strategy of inducing recombination events in a ubiquitous Cre system for biomedical applications such as clonal expansion analysis of cardiac cells. **Chapter 4** addresses ongoing work examining whether neonatal plasma contains “pro-youthful” factors that may prevent irreversible myocardial damage in adult mice after ischemia-reperfusion injury. We focus on neonatal plasma from mice 2-5 days old during which the heart’s ability to fully regenerate after injury is well recognized. And finally, **Chapter 5** closes with a summary of our significant findings and the future direction of this research. It is our hope that this body of work pushes forward the field of cardiac regeneration and sets the stage for the development of therapeutic interventions to prevent the progression to heart failure after an acute myocardial infarction, which would greatly relieve the financial and health burden that it holds worldwide.

CHAPTER 2: ANALYSIS OF CARDIOMYOCYTE CLONAL EXPANSION DURING MOUSE HEART DEVELOPMENT AND INJURY

Konstantina-Ioanna Sereti*, Ngoc B Nguyen*, Paniz Kamran*, Peng Zhao, Sara Ranjbarvaziri, Shuin Park, Shan Sabri, James L Engel, Kevin Sung, Rajan P Kulkarni, Yichen Ding, Tzung K Hsiai, Kathrin Plath, Jason Ernst, Debashis Sahoo, Hanna K A Mikkola, M Luisa Iruela-Arispe, Reza Ardehali

This research was originally published by Sereti, Nguyen, and Kamran *et al*. Clonal analysis of cardiomyocyte generation during development and injury. *Nature Communications*. Feb 2018. PMID: 29467410

2.1. ABSTRACT

The cellular mechanisms driving cardiac tissue formation remain poorly understood, largely due to the structural and functional complexity of the heart. It is unclear whether newly generated myocytes originate from cardiac stem/progenitor cells or from pre-existing cardiomyocytes that re-enter the cell cycle. Here, we identify the source of new cardiomyocytes during mouse development and after injury. Our findings suggest that cardiac progenitors maintain proliferative potential and are the main source of cardiomyocytes during development; however, the onset of αMHC expression leads to reduced cycling capacity. Single-cell RNA sequencing reveals a proliferative, “progenitor-like” population abundant in early embryonic stages that decreases to minimal levels postnatally. Furthermore, cardiac injury by ligation of the left anterior descending artery was found to activate cardiomyocyte proliferation in neonatal but not adult mice. Our data suggest that clonal dominance of differentiating progenitors mediates cardiac development, while a distinct subpopulation of cardiomyocytes may have the potential for limited proliferation during late embryonic development and shortly after birth.

2.2. INTRODUCTION

The adult mammalian heart has long been considered a non-regenerative organ and cardiomyocytes (CMs), the building blocks of the heart, as terminally differentiated cells. A number of studies have demonstrated a low rate of CM turnover[70, 78, 79] while others have suggested the existence of distinct CM populations that maintain their proliferative capacity throughout adulthood[80]. Remarkably, zebrafish[69] as well as neonatal mice[67, 69] can efficiently regenerate their hearts in response to injury. A recent study by Sturzu *et al*[81] reported the ability of the embryonic heart to rapidly restore extensive tissue loss through robust CM proliferation. However, the proliferative capacity of CMs during development and after birth remains an area of controversy. It is unclear whether newly generated myocytes originate from cardiac stem/progenitor cells or from pre-existing CMs that re-enter the cell cycle. In this paper, we utilized the Rainbow system to perform clonal analysis of CMs during development and after injury to obtain a better mechanistic understanding of cardiac growth. The Rainbow system marks a small number of cells and their progeny with a distinct fluorescent protein, allowing retrospective tracing of cellular expansion through easily identifiable clones *in vivo*.

Through single cell lineage tracing, we find that cardiomyocytes marked as early as embryonic day 9.5 (E9.5) have the capacity to form large clones both *in vitro* and *in vivo*, however, this capacity is substantially reduced by E12.5. Additionally, our data suggest the possibility that cardiovascular progenitors contribute to the majority of cardiac growth during embryonic development and that their maturation occurs with gradual expression of cardiac-specific markers concomitant with their decreasing proliferative capacity. Single cell RNA sequencing supports the notion of heterogeneity in the proliferative capacity of αMHC-expressing CMs over time. Within the early stages of cardiac development, we observe a potential reduction in developmental growth signals and a shift toward pathways involved in heart contraction and cellular respiration. Taken together, our study provides important insights into the source of CMs and the characteristics of progenitor cells both during development and after injury.

2.3. METHODS

2.3.1. Generation of Rainbow mice

All animal studies were performed according to the guidelines of UCLA's animal care and use committee and the National Institutes of Health Guide for the Care and Use of Laboratory Animals. Both male and female mice were used for all animal experiments within this study. Rainbow transgenic mice (mixed background) were initially generated in I. Weissman's lab at Stanford University. Rainbow mice carry a cassette of 4 fluorescent proteins, inserted in the Rosa26 locus under the control of CAG promoter. Upon Cre mediated recombination the default GFP expression is replaced by random expression of one of three other fluorescent proteins: mCherry, mOrange and mCerulean. *Mesp1*^{Cre} (Mesp1$^{tm2(cre)Ysa}$), *Rosa26*^{CreER} (B6.129-Gt (ROSA) 26Sortm1$^{(cre/ESR1)Tyj}$/J), *Nkx2.5*^{Cre} (Nkx2-5$^{tm1(cre)Rjs}$), *αMHC*^{Cre} (Myh6-cre), *αMHC*^{CreER} (Myh11-cre/ESR1), *βactin*^{CreER} (ACTB-cre/Esr1) and *Wt1*^{CreER} (Wt1$^{tm2(cre/ERT2)Wtp}$/J) transgenic mice were obtained from The Jackson Laboratory. All animals were housed in sterile micro insulators and given water and rodent chow ad libitum.

2.3.2. Generation of Nkx2.5^{CreER} knock-in mice

The targeting vector Nkx2.5IRESCre was a generous gift from Dr. Richard P. Harvey's laboratory[82]. It consisted of a gene cassette (IRES-Cre) carrying an internal ribosome entry site linked to the gene encoding a nuclear-localizing recombinase, which was inserted into the 3' untranslated region (utr) of Nkx2.5. This vector was further modified by replacing the Cre sequence with the CreERT2 in-frame downstream of the IRES site. The resulting construction vector included a hygromycin resistance gene cassette (pgk-HYGRO-pA) flanked by yeast flp recombinase target (frt) sites inserted downstream of IRES-CreERT2. The correct targeting occurred at a frequency of ~ 1 in 7 (22/152) hygromycin-resistant ES cell clones. Blastocyst injection of a single correctly targeted clone produced chimeric animals that passed the modified allele through the germline, generating the strain Nkx2.5IRESCreERT2HYGRO. To remove the

pgk-HYGRO-pA cassette, founders were crossed with transgenic mice expressing the Flp recombinase gene (FLP1) in germ cells. Founders of this new strain (Nkx2-5IRESCreERT2) were backcrossed onto C57BL/6 mice. Validation and genotyping of mice were performed by Southern analysis and PCR. The resulting transgenic mice were fully viable, healthy and fertile over several generations. In addition, this strategy resulted in preservation of the endogenous NKX2.5 loci, thereby avoiding haplo-insufficiency, which may inadvertently influence developmental studies. Mice were genotyped by PCR using Cre-for (5'-TGCAGGTTTTGAGCCCTAAC-3') and Cre-rev (5'-CGAGAATGACTTCCCTGTCC-3'). It should be noted that not all mouse models in this study were knock-ins, posing the potential limitations associated with use of ectopically-inserted promoters.

2.3.3. Hydroxytamoxifen preparation and administration

Tamoxifen (Sigma) was dissolved by sonication in corn oil to a stock concentration of 20 mg/ml. 4-Hydroxytamoxifen (4OH-TM, Sigma) was first dissolved in absolute ethanol to a concentration of 100 mg/ml followed by dilution with corn oil to a final stock concentration of 10 mg/ml. Extensive sonication and vortexing were used. Stock solutions were used within 3 days of preparation. To achieve minimum recombination, one dose of tamoxifen was given through intraperitoneal injection. Pregnant females from αMHC^{CreER} ; $R26^{VT2/GK}$ and $\beta actin^{CreER}$; $R26^{VT2/GK}$ crossings received 4 mg and 350 µg of tamoxifen respectively. Postnatally, αMHC^{CreER} ; $R26^{VT2/GK}$ mice received 10 µg and $\beta actin^{CreER}$; $R26^{VT2/GK}$ mice received 1 µg of tamoxifen. Pregnant females from $Wt1^{CreER}$; $R26^{VT2/GK}$ and $Rosa26^{CreER}$; $R26^{VT2/GK}$ crossings were treated with 4 mg of 4OH-TM and 350 µg of tamoxifen respectively.

2.3.4. Measurement of tamoxifen levels in serum

Serum levels of 4-hydroxytamoxifen were measured after administration of tamoxifen to pregnant female mice. An aliquot of mouse plasma was mixed with acetonitrile in a 1:2 ratio, and

then vortexed and centrifuged at 12500 rpm for 8 min. The supernatant was removed and evaporated under a stream of argon. The resulting residue was reconstituted by vortex mixing with methanol. The solution was transferred to a tapered, limited volume autosampler vial which was then analyzed. The chromatographic separations were performed on a 10cm x 300 μm Higgins Targa C18 3 μm column maintained at 50°C. A 1 μl aliquot of sample was injected into the column and eluted with a 1-95% B gradient over 5 min where solution A was aqueous formic acid (0.1%) and solution B was acetonitrile. The eluate was analyzed and detected by tandem mass spectrometry (MS/MS) using selected reaction monitoring of the transition m/z 388.24->71.9 with a Waters Micromass LCT Premier MS that allows accurate detection to the 1 nM range.

2.3.5. Tissue harvest and processing for histological analysis

Hearts were harvested, perfused and incubated in 4 % (vol/vol) paraformaldehyde (PFA) (4-6 hours and 12-18 hours at 4 °C for embryonic and postnatal hearts respectively) followed by incubation in 30 % (wt/vol) sucrose in PBS at 4 °C for 12-18 hours. The samples were removed from the sucrose solution and tissue blocks were prepared by embedding in Tissue Tek O.C.T. (Sakura Finetek). Blocks were kept frozen in -80°C. Frozen whole heart blocks were sectioned into 7-10 μm thick sections with a Leica CM1860 cryostat and mounted on Superfrost/Plus slides (Fisherbrand). Fluorescent images were acquired with Leica fluorescence inverted microscope DMI6000B equipped with an EL6000 light source and LED 590 (585/40), GFP ET (470/40), A4 ET (360/40), CFP ET (436/20) S-Gold (575/30) filter cubes. Confocal images were obtained with a Leica TCS-SP5 AOBS confocal multiphoton microscope. Lasers 458nm, 488nm (495nm and 514nm), and 594nm were utilized to excite mCerulean, GFP, mOrange and mCherry respectively.

2.3.6. Immunofluorescence

Sections were washed three times with PBS followed by antigen retrieval in 0.25% Triton for 10 minutes. Samples were blocked for 1 hour in 10 % goat serum followed by incubation with

primary antibodies for 2 hours at room temperature (RT). Antibodies against α-sarcomeric Actinin (1/400, Sigma, A7811), α-smooth muscle actin (1/100, Sigma, A2547), CD31 (1/100, Abcam, ab28364), DDR2 (1/100, R&D, MAB25381), WT1 (1/100, Abcam, ab89901) and PDGFRα (1/100, Santa Cruz, sc338) were used. Alexa fluor 647 secondary antibodies were used (1:100, Invitrogen) for 1 hour at RT. Co-localization of proteins with Rainbow-labelled clones was obtained through confocal z-stack analysis. WGA (1/500, Invitrogen) staining was performed for 1 hour at RT. For co-localization purposes, blue pseudocolor was assigned to all clones analyzed in this manuscript.

2.3.7. In vitro *clonal analysis*

Pregnant female mice were sacrificed by isofluorane anesthetic overdose followed by cervical dislocation. The uterus containing E10.5 embryos was removed through an incision at the lower abdomen and was placed in sterile PBS supplemented with anti-biotic and anti-mycotic agents (PBS-AB/AM) at 37°C. Embryos were dissected out of the uterus and their hearts were harvested under a dissection microscope. Hearts were rinsed with PBS-AB/AM (37°C) and digested in 0.2% (v/v) Collagenase type I solution for one hour at 37°C. Following digestion cells were collected by centrifugation (3 min, 3000 rpm) and resuspended in DMEM supplemented with 10% FBS. Cells were counted using a hemocytometer and plated onto 12-well culture dishes at a density of 500,000 cells / dish. Cells were maintained at 37°C in 6% CO_2 for 120 hours. Images of single cells labeled with a Rainbow color were acquired with a Leica fluorescence microscope every 8 hours. The feature “mark and find” of the Leica AF6000 software was used to ensure precise repositioning of defined positions within the culture dish.

2.3.8. In vivo *clonal analysis*

The offspring of crossings between *R26*$^{VT2/GK}$ and *Mesp1*^{Cre}, *Nkx2.5*^{Cre} or *αMHC*^{Cre} were analyzed at P1, P14 and P21 (n=4 for each). To determine clonal expansion in *αMHC*^{CreER} ;

R26$^{VT2/GK}$ and *βactin*^{CreER} ; *R26*$^{VT2/GK}$ mice, tamoxifen was administered at E12.5 and E9.5 respectively and animals were analyzed at P2, P7, P15 and P30. In a second set of experiments, tamoxifen was administered at E12.5, P2, P7 and P15 and analysis was performed at P30. For experiments with *Wt1*^{CreER} ; *R26*$^{VT2/GK}$ mice 4OH-TM was administered at E9.5 and analysis was performed at P0. Pregnant females from *Rosa26*^{CreER} ; *R26*$^{VT2/GK}$ crossings received tamoxifen at E7.5 and were analyzed at P2. For each mouse strain and time-point n=6.

Images were processed with the Leica AF6000 software. Two-dimensional images of every 10 sections of the whole tissue were obtained for each time-point and experimental condition. Sections were stained with WGA to identify cell boundaries (Supplementary Figure 13). To specifically distinguish CM clones, sections were stained with α-sarcomeric actinin and co-localization of actinin with each clone was verified. Quantification of clone number and size was performed by manual counting of the number of single color clusters and the cells within each cluster. Samples identity was hidden from the operator in order to perform quantifications in a blinded fashion.

2.3.9. Clearing of P2 mouse hearts using CLARITY for 3D quantification of clone volumes

P2 mouse hearts were rinsed in PBS and then placed in 4% paraformaldehyde (Electron Microscopy Sciences) at room temperature for 4 hours. The tissues were then rinsed in PBS and transferred to a 4% acrylamide solution (Bio-Rad) along with 0.5% w/v of the photoinitiator 2,2'-Azobis[2-(2-imidazolin-2-yl)propane]dihydrochloride (VA-044, Wako Chemicals USA) and incubated overnight at 4°C. To initiate polymerization, tissues were incubated in the same solution at 37°C for 3 hours. After polymerization, the tissues were rinsed with PBS and then placed into a solution of 8% w/v sodium dodecyl sulfate (Sigma Aldrich) and 1.25% w/v boric acid (Fisher), pH 8.5 at 37°C until cleared. Tissues were transferred to PBS for one day to remove residual SDS and stored in refractive index matching solution (RIMS) until imaging. The RIMS formulation is as follows: to make 30 mL RIMS, dissolve 40 grams of Histodenz (Sigma) in 0.02M Phosphate buffer

(Sigma) with 0.05% w/v sodium azide (Sigma) and syringe filter through a 0.2 mm filter. The tissues can be stored at room temperature in RIMS until ready for imaging.

2.3.10. 3D imaging and reconstruction

Light-sheet fluorescent imaging was carried out on a system previously developed[83]. A diode-pumped solid-state laser containing 4 wavelengths of 405 nm, 473 nm, 532 nm and 589 nm (LMM-GB1, Laserglow Technologies, Toronto, Canada) was used as the illumination source. The laser beam was first expanded from its initial diameter of 2 mm to 10 mm using a 5x achromatic beam expander (GBE05-A, Thorlabs Inc, New Jersey, USA). Then the expanded beam was focused by a plano-convex cylindrical lens (= 50 mm, LJ1695RM-A, Thorlabs Inc, New Jersey, USA) and was then reshaped by a group of achromatic doublets (AC254-060-A, AC254-100-A, Thorlabs, New Jersey, USA). After passing through an f = 150 mm lens, a laser-sheet 40 mm wide and 17 µm thick (Full width at half maximum value) was generated to optically section the entire heart sample. The detection path including an objective lens (2X/0.06, Nikon), a tube lens (ITL 200, Nikon) and switchable optical filters (Semrock, New York, USA) was placed orthogonal to the illumination path for collecting the fluorescence signals. A scientific CMOS (ORCA-Flash4.0 V2, Hamamatsu, Japan) was mounted at the terminal to record the digitalized images with a high frame rate. Samples were mounted into a borosilicate glass tubing and placed on a motorized translational stage. The sample and its holder were immersed in a chamber filled with 99.5% glycerol. Illumination and detection were computer-controlled. Horizontal stripe shadow artifacts were removed from light sheet images in the Fast Fourier Transform (FFT) image of each plane by masking the frequency of the stripes near the Y axis using FIJI ImageJ software[84]. The images of serial sections were then assembled into a z-stack and processed. The contrast was adjusted and adjacent sections were automatically aligned using the StackReg plugin in Rigid Body mode[85]. A 3D volume of the aligned z-stack was rendered using Imaris x64 *ver. 7.7.1 (Bitplane AG, Zurich). Single clones were selected using the Isosurface function of Imaris.

2.3.11. Neuregulin treatment

Recombination was induced at P15. Starting at P20 *αMHC*^{CreER} ; *R26*$^{VT2/GK}$ mice received daily injections of Neuregulin (2.5 µg/mouse, NRG1, R&D) or control BSA (0.1%) for 9 days. Analysis was performed at P29 (control n=3, NRG1 n=4). Animals received BSA or NRG1 in a non-randomized manner.

2.3.12. BrdU pulse and chase experiments

Dames carrying *αMHC-GFP* embryos at E9.5 or E12.5 and P1 neonates were administered 0.1mg BrdU/g body weight of BrdU (BD Biosciences, 550891). Three hours post injection, hearts were collected and digested in collagenase type II (2600 U/ml) for 30 minutes at 37°C and washed with 1 ml FACS Buffer. Cells were centrifuged and supernatant removed. BrdU staining was performed according to manufacturer's protocol (BD Pharmingen, 552598) and cells were FACS analyzed using BD LSRFortessa™ Cell Analyzer Systems.

2.3.13. Single cell RNA sequencing using Fluidigm C1 platform

αMHC-GFP mouse hearts at E9.5, E12.5, and P1 were harvested and digested for FACS sorting. Hearts were digested in either 0.2% (v/v) Collagenase type I solution for 30 min at 37ºC (E9.5 and E12.5) or with Liberase Blendzyme TH and TM (Roche) in Medium 199 with DNAase I and polaxamer for 1 hour at 37°C (P1). P1 samples were passed through a 70µm cell strainer (BD Falcon) before centrifugation at 450 × g for 5 min, supernatant aspirated, and pellet resuspended in FACS buffer. Single-cell RNA sequencing using the C1 Fluidigm platform was performed by the Genomics Core at Cedars-Sinai Medical Center. Cells were sorted directly into C1 Suspension Reagent to obtain a range of 200-260 cells/µl and 6-8µl of cell suspension were loaded according to the manufacturer's protocol on a primed C1 Single Cells AutoPrep Medium IFC microfluidic chip. The chip was run on a Fluidigm C1 instrument and images of all 96 capture sites were taken on a Leica DMi8 Fluorescent Microscope at 100X and 200X magnification. Lysis,

reverse transcription, and PCR was then performed using the Fluidigm 'mRNA Seq: RT + Amp (1772x/1773x)' script and commercially available kits from Life Technologies (Life Technologies Superscript II reverse transcriptase) and Clonetech (dSMART-Seq V4 Kit) according to manufacturer's instructions. Amplified cDNA was harvested in a total of 13 µl of C1 Harvesting Reagent and quantified on an Agilent Bioanalyzer. Sequencing was performed on the NextSeq on a 1 x 75 high output flow cell following the NextSeq denature and dilute guide (Protocol A: Standard Normalization Method).

2.3.14. Single cell RNA sequencing analysis

RNASeq data was mapped with OLego version 1.1.5[86] and normalized by using TPM (Transcripts per millions) analysis as shown in Supplement Figure 14f. Total number of reads mapped to a known transcript annotation was estimated using featurecCounts version v1.5.0-p2[87]. Expression levels for each transcript were determined by normalizing the counts returned by featureCounts using custom Perl scripts. Normalized expression levels for each transcript were determined by transforming the raw expression counts to TPM following log2 scaling. Total number of reads mapped to the genome showed a bimodal distribution. This bimodal distribution separated high quality data and low quality data. We performed StepMiner[88] analysis to determine a threshold to identify cells with high quality data. All the cells with low quality data were removed from subsequent analysis. Clustering was performed using standard hierarchical agglomerative approach using Euclidian distance as a metric for complete linkage (Figure 5b and Supplement Figure 14f, R package `hclust`).

t-SNE and differential gene expression analyses were performed as follows. Raw count matrices were generated using featureCounts and normalized by the number of mapped reads in log space (ln(mapped_reads/10,000+1)). We filtered to exclude low-quality cells with <2000 expressed genes (64 cells) and lowly expressed genes that are expressed in less than 3 cells (9714 genes) from all downstream analyses. This results in a normalized expression matrix of

13623 genes among 122 cells (Extended Figure 14a). Cells were projected onto a 2D embedding using t-Distributed Stochastic Neighbor Embedding (t-SNE, perplexity set to 27) with cell loadings associated to 30 principal components utilizing all expressed genes as input (Figure 5a, R packages 'irlba' and 'Rtsne'). Cell cluster assignments were computed using K-means clustering with k=4 (Figure 5d). The number of K-means clusters was determined by computing the sum of squared error (SSE) for k=1…15 and observing an 'elbow' where the estimated number of clusters is observed. We implemented a negative binomial generalized linear model to identify differentially expressed genes enriched in each cluster. Genes satisfying an abs(log(average expression difference))>0.5 and P-value<0.01 were considered statistically significant. Gene Ontology (GO) enrichments among cluster enriched, differential genes were computed using Metascape (http://www.metascape.org) (Figure 5e). RStudio (https://www.rstudio.com/) was used to run custom R scripts to perform the analyses described above. Generally, ggplot2 and pheatmap packages were used to generate data graphs.

2.3.15. Myocardial infarction model

βactin^{CreER} ; *R26*$^{VT2/GK}$, *αMHC*^{CreER} ; *R26*$^{VT2/GK}$, and *Nkx2.5*^{CreER} ; *R26*$^{VT2/GK}$ mice received tamoxifen one day prior to surgery. All surgical procedures were performed by a single, experienced surgeon, blinded to the identity of the mice. Myocardial infarction was generated via permanent ligation of the left anterior descending artery (LAD). Neonatal mice (P1) (n=3) were anesthetized in an isofluorane chamber (3% isofluorane) and placed on an ice bed for the entire procedure. An incision was performed at the fourth intercostal space and LAD was permanently ligated with an 8-0 suture. The chest wall was sutured with a 6-0 prolene suture and the skin wound was closed using a surgical skin adhesive. Following the procedure mice were placed under a heat lamp until recovery. Adult mice (8 weeks old) (n=5) were anesthetized by intraperitoneal injection of ketamine (100mg/kg) and xylazine (10mg/kg). Animals were ventilated with oxygen-enriched room air during the entire procedure. Left thoracotomy was performed

through an incision between the fourth and fifth intercostal muscles followed by removal of the pericardium. An 8-0 silk suture was used to permanently ligate the LAD. Post-operative discomfort was treated with buprenorphine (0.03-0.06 mg/kg). Sham-operated mice were submitted to the same procedure lacking the LAD ligation (n=3 for P1 and 8 weeks old). Animals were submitted to sham operation or LAD ligation in a non-randomized manner.

2.3.16. Statistical analysis

Student unpaired t test and one-way ANOVA were used for statistical analysis. All data are presented as mean ± SEM. Two-sample Kolmogorov–Smirnov distribution test was used to determine significance for two-dimensional clonal size analysis and three-dimensional clonal volumes analysis. A probability value $p \leq 0.05$ was considered statistically significant. All analyses were performed with GraphPad Prism 5.04.

2.3.17. Data availability

The authors declare that all data supporting the findings of this study are available within the article and its supplementary information files or from the corresponding author upon reasonable request. Sequencing and code sources that support the findings of this study have been deposited in GitHub at the following link: https://github.com/ShanSabri/Rainbow-analysis. Raw data files have been deposited in the GEO database under accession code GSE10842.

2.4. RESULTS

2.4.1. Rainbow provides a direct tool for clonal expansion analyses

To study clonal distribution in the heart, we used Rainbow (hereafter termed *R26*$^{VT2/GK}$) mice (**Figure 2.1a**) to generate transgenic lines expressing Cre under the control of early cardiovascular progenitor transcription factors, Mesp1[89] and Nkx2.5[90]. In this system, Cre-mediated recombination of paired lox P sites results in permanent expression of a distinct

fluorescent protein in cells expressing Mesp1 or Nkx2.5 and their subsequent progeny (**Figure 2.2a-f**). There was equal expression of all three fluorescent proteins (mCherry, mOrange, and Cerulean) in the labeled hearts (**Figure 2.1b-c**). We analyzed heart sections at embryonic day 14.5 (E14.5), and postnatal days 1 and 21 (P1, P21) for the presence of clonal patterns. We identified single-color multicellular clusters evident across the atria and ventricles, indicating possible clonal areas (**Figure 2.2b,e** and Supplementary Movie 1). We expected some uniformity to the clonal regions in terms of shape and size, however, hearts from different animals displayed unique clonal distribution patterns. To examine the proliferative behavior of CMs during development, we utilized $\alpha MHC^{Cre};R26^{VT2/GK}$ mice (**Figure 2.2g-i**)[91]. αMHC-derived CMs appeared mainly as singletons, illustrated by the mosaic appearance of Rainbow colors and the limited occurrence of single-colored clones (**Figure 2.2h** inset). These data suggest that cardiac progenitors marked by the expression of Mesp1 and Nkx2.5 are potential sources of substantial CM expansion, whereas αMHC-expressing CMs possess low cycling capacity, even during embryonic development.

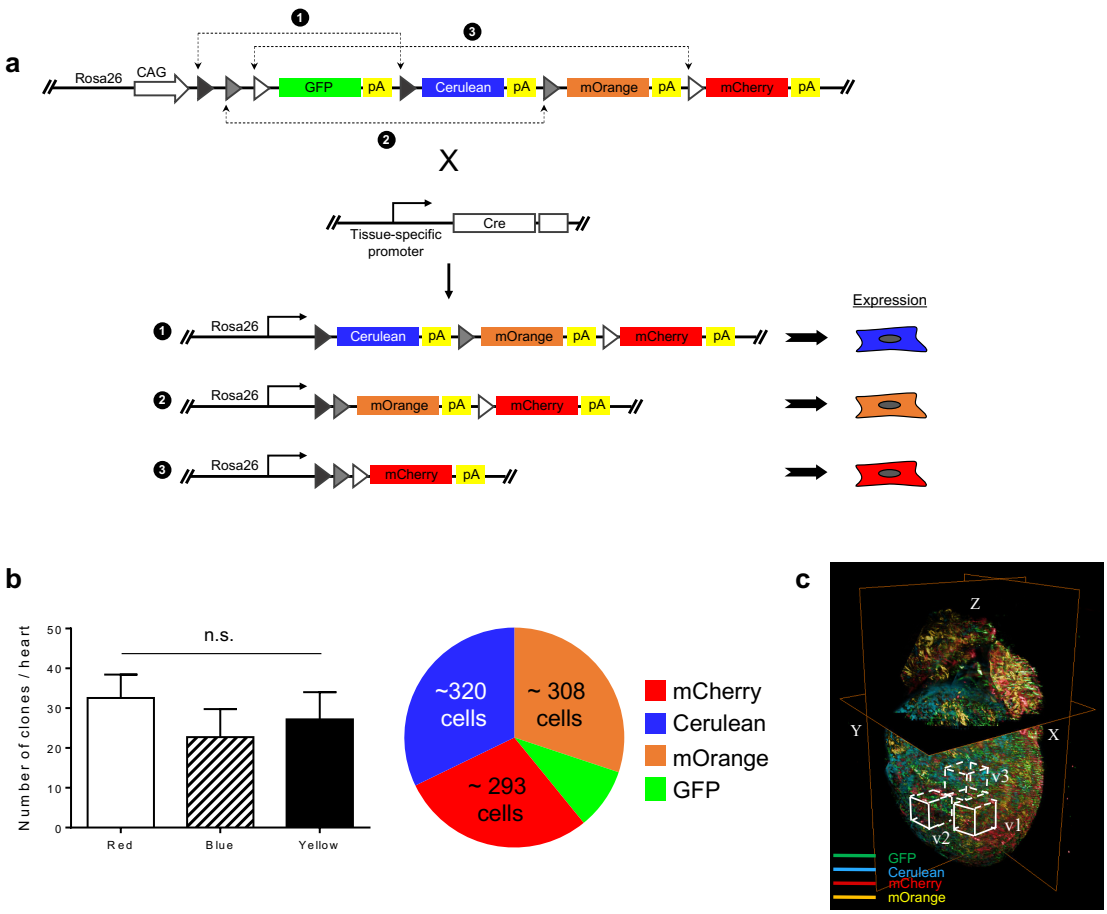

Figure 2.1: The Rainbow model provides a precise, direct method to study clonal expansion of cardiac progenitors and CMs within the developing heart.
a, Schematic representation of the Rainbow reporter system. Expression of Cre induces random recombination between mutated paired lox P sites (black, grey and white triangles) leading to expression of Cerulean, mOrange and mCherry respectively. **b-c,** Quantification of the number of labeled clones per heart from 2D sections of P1 hearts (n=11) **(b)** and 3D imaging of a *αMHC*^{Cre} ; *R26*$^{VT2/GK}$ P1 heart **(c)** demonstrates equal representation of Cerulean, mOrange and mCherry. All measurements shown are depicted as mean ± SEM.

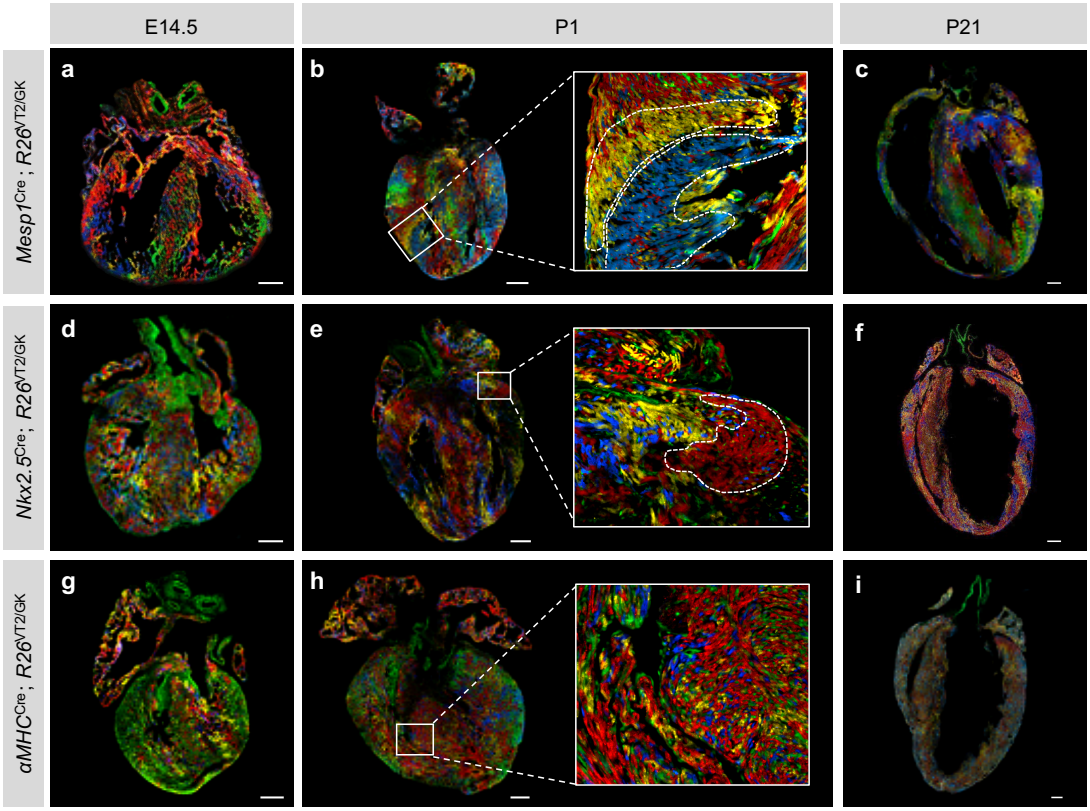

Figure 2.2: Evidence of clonal expansion during cardiac development.
Representative fluorescent microscope images of **a-c**, *Mesp1*^{Cre};*R26*$^{VT2/GK}$, **d-f**, *Nkx2.5*^{Cre};*R26*$^{VT2/GK}$ and **g-i**, *αMHC*^{Cre};*R26*$^{VT2/GK}$ longitudinal hearts sections at E14.5, P1, and P21 respectively (n=4). Insets show a higher magnification of boxed areas. Putative clonal areas are traced by a dotted line. Scale bar 500 μm (**c, f, i**), all others 50 μm.

2.4.2. Single cell lineage tracing of early cardiac progenitors

However, the use of Rainbow with a non-inducible Cre model results in high levels of recombination. To exclude the possibility that the observed single-color cell clusters could result from random recombination and expression of the same fluorescent protein within neighboring cells, we used tamoxifen-inducible Cre lines that permit tight spatiotemporal control on recombination events (**Figure 2.5a-f**). We initially investigated the clonal expansion of all cell types in the heart (including CMs and stem/progenitor cells) by crossing *R26*$^{VT2/GK}$ mice with mice harboring an inducible Cre under the control of a βactin (*βactin*^{CreER}) promoter (**Figure 2.5a, d**). Since βactin is ubiquitously expressed, fluorescent labeling could occur in any cell. We achieved single cell labeling through titration of tamoxifen dosage (**Figure 2.3a**), which generated easily

identifiable clones for analysis (**Figure 2.3b**). Twenty-four hours following administration, serum tamoxifen level was reduced to negligible levels, ensuring tight temporal control of recombination (**Figure 2.3c**). In addition, there were no significant differences in the distribution or frequency of the three fluorescent proteins in single cell labeling and accordingly, there was comparable prevalence of the different colored clones at time of analysis.

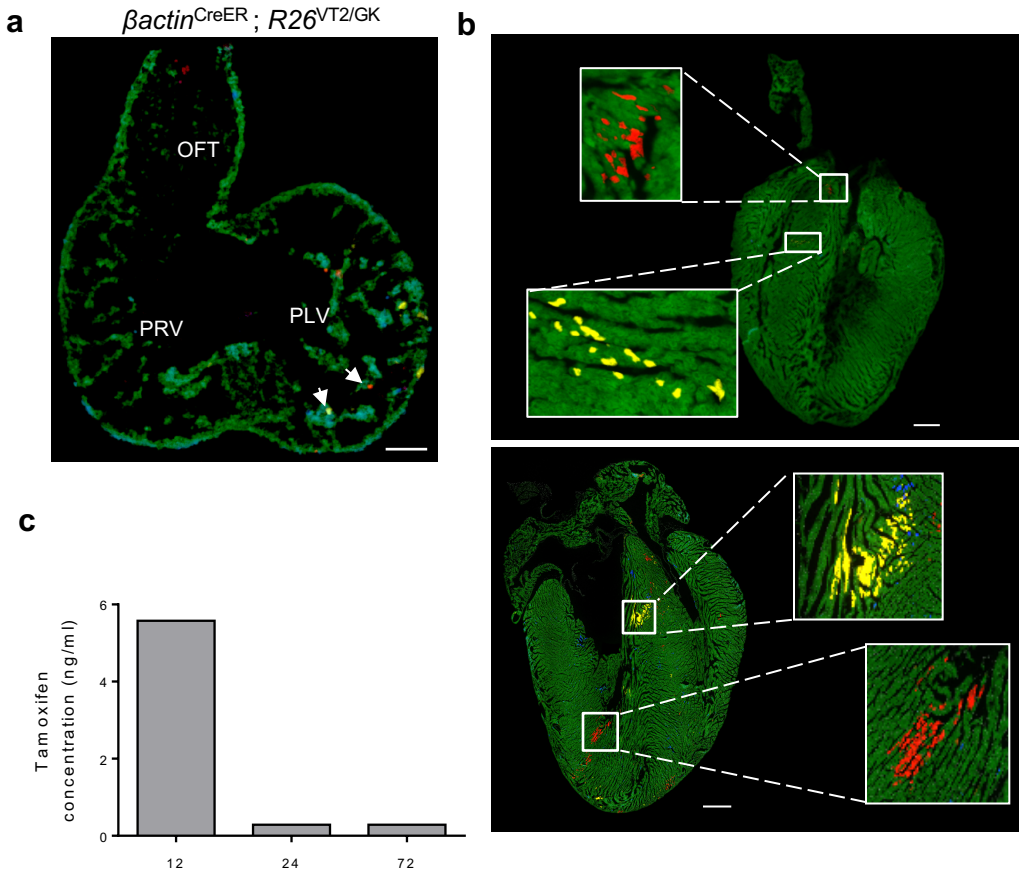

Figure 2.3: Single low dose of tamoxifen induces rare recombination events.
a, Representative fluorescent microscope image of *βactin*^{CreER} ; *R26*$^{VT2/GK}$ E10.5 hearts 24hrs post tamoxifen administration. Arrows indicate single recombination events. Scale bar 100 μm.**b,** Representative images of adult hearts with sparse clones. Recombination was induced at E9.5. Insets show magnification of boxed areas. Scale bar 500μm. **c**, Tamoxifen is removed from the circulation within 24 hours after treatment. Blood serum levels of tamoxifen measured 12, 24, and 72 hours following administration. Tam, tamoxifen; OFT, outflow tract; PRV, primitive right ventricle; PLV, primitive left ventricle.

Within *βactin*^{CreER}; *R26*$^{VT2/GK}$ mouse hearts, we observed fibroblast, endothelial, and smooth muscle cell clones (**Figure 2.4a-d**), however, we focused our analysis on CM clusters. When recombination was induced at E9.5, we identified single-colored clones ranging from two to 40

cells, with an average of 5.7 cells/clone at all time-points analyzed (**Figure 2.5a** and **Figure 2.6a-b**). Clone size quantification revealed slightly larger clones at P7, P15, and P30 compared to P2 (**Figure 2.6b**), which agrees with several studies suggesting limited proliferative capacity of CMs during early postnatal life[92-94]. Interestingly, we observed a drop in the number of clones larger than 20 cells at P30 (**Figure 2.6b**), which was accompanied by an increase in single "Rainbow-colored" cells (**Figure 2.6c**). Possible explanations for the higher incidence of single cells include migration of daughter cells after division within a clone or dispersion of sibling cells in a clone among other dividing neighboring cells. Isolation and *in vitro* culture of single "Rainbow-labeled" cardiac cells from E9.5 *βactin*^{CreER}*; R26*$^{VT2/GK}$ embryos showed that these cells retained their ability to form clones through several rounds of division (**Figure 2.7**). These findings suggest that cardiac cells marked as early as E9.5 have the capacity to form large clones both *in vivo* and *in vitro*.

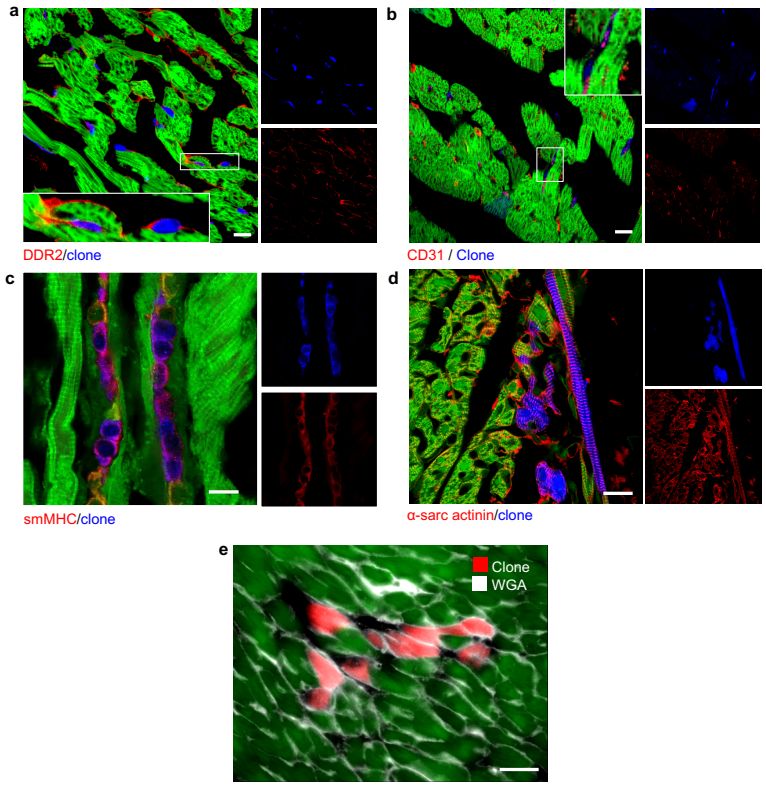

Figure 2.4: Immunohistochemical staining of clones.
Immunohistochemical staining of *βactin*^{CreER} ; *R26*$^{VT2/GK}$ clones positive for **a,** the fibroblast marker, DDR2, **b,** endothelial cell marker, CD31, **c,** smooth muscle myosin heavy chain, smMHC (scale bar 50 μm), and **d,** CM, α-sarcomeric actinin. Insets show close ups of the co-localization. **e,** WGA (white) was used to delineate individual cells within a clone (red pseudocolor) for counting purposes. Scale bar 100 μm unless otherwise denoted.

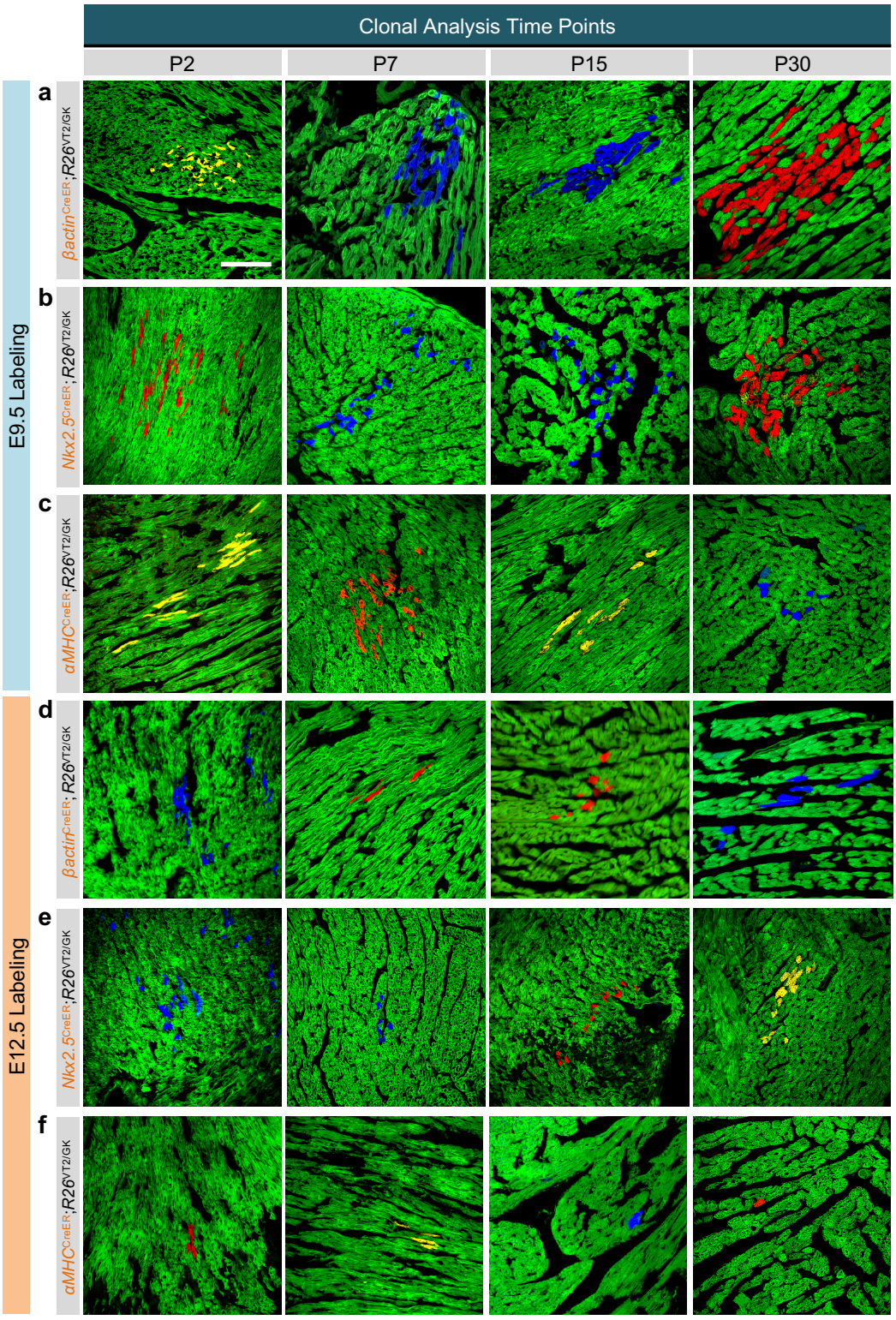

Figure 2.5: Cardiac growth occurs primarily through clonal expansion of non-αMHC expressing cells. **a**, Representative confocal microscope images of cell cluster expansion in **a,d,** *βactin*^{CreER} ; *R26*$^{VT2/GK}$, **b,e,** *Nkx2.5*^{CreER} ; *R26*$^{VT2/GK}$ and **c,f,** *αMHC*^{CreER} ; *R26*$^{VT2/GK}$ hearts at different developmental time-points, following tamoxifen administration at E9.5 **(a-c)** and E12.5 **(d-f)** (n = 6 for each time-point). Scale bar 100 μm.

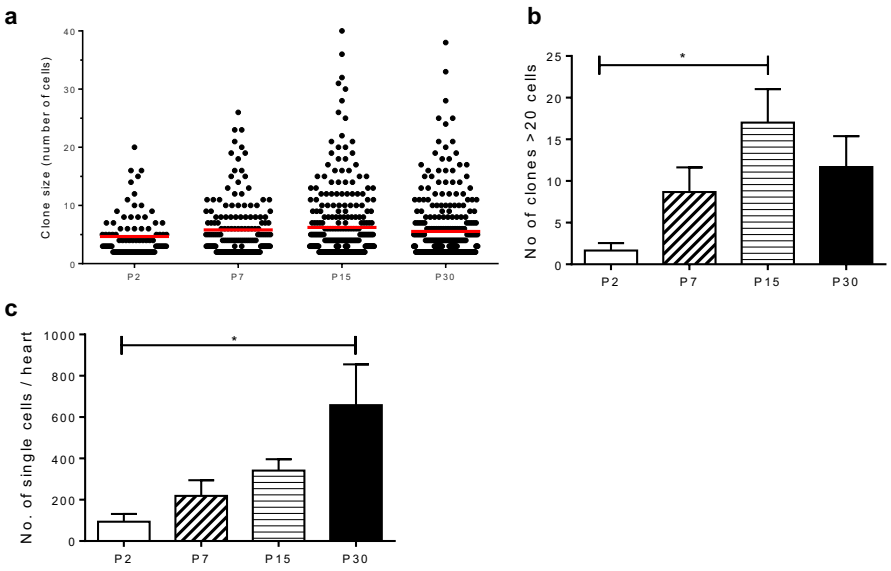

Figure 2.6: Clonal expansion occurs mainly during embryonic development.
a, Dot plot analysis of clonal sizes in *βactin*^{CreER} ; *R26*$^{VT2/GK}$ hearts labeled at E9.5 and analyzed at P2, P7, P15, and P30 (n=3). **b**, Number of clones > 20 cells progressively increase up to P15 and declines by P30. **c**, Number of single cells increases over time (n=3). All measurements shown are depicted as mean ± SEM.

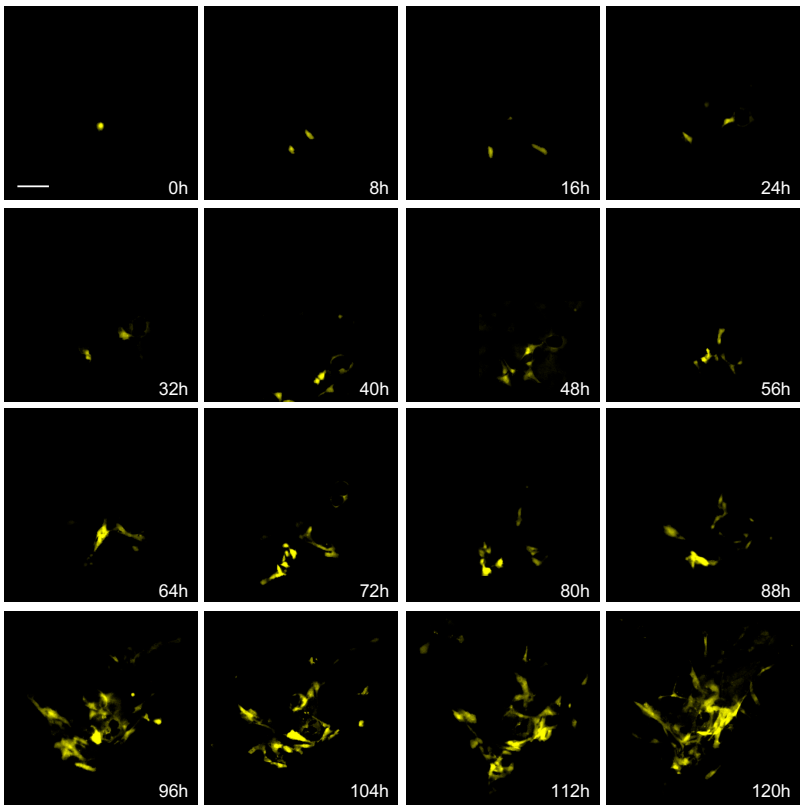

Figure 2.7: "Rainbow-labeled" cardiac cells expand clonally *in vitro*.
Time-lapse imaging of a single rainbow-labeled cell (yellow pseudocolor) forming a clone *in vitro*. Monitoring was performed 0-120 hours after plating. Scale bar 100μm.

To determine whether cardiac progenitors are the main contributors to the observed CM clonal expansion, we generated an inducible Nkx2.5 reporter mouse (*Nkx2.5*^{CreER}) by targeting an IRES-CreER sequence to the 3' end of the endogenous Nkx2.5 locus, in order to avoid haploinsufficiency (**Figure 2.8**). Clonal analysis of *Nkx2.5*^{CreER}*; R26*$^{VT2/GK}$ mice labeled at E9.5 and analyzed at P2 revealed a similar pattern of clonal expansion, with the largest clone containing 39 cells, and an average of 7.5 cells/clone (**Figure 2.5b** and **Figure 2.11a**). Collectively, these data support the proliferative capacity of progenitor cells to generate myocardial cells during early fetal development.

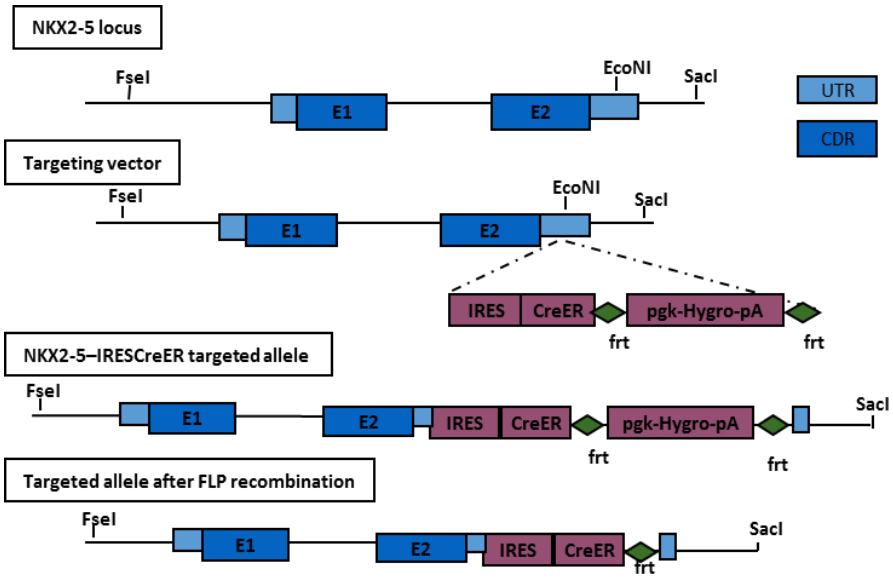

Figure 2.8: Generation of the Nkx2.5-CreER construct.
Maps of the Nkx2.5 wild-type allele, gene targeting construct and resultant mutant alleles before (Nkx2.5IRES-CreER-pgkHYGRO) and after (Nkx2.5IRES-CreER) flp-mediated deletion. Several stable clones were generated and founders of this new strain (Nkx2.5-CreER) were backcrossed onto C57BL/6 mice.

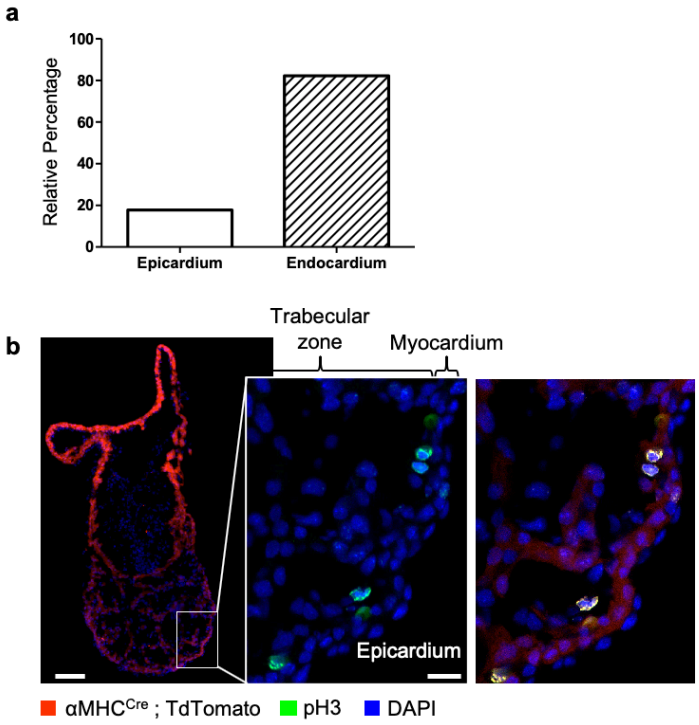

Figure 2.9: CM clones are mainly localized near the endocardium.
a, Quantification of CM clones based on their proximity to either the epicardium or the endocardium. Tamoxifen was administered at E9.5 and hearts were analyzed at P2. **b,** Immunohistochemical staining for phospho-Histone H3 (pH3 in green) of a E9.5 *αMHC*^{Cre} ; TdTomato heart. Scale bar 100μm. Inset shows magnification of boxed area, scale bar 20μm.

2.4.3. αMHC-marked cells decrease their proliferation over time

While these studies support the active division of cardiac progenitors during early cardiovascular development, we sought to determine the proliferative behavior of CMs at similar stages of development. To accomplish this, we crossed *R26*$^{VT2/GK}$ with mice harboring an inducible Cre under the control of an αMHC (*αMHC*^{CreER}) promoter. Expression of αMHC in embryonic mouse hearts was observed at E9.5, and by E12.5, most of the distribution was found in the atria and to a lesser extent in the ventricles (**Figure 2.10a**).

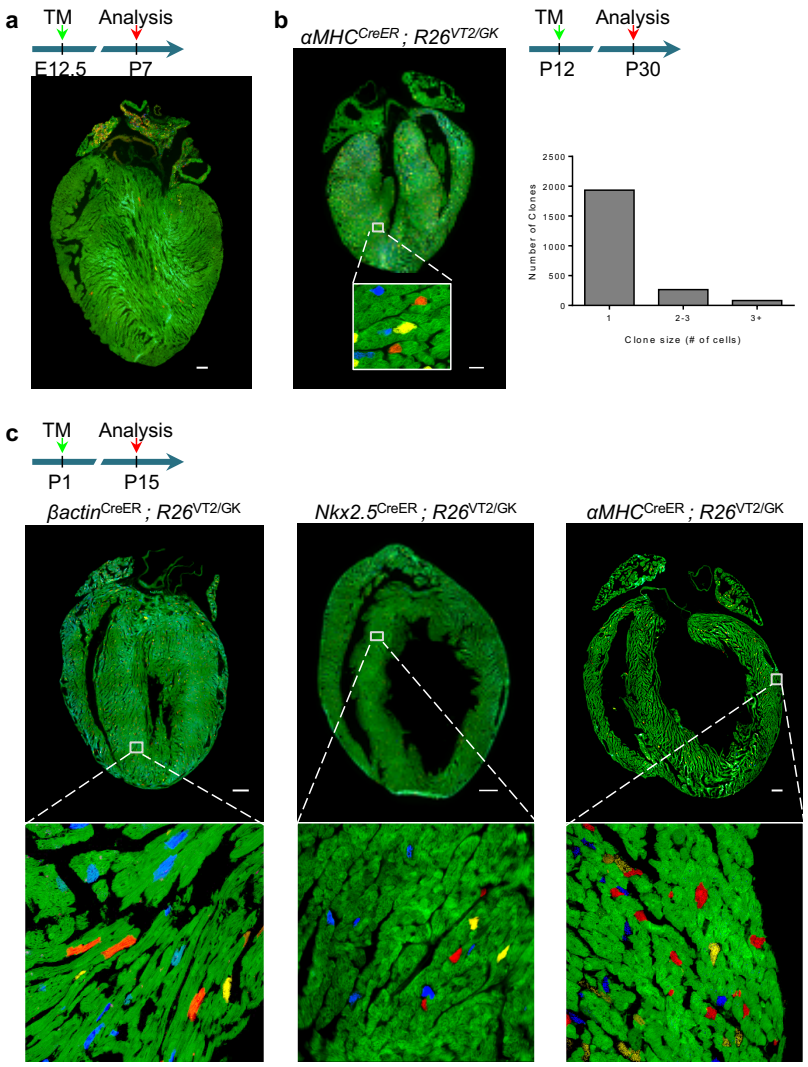

Figure 2.10: Postnatal CMs exhibit limited proliferative capacity in the absence of injury. **a,** *αMHC*^{CreER} ; *R26*$^{VT2/GK}$ mouse heart labeled at E12.5 and analyzed P7 showing the distribution of αMHC primarily in the atria and to a lesser extent in the ventricles, scale bar = 200 μm. **(b, left)** Representative image of *αMHC*^{CreER} ; *R26*$^{VT2/GK}$ P30 heart labeled at P12 showing the dominance of single Rainbow-labeled cells, scale bar 500 μm. **(b, right)** Quantitation of clone size and number within *αMHC*^{CreER} ; *R26*$^{VT2/GK}$ mouse hearts labeled at P12 and analyzed P30 (n=4, 8 images at 40X magnification analyzed per section, 5 sections/heart).**c**, Representative confocal microscope images of *βactin*^{CreER} ; *R26*$^{VT2/GK}$, *Nkx2.5*^{CreER} ; *R26*$^{VT2/GK}$, and *αMHC*^{CreER} ; *R26*$^{VT2/GK}$ P15 hearts labeled at P1. Insets show up close view of boxed areas. Scale bar 500 μm.

Analysis of *αMHC*^{CreER}; *R26*$^{VT2/GK}$ mice labeled at E9.5 revealed smaller clones (largest observed consisted of 30 cells, with an average of 6.3 cells/clone) compared to *βactin*^{CreER}; *R26*$^{VT2/GK}$ and *Nkx2.5*^{CreER}; *R26*$^{VT2/GK}$ in which clones >50 cells were observed (**Figure 2.5c** and **Figure 2.11a**). Arbitrary clone size cutoff (dashed lined) was determined as two standard deviations above the clone size mean of *αMHC*^{CreER}; *R26*$^{VT2/GK}$. Comparison of the percent of

clones within each strain larger than this cutoff showed similar percentages at E9.5 (**Figure 2.11b**). Interestingly, the majority of clones were localized to the inner endocardial region (**Figure 2.9a**) and phospho-H3 staining in E9.5 hearts was mainly localized to the myocardial compact zone, suggesting that clonal growth may be directed towards the endocardium (**Figure 2.9b**). Furthermore, βactin and Nkx2.5 expressing cells labeled at E12.5 exhibited a slight decrease in proliferation compared to at E9.5 (up to 26 cells/clone in βactin, and 21 cells/clone in Nkx2.5) (**Figure 2.5d,e** and **Figure 2.11c**). However, a dramatic decrease was observed in αMHC cells labeled at E12.5, with the largest clone consisting of only 9 CMs when analyzed postnatally. Additionally, the percentage of clones larger than 2 cells decreased by 30% compared to labeling at E9.5, with exceedingly rare clones consisting of more than 5 CMs (**Figure 2.5f** and **Figure 2.11d**). This suggests that αMHC-expressing CMs at E9.5 retain the ability to proliferate (albeit to a lesser degree than Nkx2.5 cardiovascular progenitors), and that this capacity is significantly diminished by E12.5.

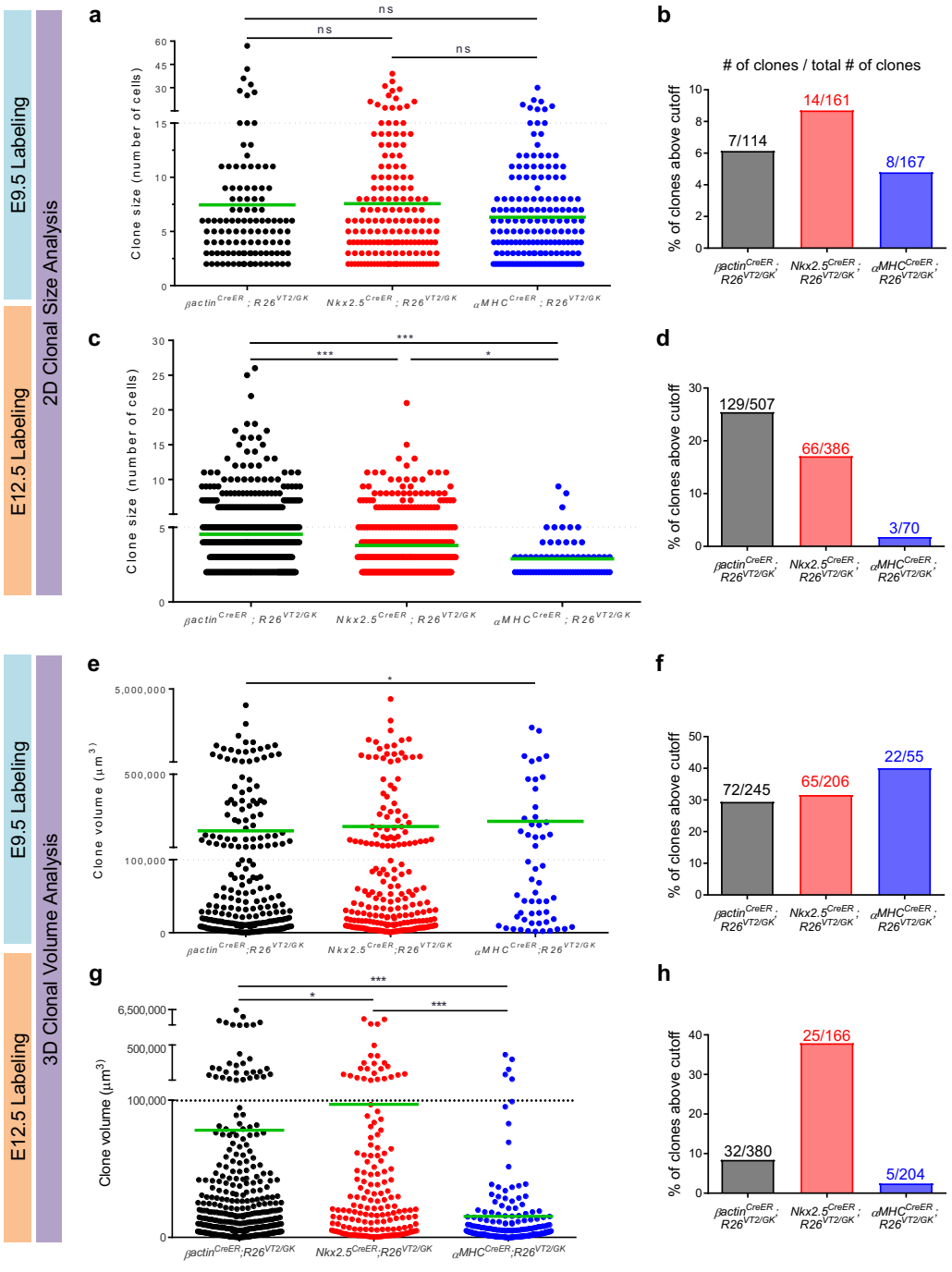

Figure 2.11: 2D and 3D quantification reveals a dramatic decrease in the proliferative capacity of αMHC-expressing cells.
Quantification of clonal expansion in P2 *βactin*^{CreER} ; *R26*$^{VT2/}$, *Nkx2.5*^{CreER} ; *R26*$^{VT2/GK}$, and *αMHC*^{CreER} ; *R26*$^{VT2/GK}$ hearts labeled at E9.5 **(a, b and e, f)** and E12.5 **(c, d and g, h)** (two-sample Kolmogorov–Smirnov distribution test) * $p < 0.05$, ** $p < 0.01$, *** $p < 0.001$. Two-dimensional quantification of clonal expansion **(a, c)** and bar graphs highlighting the scarcity of large clones in *αMHC*^{CreER} ; *R26*$^{VT2/GK}$ hearts **(b, d),** respectively. Three-dimensional quantification of clone volumes in P2 hearts **(e, g)** and bar graphs depicting clones volumes in *αMHC*^{CreER} ; *R26*$^{VT2/GK}$ hearts **(f, h).** Green lines depict mean values. Dashed lines depict cutoff.

Our two dimensional (2D) quantification revealed striking differences in clone sizes that emerged from labeling single progenitors or CMs at different time points. However, there is possibility for error in clone size estimation, as the depth of each cell cluster cannot be accounted for using cross sections. To address this, we developed a modified CLARITY technique[95] to transform the intact heart into an optically-transparent but structurally-preserved organ for light sheet fluorescence microscopy (**Figure 2.12a-b**). This methodology facilitates three dimensional (3D) imaging of whole neonatal mouse hearts to precisely quantify and compare clone volumes from each strain at various time points (**Figure 2.12c**, Supplementary Movie 2). To provide a parallel comparison with our 2D results, we labeled the three strains at both E9.5 and E12.5. Analysis of P2 cleared hearts from *βactin*^{CreER}*; R26*$^{VT2/GK}$ and *Nkx2.5*^{CreER}*; R26*$^{VT2/GK}$ mice labeled at E9.5 revealed clones of similar volumes (average 190220 μm^3 and 214260 μm^3, respectively), which decreased by ~2-fold when labeling occurred at E12.5 (**Figure 2.11e, g**). In *αMHC*^{CreER}; *R26*$^{VT2/GK}$ hearts labeled at E9.5 and analyzed at P2, we did not find a difference in clone volumes compared to *Nkx2.5*^{CreER}*; R26*$^{VT2/}$GK and the percent of clones within each strain with volumes above 100,000 μm^3 were similar (**Figure 2.11f**). However, when labeling was initiated at E12.5, significant differences were observed in volumes of *αMHC*-marked clones compared to *β-actin* and *Nkx2.5* ($p < 0.001$) and there was a substantial decrease in the percent of clones within *αMHC*^{CreER}; *R26*$^{VT2/GK}$ that were above the volume cutoff compared to *Nkx2.5*^{CreER}*; R26*$^{VT2/GK}$ (**Figure 2.11h**). Additionally, within *aMHC*-marked clones, there was a ~16-fold decrease in volumes with labeling at E12.5 when compared to E9.5. These results further validate the notion that while αMHC-marked CMs retain the ability to proliferate during early embryonic development, cardiovascular progenitors are the primary contributors of cardiac growth during this time.

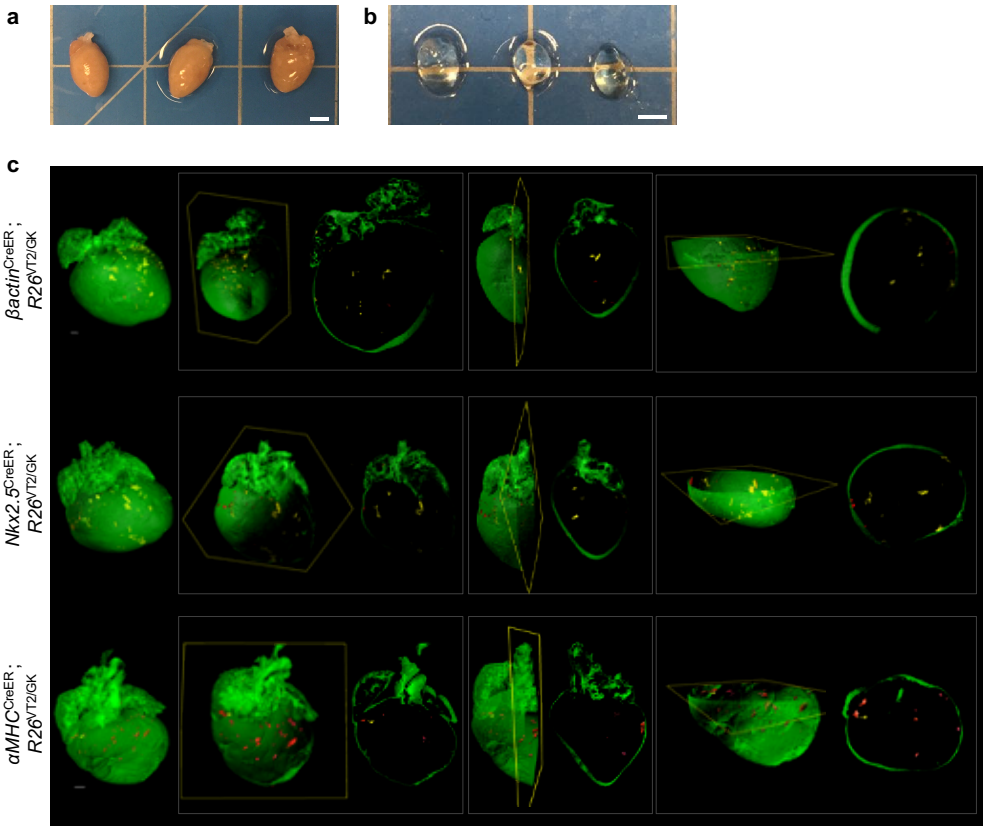

Figure 2.12: Three-dimensional imaging of cleared whole neonatal mouse hearts using the CLARITY method.
P2 hearts **(a)** prior to CLARITY and **(b)** post CLARITY, scale bars = 2 mm. **c,** 3-dimensional rendering of cleared P2 hearts from *βactin*^{CreER} ; R26$^{VT2/GK}$, *Nkx2.5*^{CreER} ; R26$^{VT2/GK}$, and *αMHC*^{CreER} ; R26$^{VT2/GK}$. Examples of sagittal, coronal, and axial planes captured using Imaris 7.7.2 software (Bitplane AG, Zurich).

To exclude the possibility that lack of clone formation in *αMHC*^{CreER}; *R26*$^{VT2/GK}$ hearts is due to the inability of the system to specifically label CMs with proliferative potential, we stimulated CM proliferation with neuregulin (NRG1), an extracellular growth factor shown to promote CM cell cycle re-entry in normal and injury conditions[96] (**Figure 2.13**). *αMHC*^{CreER}; *R26*$^{VT2/GK}$ mice received tamoxifen to induce sparse labeling of CMs at P15 followed by daily administrations of NRG1 from P20 to P28. Scoring the frequency of clones revealed an increase in “Rainbow-labeled” CM clones in NRG1 treated hearts compared to control (4–fold increase in doublets) (**Figure 2.13b-c**). This validates that the decreased clonal size observed in *αMHC*^{CreER}; *R26*$^{VT2/GK}$ hearts during development is due to the limited intrinsic ability of these cells to divide and further support the validity of the Rainbow system as a sensitive tool for clonal analysis.

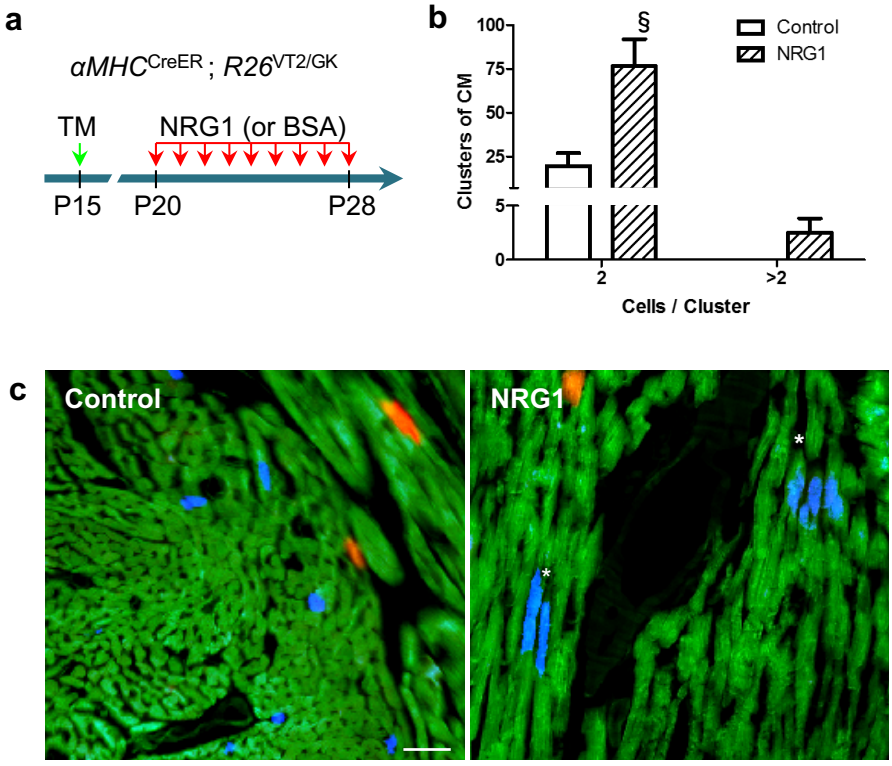

Figure 2.13: NRG1 treatment induces postnatal CM proliferation.
a, Experimental design of NRG1 treatment. Arrow indicates tamoxifen administration at P15. NRG1 (n=4) or BSA control (n=3) were given daily to *αMHC*^{CreER} ; *R26*$^{VT2/GK}$ mice from P20 to P28. **b,** Quantification reveals increased formation of CM clusters following NRG1 treatment. **c,** Representative fluorescent microscope images of control and NRG1-treated hearts. Stars indicate clusters of CMs. § NRG1 vs control, $p<0.05$. Scale bar 50 μm. All measurements shown are depicted as mean ± SEM.

Our results thus far suggest that cardiac development is a continuum in which progenitors progressively transition to more mature, less proliferative CMs. Interestingly, a recent prior study[97] reported a burst of highly synchronized CM proliferation during preadolescence. This proliferative event, occurring at P14, resulted in a remarkable 40% increase in CM number. To examine whether the decrease in CM proliferation we observed during embryonic development is followed by a re-activation of cell division postnatally, we labeled single CMs at P12 using *αMHC*^{CreER}; *R26*$^{VT2/GK}$ mice and looked at their proliferative potential retrospectively at P30. Consistent with other reports[93, 98], we observed mainly single-labeled cells dispersed throughout the myocardium and rare clones of 2-3 cells (**Figure 2.10a**). Furthermore, we detected rare clusters of CMs consisting of >2 cells derived from βactin-, Nkx2.5-, or αMHC-Rainbow labeling at P1, suggesting

limited expansion of CMs even prior to preadolescence (**Figure 2.10c**). Collectively, these findings do not support the substantial second wave of CM proliferation during preadolescence as was described.

2.4.4. Epicardial progenitors are unlikely to be sources of CMs

While our studies demonstrate the source of CMs during development, it does not address whether stem/progenitor cells are entirely endogenous to the myocardium. There is controversy regarding the contribution of epicardial cells to the developing heart. Several studies have reported that epicardial cells can differentiate into endothelial cells, vascular smooth muscle cells, fibroblasts, and even CMs[99, 100]. To examine whether the observed clones may have originated from epicardial-derived progenitor cells, rather than intramyocardial progenitors or CMs, we utilized a *Wt1*^{CreER}; *R26*$^{VT2/GK}$ double-transgenic mouse (**Figure 2.14a**). Postnatal analysis of cells labeled at E9.5 or E12.5 did not reveal any Rainbow-labeled CMs, but the clones identified primarily consisted of fibroblasts and in some cases, smooth muscle cells (**Figure 2.14b-c**).

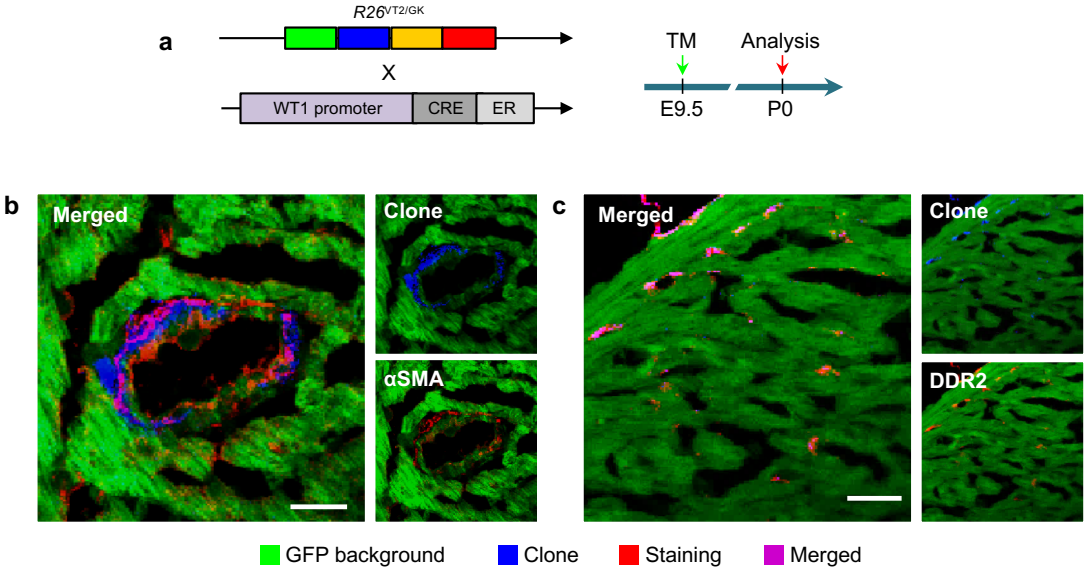

Figure 2.14: Smooth muscle cell and fibroblast clones of WT1 origin.
a, Experimental design. *Wt1*^{CreER} ; *R26*$^{VT2/GK}$ mice received tamoxifen at E9.5 and were analyzed at P0. **b-c,** Representative confocal microscope images of **b**, a clone (blue) consisting of smooth muscle cells (α-SMA in red) and **c**, a clone of fibroblasts (DDR2 in red). Insets show the individual pseudocolors in GFP background. Scale bars 20 μm.

2.4.5. BrdU studies uncover decreased proliferative capacity of CMs

To further support our clonal analysis data, *in vivo* BrdU pulse/chase experiments were performed. BrdU was administered to dames carrying *αMHC-GFP* embryos at E9.5 or E12.5 and to P1 neonates three hours prior to heart harvest. Flow cytometric analysis of αMHC$^+$ cells revealed a dramatic decrease in the percentage of BrdU$^+$ CMs from E9.5 to E12.5 (~9 fold decrease) and P1 (~60-fold decrease) (**Figure 2.15a-b** and **Figure 2.16a**). We next evaluated the proliferation of αMHC-expressing CMs relative to cardiac progenitors by performing a similar pulse/chase experiment in triple transgenic mice (*Nkx2.5$^{+/Cre}$; R26R-Tdt$^{+/fl}$; αMHC$^{+/GFP}$*). In this model, cardiac progenitors (*Nkx2.5$^+$/αMHC$^-$*) express only tdTomato while αMHC-expressing CMs (*Nkx2.5$^+$/αMHC$^+$*) express both tdTomato and GFP. We observed that while the fraction of αMHC-expressing CMs increased from E9.5 to E12.5 and P1 (**Figure 2.16a**), their proliferative capacity at E12.5 and P1 decreased by ~7–folds and 65-folds compared to E9.5, respectively, as indicated by the decrease in percentage of BrdU incorporation (**Figure 2.15c**). Importantly, we observed a significantly lower proportion of BrdU+ cells at E12.5 and P1 within the CM population compared to progenitors even though their BrdU incorporation was relatively similar at E9.5 (**Figure 2.15d**). Correspondingly, expression of cell cycle markers (*Ccnb, Cdc6, and Ccna*) in GFP+ CMs isolated from *αMHC-GFP* mice were higher at E9.5 compared to later time points (**Figure 2.15e**), and this was inversely correlated with αMHC expression levels (**Figure 2.15f**). These data suggest that as the embryonic heart develops, αMHC-expressing cells become progressively more committed, while progenitor cells retain their proliferative potential for a longer span of time. It is possible that αMHC marks a heterogeneous population of CMs that differ in their proliferative capacity and maturity level; less mature αMHC-expressing cells may exhibit higher proliferative potential, whereas more mature αMHC-expressing CMs (found in abundance at E12.5 and beyond) are limited in their ability to undergo division. We therefore hypothesized

that heart formation is a dynamic process that consists of CMs with varying proliferative potential and that these populations are refined as development proceeds.

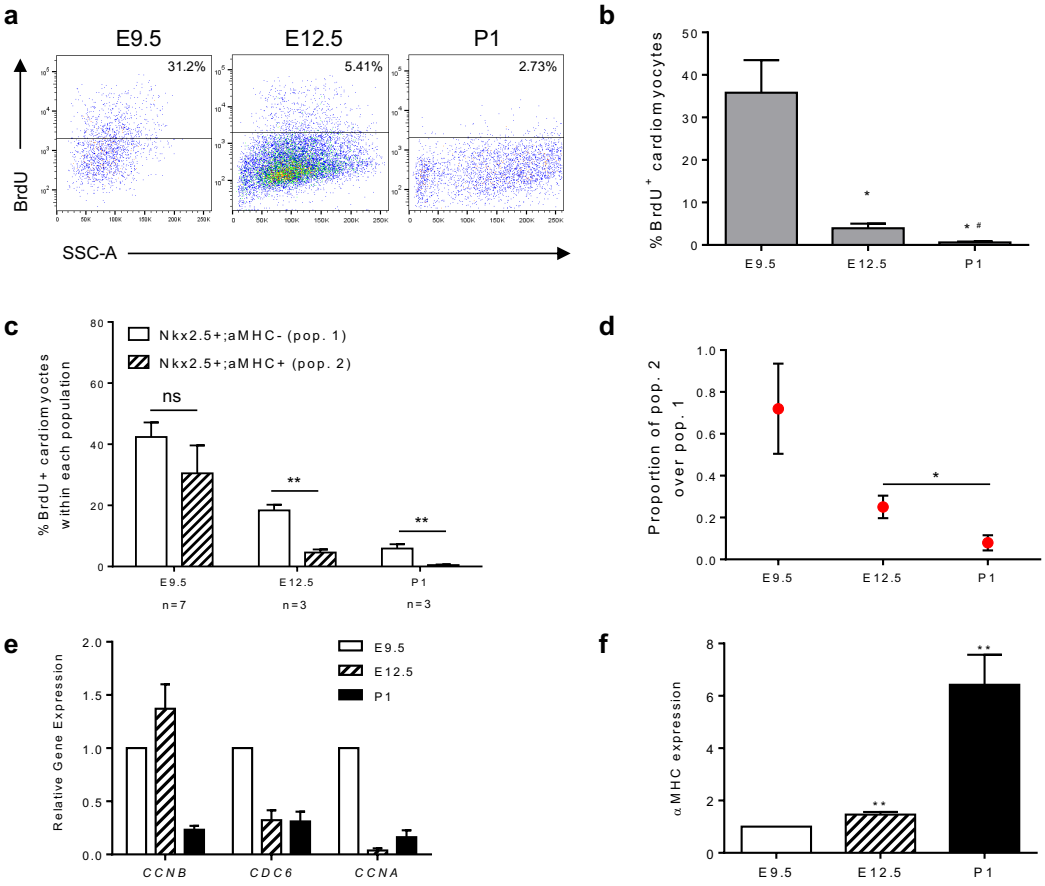

Figure 2.15: BrdU pulse-chase experiments substantiate decreasing proliferative capacity of CMs. **a,** Representative flow cytometric analysis of BrdU incorporation. BrdU was given at E9.5, E12.5 or P1 αMHC-GFP mice 3 hrs prior to analysis. **b,** Quantification of BrdU$^+$ αMHC-GFP$^+$ cells at E9.5, E12.5, and P1. (student's t-test), * E12.5 or P1 vs E9.5, # P1 vs E12.5, $p < 0.05$. **c**, Quantification of percent BrdU incorporation in Nkx2.5$^+$;αMHC$^-$ and Nkx2.5$^+$;αMHC$^+$ cells at E9.5, E12.5, and P1. (student's t-test), ** $p < 0.01$. **d,** Proportion of BrdU+ cells within the cardiomyocyte (Nkx2.5$^+$;αMHC$^+$) compared to progenitor (Nkx2.5$^+$;αMHC$^-$) populations at E9.5, E12.5, and P1. (student's t-test), * $p < 0.05$. **e,** qPCR analysis of αMHC-GFP$^+$ cells reveals an age-dependent drop in expression of cell cycle genes (*Ccna2*, *Ccnb1*, *Cdc6*). **f,** qPCR analysis of αMHC gene expression in αMHC-GFP$^+$ cells from E9.5 to P1. All measurements shown are depicted as mean ± SEM.

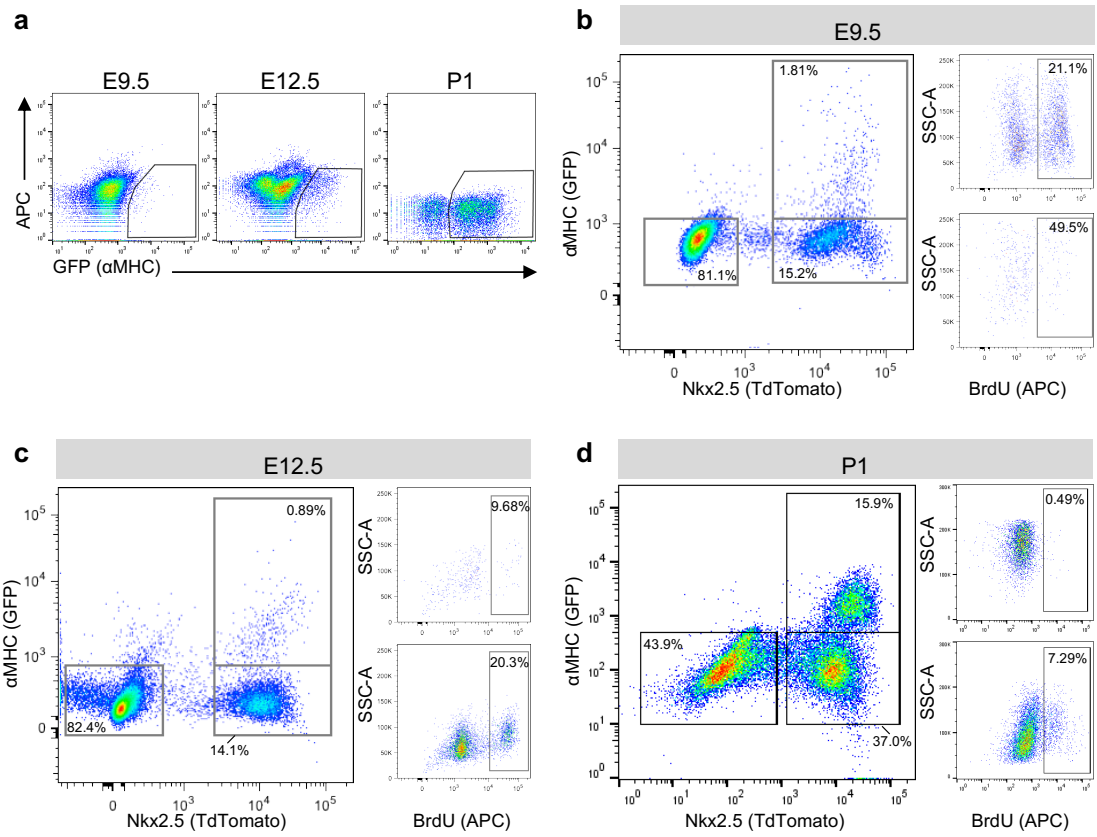

Figure 2.16: BrdU incorporation in CMs during development.
a, Representative flow cytometric analysis of αMHC-GFP cells sorted for qPCR or single cell analysis. Gated areas show cells selected for sorting. **b-d,** Representative flow cytometric analysis plots of BrdU incorporation in *Nkx2.5$^{+/Cre}$; R26R-Tdt$^{+/fl}$; αMHC$^{+/GFP}$* hearts at **(b)** E9.5, **(c)** E12.5, and **(d)** P1.

2.4.6. Single cell RNA sequencing delineates heterogeneity of CMs

To test this hypothesis and to profile the potential heterogeneity of CMs during early cardiac development, we used a Fluidigm C1 chip platform to capture αMHC+ cells from *αMHC-GFP* murine hearts at E9.5, E12.5, and P1 for single cell RNA sequencing. Overall, we analyzed a total of 122 cells that passed quality screening. Unsupervised dimensionality reduction by t-SNE identified clusters of single cells that appeared to correspond to their developmental time point (**Figure 2.17a**). Heat map analysis of these cells on genes relevant to cardiac development and maturation showed that P1 CMs displayed a more mature, less proliferative transcriptional profile that is distinguishable from E9.5 and E12.5 clusters (**Figure 2.17b**). In particular, genes encoding

for cell cycle, cardiac cell differentiation, and cellular migration were downregulated in P1 cells while these same markers were expressed at high levels in the majority of E9.5 and E12.5 CMs. Conversely, the expression of genes encoding for structural proteins and cellular metabolism were upregulated in the P1 population but expressed at low levels in the earlier time points. We also observed substantial heterogeneity in gene expression levels within E9.5 and E12.5 cells compared to P1. Expression of cell cycle-associated genes (*Ccnb1, Cdc6, and Ccna2*) from individual cells at each time point confirmed our qPCR results showing a decline in cell cycle activity from E9.5 to P1 (**Figure 2.17c** and **Figure 2.15e**). Additionally, consistent with our hypothesis that early embryonic CMs span a broad spectrum in their capacity to proliferate, we observed a wide range of gene expression levels of cell cycle markers at E9.5 that progressively narrowed at later time points. These results provide initial evidence to support the existence of a heterogeneous population of CMs within the early stages of cardiac development and their transition into a mature, less proliferative, and homogenous population by the early postnatal period.

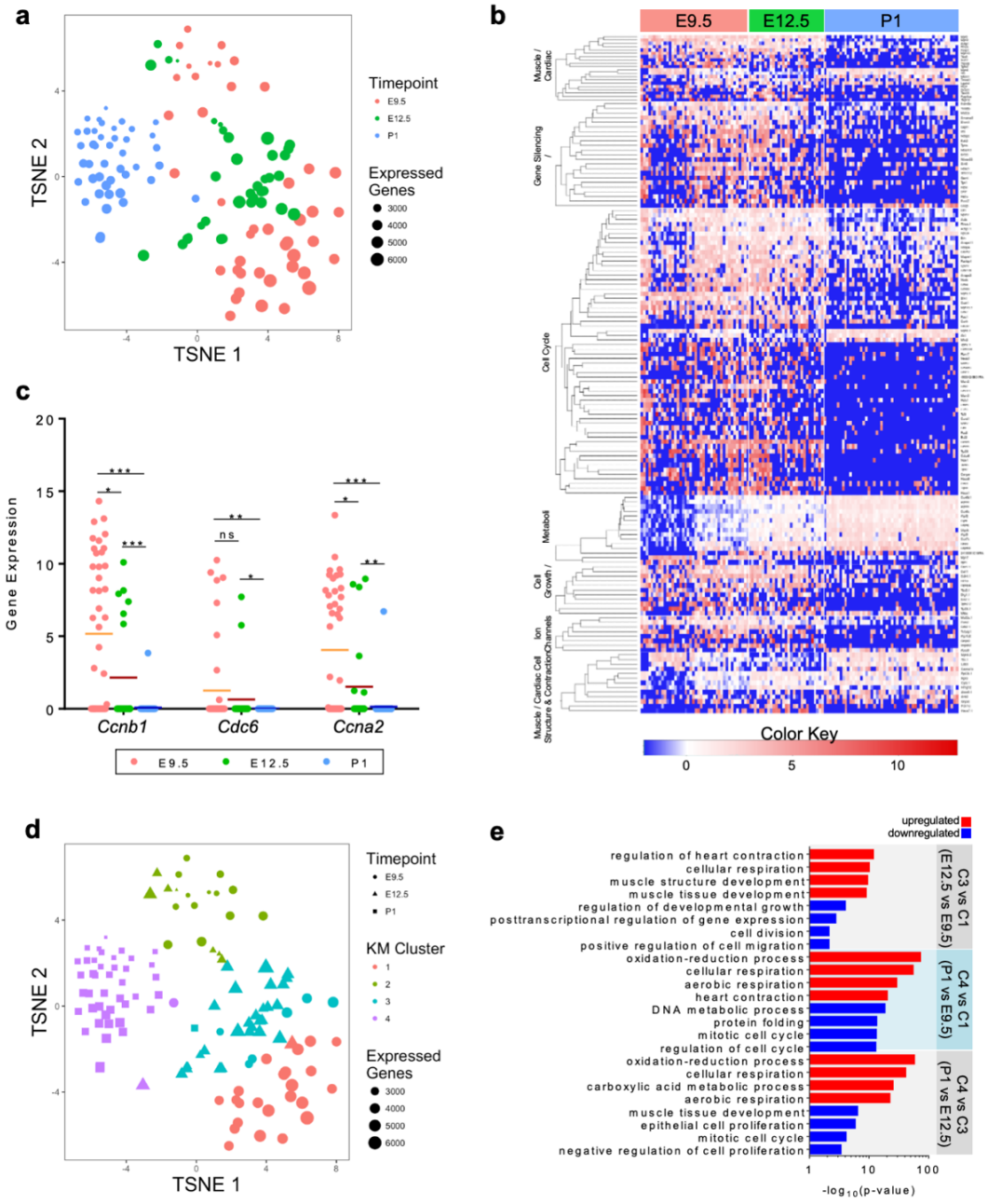

Figure 2.17: Single cell gene expression analysis reveals heterogeneity of CMs within and between developmental time points.
a, t-SNE revealing distribution of single cells. **b,** Heat map analysis of single cells from different developmental time points on genes relevant to cardiac development and maturation (E9.5: n = 42, E12.5: n = 29, P1: n = 52). The full list of genes presented in the maps is provided in Supplementary Table 1. **c,** Expression of cell cycle-associated genes (*Ccna2, Ccnb1, Cdc6*) from individual cells at each time point confirming a decline in cell cycle activity from E9.5 to P1 (student's t-test), * $p < 0.05$, ** $p < 0.01$, *** $p < 0.001$. Mean depicted as solid line. **d**, t-SNE with k-m based clustering identifies 4 distinct clusters. **e**, Gene ontology analysis of upregulated and downregulated genes between different clusters.

To further characterize the heterogeneity we observed in the heat map analysis of CMs from E9.5 and E12.5, we utilized a k-means clustering algorithm to classify subgroups within the t-SNE (**Figure 2.17d**). This approach yielded four distinct clusters, which we used for subsequent transcriptomic analyses (**Figure 2.18a**). Of particular interest are Clusters 1 and 3, which are enriched for E9.5 and E12.5 cells, respectively. To identify potential transcriptomic changes that occurs between E9.5 and E12.5 that may contribute to the clonal size differences observed in our *in vivo* studies, we performed gene ontology analysis of differentially expressed genes between these clusters (**Figure 2.17e**). Pathways involved in developmental growth, cell division, and migration were downregulated within Cluster 3 compared to Cluster 1. Conversely, there was upregulation in pathways involved in the regulation of heart contraction, cellular respiration, and muscle development within Cluster 3. Interestingly, we identified 4 genes (*Thbs4, Kif26b, Col2a1, and Prtg*) that were only expressed in E9.5 cells, and 2 others (*Sall4* and *Hmga2*) whose expression was primarily concentrated in cells from this time point (44% and 53% of E9.5 cells, respectively) (**Figure 2.18b**). From these, *Thbs4*, *Sall4*, and *Hmga2* are genes associated with Gene Ontology pathways involved with developmental growth and cell division and migration. As expected, a comparison of genes enriched in Cluster 4 (containing primarily P1 cells), revealed an increase in pathways involved in cellular respiration, heart contraction, and metabolism when compared to Cluster 1 or 3. On the other hand, pathways involved in cellular proliferation and developmental growth were downregulated in cells within this cluster. These results suggest that by E12.5, CMs have already begun to shift to an initial state of maturation and have downregulated vital genes involved with cell division and migration, potentially contributing to the decrease in clone sizes observed in our analysis of CMs labeled at this developmental time point. Interestingly, we observed a P1 cell which segregated more closely with other E9.5 and E12.5 cells than their counterparts (residing within Cluster 3). Differential gene expression analysis revealed considerable differences in the gene profiles of this cell with the remaining P1 cluster (**Figure 2.18c**). Analysis using the STRING (Search Tool for the Retrieval of Interacting

Genes/Proteins) database comparing the top 50 genes more highly expressed in the P1 cluster compared to the outlier identified two nodes associated with metabolism and cardiac structural proteins (**Figure 2.18d**). This suggests that this particular P1 cell may be a rare CM present in the postnatal heart that retains some immature, more proliferative characteristics generally present only in earlier embryonic CMs. However, further studies examining a larger number of cells with similar characteristics are needed to substantiate this observation.

To examine how expression of cell cycle genes may relate with CM maturity, cells from E9.5 and E12.5 were selected based on low or high cycling activity, and concomitantly, their expression of cardiac structural proteins and transcription factors were examined (**Figure 2.18e**). CMs with high cell cycle activity according to gene expression profiles displayed a “progenitor-like” gene profile, in which there was low expression of structural proteins (*Myh6, Ttn, Myl4, Flnc)* indicating immaturity, and high expression of transcription factors involved in embryonic and cardiac development *(Nkx2-5, Gata6, Tbx18*). Likewise, CMs with low cell cycle activity had an expression signature indicative of a more mature CM, with high levels of structural proteins and low levels of early cardiac transcription factors. These findings indicate a possible link between cell cycle activity and CM maturity that may be independent of embryonic age.

a

	E9.5	E12.5	P1
Cluster 1	23	1	0
Cluster 2	13	7	0
Cluster 3	6	27	1
Cluster 4	1	1	42
Total	**43**	**36**	**43**

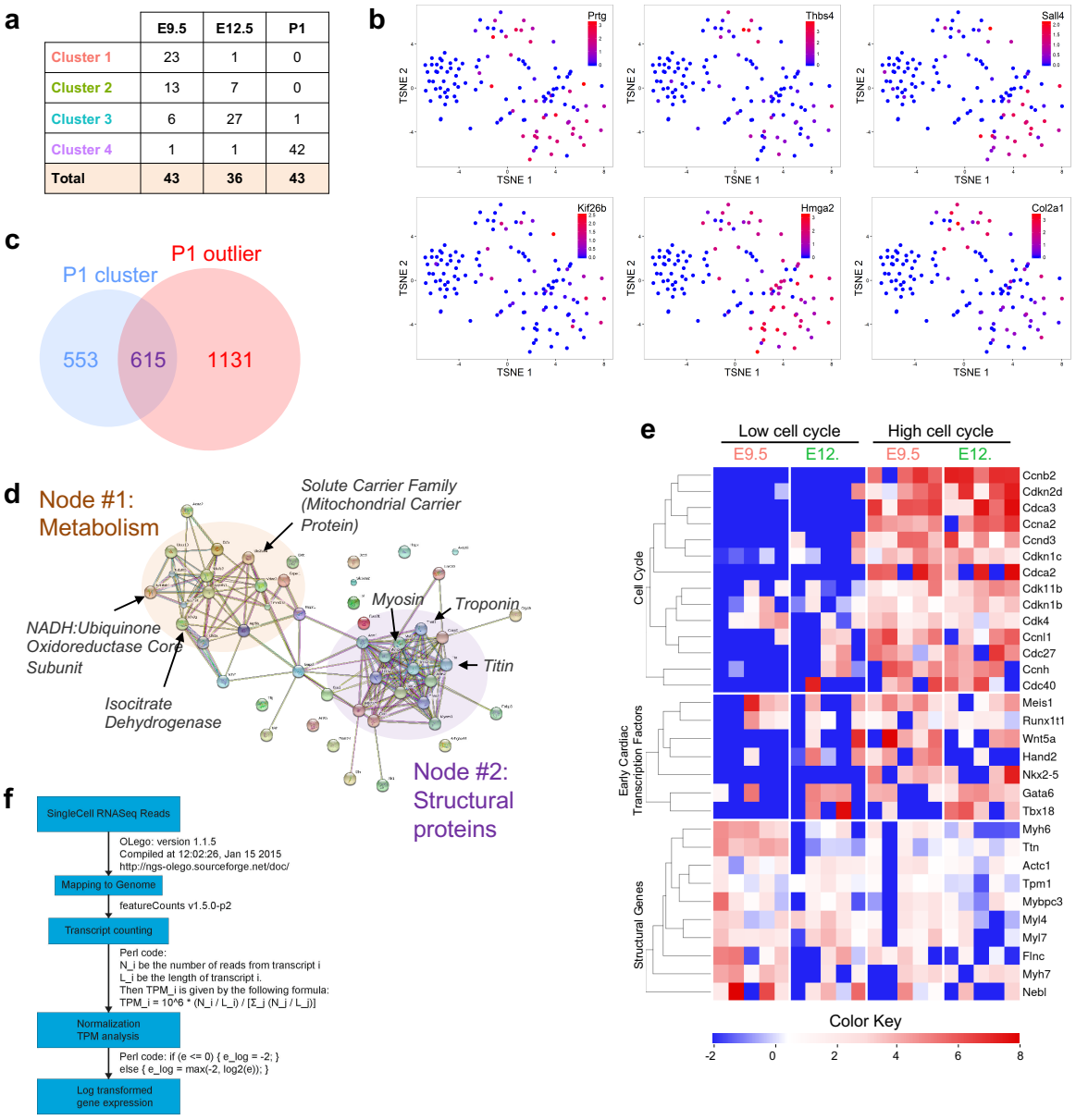

Figure 2.18: Transcriptional profiling of CMs during early embryonic and postnatal development. **a,** Table depicting numbers of single cells found within each km cluster. **b,** Expression of genes found only in E9.5 cells (*Thbs4, Kif26b, Col2a1, Prtg)* or were highly enriched (*Sall4, Hmga2)* within cells from this timepoint. **c**, Venn diagram depicting the number of differentially expressed genes between P1 cluster and P1 outlier. **d**, Search Tool for the Retrieval of Interacting Genes/Proteins (STRING) analysis comparing the top 50 genes more highly expressed in the P1 cluster compared to P1 outlier. Two nodes were identified encoding for genes of metabolism (bronze circle) and structural proteins (purple circle). **e,** Single cells at E9.5 and E12.5 were selected based on low or high cell cycle activity, as determined by expression levels of common cell cycle genes. Genes encoding for cardiac structural proteins and transcription factors were examined within the selected cells showing a possible link between cell cycle activity and CM maturity. **f,** RNA Sequencing Analysis Workflow. RNASeq data was mapped with OLego version 1.1.5 and normalized using Transcripts per Millions analysis. featureCounts version v1.5.0-p2 was used to estimate total number of reads. Expression levels were then log transformed using algorithm depicted. ** $p < 0.01$. Mean ± SEM.

2.4.7. Injury activates proliferation in neonatal but not adult CMs

We next examined whether regeneration in neonatal injured hearts is due to clonal expansion of αMHC-expressing CMs or non-αMHC (progenitor) cells. Newborn (P0) *αMHC*^{CreER}; *R26*$^{VT2/GK}$, *βactin*^{CreER}; *R26*$^{VT2/GK,}$ and *Nkx2.5*^{CreER}*; R26*$^{VT2/GK}$ mice received tamoxifen followed by LAD ligation or sham operation 24hrs later (P1). At 21 days post-injury (dpi) the majority of the tissue was regenerated and only a small fibrotic area remained (**Figure 2.19a, Figure 2.20a-c**). We observed frequent clones of CMs in the injury and border areas of *αMHC*^{CreER}; *R26*$^{VT2/GK}$ hearts, indicating division of CMs in response to injury. CM clones were also detected in the remote zones, albeit at a lower number. Quantification of the number of clones consisting of 2 or more cells in these models did not reveal significant differences, indicating that regeneration is largely due to CM division (**Figure 2.20d-f**). Our observations support previous studies showing CM proliferation following neonatal cardiac injury[101, 102]. However, it should be noted that this model cannot exclude the possibility of de-differentiation or reversion of existing CMs into a more primitive state with subsequent proliferation.

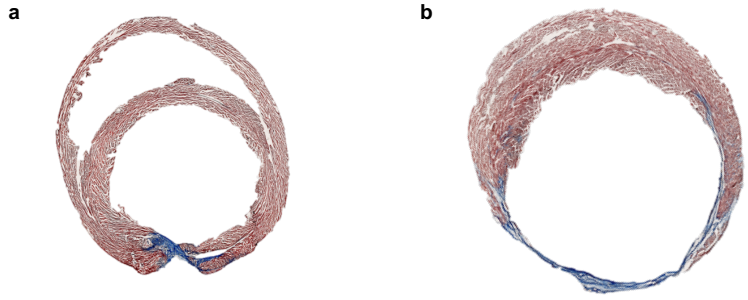

Figure 2.19: Mason's trichrome staining of infarcted hearts.
Representative images of a heart section 21 days following LAD ligation at **(a)** P1 and **(b)** 2 months of age. A small area of fibrosis (blue) is still apparent **(a)** after neonatal injury while injury in adult results in large scar formation **(b)**.

We next sought to find clonal evidence for CM proliferation in adult hearts after injury. In contrast to neonatal mice, LAD ligation performed in adults resulted in scar formation with sparse single-labeled cells and very rare 2-cell clones were detected in the infarct border zone (**Figure 2.19b**, **Figure 2.20g-i**). Overall, we observed a similar pattern of mosaic labeling, with no

evidence of clonal dominance, in *Nkx2.5*^{CreER}*; R26*$^{VT2/GK}$, *βactin*^{CreER}; *R26*$^{VT2/GK}$, or *αMHC*^{CreER}; *R26*$^{VT2/GK}$ adult hearts after injury (**Figure 2.20j-l**).

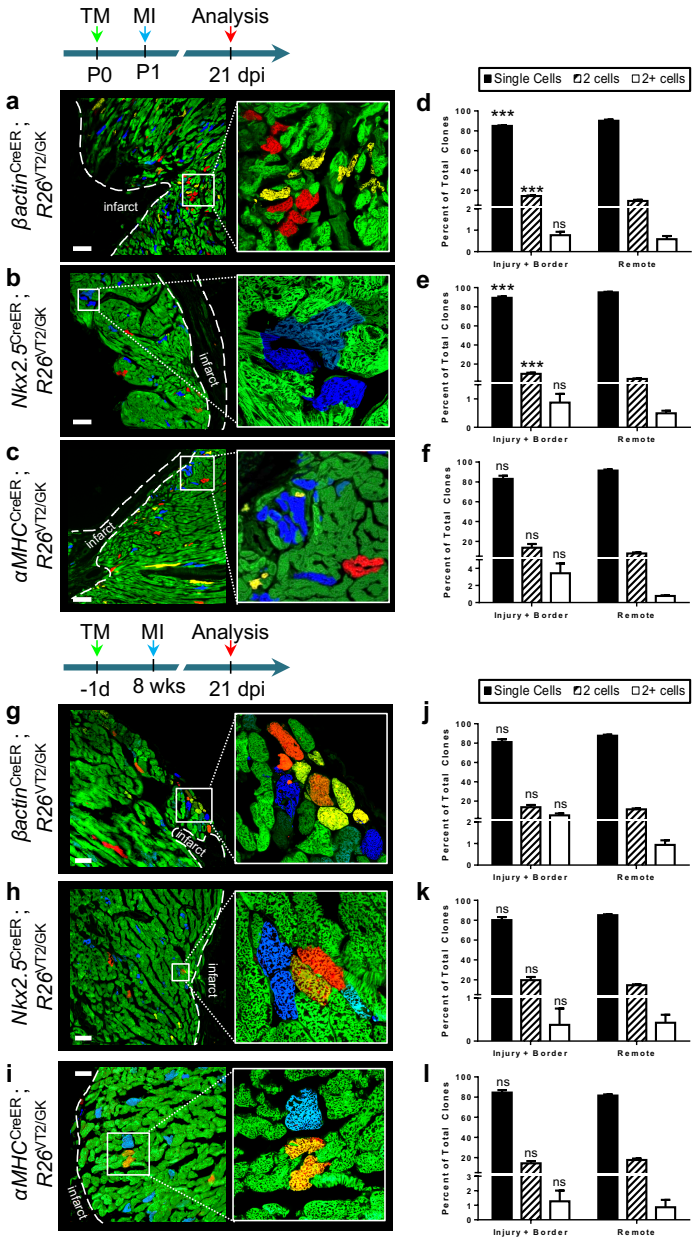

Figure 2.20: Myocardial injury activates CM proliferation in neonatal but not adult mice.
Neonatal mice underwent left anterior descending artery (LAD) ligation at P2 and clonal analysis performed 21 days post injury. Representative confocal images of **a,** *βactin*^{CreER} ; *R26*$^{VT2/GK}$, **b,** *Nkx2.5*^{CreER}*; R26*$^{VT2/GK}$ and **c,** *αMHC*^{CreER} ; *R26*$^{VT2/GK}$ heart (left ventricle) sections. Insets show close-up of boxed regions. **d-f,** Quantification of clonal formation following neonatal injury. LAD ligation was performed in 8-week-old mice (**g, h, i**), followed by clonal analysis 3 weeks post-injury. Representative fluorescent microscope images of the infarct and border zone of **g,** *βactin*^{CreER} ; *R26*$^{VT2/GK}$, **h,** *Nkx2.5*^{CreER}*; R26*$^{VT2/GK}$ and **i,** *αMHC*^{CreER} ; *R26*$^{VT2/GK}$ hearts (left ventricle). **j-l,** Quantification of clonal formation following adult injury. White dashed line marks infarct area. (Tukey's multiple comparison test), *** $p < 0.001$ to remote. All measurements shown are depicted as mean ± SEM.

2.5. DISCUSSION

Stochastic labeling using the Rainbow model offers a precise, versatile method to retrospectively examine the proliferative behavior of CMs at a single cell resolution. Utilizing this approach, we provide a direct and detailed investigation of mammalian embryonic and postnatal cardiovascular development. The existence of large clones observed during early development reflects the proliferative characteristic of progenitor cells that we also observed in early αMHC-expressing CMs. Our study points to the possibility that cardiac progenitors are able to maintain their proliferative potential for a longer span of time and contribute to a considerable portion of cardiac growth during embryonic development. Additionally, it is likely that their transition into a mature, less proliferative state occurs on a continuous, rather than discrete timescale with gradual expression of cardiac-specific markers concomitant with decreasing proliferative capacity.

Our BrdU and single cell RNA sequencing experiments support the notion of heterogeneity within αMHC-expressing CMs, particularly within the early embryonic stages. The lower proliferative capacity at E12.5 compared to E9.5 may be due to combined effects of CM maturation: reduced response to developmental growth signals and cellular migration and a shift toward processes involved in heart contraction and cellular respiration. However, congruent with the idea of heterogeneity, we were able to identify CMs at E12.5 that still maintained high cell cycle activity and displayed a more “progenitor-like” gene profile.

Since our findings demonstrate the limited ability of postnatal CMs to undergo division, we sought to determine whether myocardial injury is sufficient to reactivate their proliferative capacity. It has been suggested that the mammalian heart retains a regenerative capacity shortly after birth that diminishes with age[101-103]. Our quantification of clone sizes within *αMHC*^{CreER}; *R26*$^{VT2/GK}$, *βactin*^{CreER}; *R26*$^{VT2/GK,}$ and *Nkx2.5*^{CreER}*; R26*$^{VT2/GK}$ mice after neonatal and adult injury suggests that CM proliferation can be activated following injury early in life and that this ability is significantly limited with aging.

Potential limitations of the current study include the possibility that administration of a minimal dose of tamoxifen may not induce recombination in a very rare subset of αMHC^{+} CMs with proliferative potential in later time points. Thus, it is possible for small clones of cardiomyocytes that were not captured in the system to make sizeable contribution to murine heart growth during this time. We also cannot exclude the possibility that a small progenitor cell population exists, capable of proliferation during adulthood (in normal aging or upon injury) that was not marked by our labeling strategy. However, this is unlikely given the consistency of our observations across a large number of samples as well as the enhanced CM proliferation observed following neonatal injury.

In conclusion, we have developed a robust *in vivo* mammalian model of clonal analysis to provide important and direct insights into the source of CMs and the characteristics of progenitor cells both during development and after injury. These findings are critical for ongoing efforts to develop regenerative therapies for cardiovascular diseases[27] in which an understanding of the mechanisms that regulate or reactivate the proliferative potential of these cells is a vital aspect.

CHAPTER 3: HARNESSING THE VERSATILITY OF PLGA NANOPARTICLES FOR TARGETED CRE-MEDIATED RECOMBINATION

Ngoc B Nguyen*, Cheng-Han Chen*, Yulong Zhang, Peng Zhao,

Benjamin M Wu, Reza Ardehali

This research was originally published by Nguyen and Chen *et al*. Harnessing the versatility of PLGA nanoparticles for targeted Cre-mediated recombination. *Nanomedicine*. Jul 2019.
PMID: 31026512

3.1. ABSTRACT

Ligand-dependent Cre recombinases are pivotal tools for the generation of inducible somatic mutants. This method enables spatial and temporal control of gene activity through tamoxifen administration, providing new avenues for studying gene function and establishing animal models of human diseases. While this paved the way for developmental studies previously deemed impractical, the generation of tissue-specific transgenic mouse lines can be time-consuming and costly. Herein, we design a 'smart', biocompatible, and biodegradable nanoparticle system encapsulated with tamoxifen that is actively targeted to specific cell types *in vivo* through surface conjugation of antibodies. We demonstrate that these nanoparticles bind to cells of interest and activate Cre recombinase, resulting in tissue-specific Cre activation. This system provides a versatile, yet powerful approach to induce recombination in a ubiquitious Cre system for various biomedical applications and sets the stage for a time- and cost-effective strategy of generating new transgenic mouse lines.

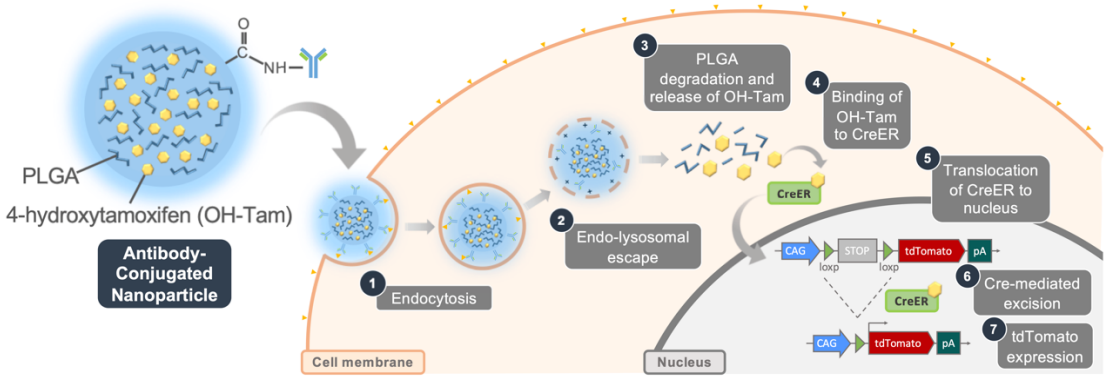

Figure 3.1: Graphical abstract.

3.2. INTRODUCTION

Within the past 50 years, nanoparticle (NP)-based carrier systems have emerged as promising vehicles for controlled drug delivery[104, 105]. The carriers are designed to protect drugs from degradation, have a large surface to volume ratio, enhance tissue penetration, and importantly, control drug release. These systems were originally in the form of liposomes but the use of polymeric materials, particularly poly(lactic-co-glycolic acid) (PLGA) gained popularity in the early 1990s[106]. The appeal of PLGA polymers as a building-block for NP fabrication resides in their desirable properties, including: (1) biocompatibility and biodegradability, (2) FDA approval for parenteral delivery, (3) capability of fine-tuning drug release profiles, (4) protection of drug from degradation, and (5) ability of surface modifications to enhance stability or targeting[105, 107-109].

A strategy for improved targeting of NPs is through surface modification with ligands that recognize specific tissue types[110, 111]. These targeting ligands play a pivotal role in navigating the NPs to desired cell types, where they can be recognized by direct ligand-receptor interaction. Examples of surface-bound ligands investigated include other polymers[112-115], antibodies[116, 117], peptides[118-120], and sugars[121, 122]. Although surface modification with various ligands have been widely studied, only a few of these systems have surpassed research-bench testing to reach

clinical development, with the majority in cancer medicine and imaging[123]. Major factors limiting the advancement of targeted NPs include an incomplete understanding of the fate of the NPs after delivery into the body, inability to load and deliver therapeutic levels of the intended drug, residual off-target effects, and the inefficiency of mass fabrication.

In this paper, we develop actively-targeted PLGA NPs that incorporates the CreER/LoxP system as a tool for tracing NP uptake and drug delivery at a cellular level. CreER/LoxP is an inducible, site-specific recombinase system comprised of the Cre recombinase enzyme fused to the estrogen receptor. This system allows for temporal control of gene expression through delivery of 4-hydroxytamoxifen (OH-Tam) to transgenic mice harboring the CreER gene. Through surface conjugation with antibodies, we provide qualitative and quantitative evidence of drug targeting at a cellular resolution using OH-Tam-loaded PLGA NPs administered to a mouse model harboring the CreER/LoxP reporter. This combined system provides a high-resolution approach to preferentially target cells of interest and for analyzing targeting efficiency. Tamoxifen-loading of targeted PLGA NPs provides an initial step for the development of a versatile, cost-effective, and timely methodology of generating transgenic mouse lines, potentially changing the current established approaches of the CreER/LoxP system.

3.3. METHODS

3.3.1. Generation of Transgenic Mouse Lines

Rosa26^{CreER};tdT$^{flox/+}$ mouse lines were obtained by crossing Rosa26-CreER mice with lineage reporter R26R-tdTomato mice. *Rosa26^{CreER};R26$^{VT2/GK3}$* mouse lines were obtained by crossing Rosa26-CreER mice with the multicolor reporter R26-“Rainbow” mice. Male and female mice ages 6-8 months were used for *in vivo* experiments unless otherwise specified. All animal studies were performed according to the guidelines of UCLA’s animal care and use committee and the National Institutes of Health Guide for the Care and Use of Laboratory Animals. Studies performed are in accordance with humane treatment of the animals.

3.3.2. OH-Tam-loaded PLGA NP Fabrication

NPs encapsulating OH-Tam were created using an emulsion-solvent evaporation technique. The “oil” phase of the emulsion was prepared by mixing 50 mg of PLGA and 4mg of 4-hydroxytamoxifenin 3ml of dichloromethane for 2 hours. 2 ml of this solution was then slowly poured into 8 ml of cold 1% polyvinyl alcohol (PVA) (in ultrapure water) solution. This solution was then sonicated on ice using a Fisher Scientific Model 500 ultrasonic dismembrator, with a microtip probe at 30% output for 120 seconds. The emulsion was stirred overnight (minimum of 12 hours) with a magnetic stir-bar at 700 rpm to allow the organic solvent to evaporate. The resulting NPs were washed of the PVA surfactant by 2 successive rinses in ddH20 (solution centrifugation at 14.5k rpm for 8 minutes followed by sonication of the pellet at 10% output for 10 seconds). With the final rinse, the NPs were resuspended in ddH20 at the desired concentration, frozen at -80ºC for 24 hours, and lyophilized for 48 hours with the FreeZone 4.5 (Labconco, Kansas City, MO, United States).

3.3.3. Serum detection of OH-Tam

Serum quantification of OH-Tam was performed using a capillary high-performance liquid chromatography/tandem mass spectrometry (HPLC-MS) method. NPs loaded with OH-Tam were delivered via lateral tail vein and allowed to circulate for 1, 12, or 60 hours. Serum was collected and prepared for HPLC analysis. The area under the curve of the peak at a retention time of 2.37 minutes was quantified, and the concentration of OH-Tam was calculated using a generated standard curve.

3.3.4. Size and surface zeta-potential measurements

To determine nanoparticle size and surface zeta-potential, lyophilized samples were suspended in PBS and dispensed into a cuvette (Malvern DTS0012) and inserted into a Zetasizer

Nano ZS (Malvern, Worchestershire, UK) where the zeta-size, polydispersity index, and zeta-potential of triplicate samples was determined. Numerical results are presented as a zeta-average size or a zeta-potential ± standard deviation.

3.3.5. In vitro Cre-mediated recombination studies

Induction of CreER-mediated recombination was studied in vitro in dermal fibroblasts from both the *Rosa26*^{CreER}*;tdT*$^{flox/+}$ and the *Rosa26*^{CreE}*R;R26*$^{VT2/GK3}$ transgenic mice models. Briefly, the ear biopsies from mice from each transgenic model were performed, cut into small pieces, and digested with Liberase Blendzyme TH and TM in Medium 199 plus DNase I and polaxamer at 37ºC for 1 hour. Cells were passed through a 70 µm cell strainer and centrifuged. The cells were resuspended in culture media (Dubecco's Modified Eagle Medium with 10% FBS and 1% Penicillin/Streptomycin) and plated on 2-well chamber slides. After the cells were cultured to approximately 60-70% confluence, PLGA(50:50) nanoparticles (containing OH-Tam) were suspended in culture media at 100 µg/ml, and the nanoparticle/culture media suspension was incubated with the cells for 24 hours. At the end of the 24-hour incubation, the media was aspirated from the chamber, and the cells were fixed by first washing with cold PBS x 3, followed by cold 4% paraformaldehyde for 15 minutes, followed by repeat cold PBS rinse x 3. VectaShield DAPI mounting medium was then placed on each slide, and the slide was sealed with a coverslip. Imaging was performed under fluorescence microscopy (Leica Microsystems, Wetzlar, Germany), with 5 20x images recorded for each experimental condition. Quantification of cells in each image was performed using ImageJ image processing and analysis software (National Institutes of Health). Numerical results are presented as a percentage of positive to total cells in field of view ± standard deviation. To examine the extent of Cre recombination in response to increasing dose of PLGA nanoparticles containing OH-Tam, dermal fibroblasts isolated from *Rosa26*^{CreER}*;tdT*$^{flox/+}$ were treated with 1, 2, 5, and 8 µg of nanoparticles and fluorescence activated

cell sorting (FACS) was performed after 24 hours to determine the percent of tdTomato^{+} fibroblasts.

3.3.6. In vivo biodistribution studies

The *in vivo* biodistribution of OH-Tam-loaded NPs was studied by intravenous injection of generated NPs into *Rosa26^{CreER};tdT$^{flox/+}$* or *Rosa26^{CreER};R26$^{VT2/GK3}$* mice. Lyophilized NPs containing OH-Tam were suspended in PBS at a concentration of 1 mg/ml. 1mg (200 µg for 5 consecutive days) of nanoparticles were injected into the lateral tail vein of each mouse model, allowed to circulate for a total of 6 days (counting from the first injection). The mice were then euthanized by cervical dislocation after anesthesia with 5% isoflurane. For each mouse, the heart, one lung, one kidney, the liver, and the spleen were harvested. The organs were then fixed in 4% paraformaldehyde overnight at 4ºC, followed by dehydration with sucrose solution for 24 hours. The organs were then mounted in OCT embedding compound, and frozen at -80ºC for 48 hours. Sections of 6-8µm thick tissue were then cut with a cryostat and mounted on standard histological slides. Imaging was then performed under fluorescence microscopy (AF6000LX, Leica Microsystems, Wetzlar, Germany) as well as confocal microscopy (TCS SP5-STED, Leica Microsystems, Wetzlar, Germany).

3.3.7. Antibody conjugation onto NP surface

NPs were “activated” for antibody conjugation by suspension for 30 min in 2-(N-morpholino)ethanesulfonic acid buffer (2 mg/ml) containing 1:1 ratio of EDC and sulfo-NHS. The solution was centrifuged and rinsed with phosphate buffered saline to remove excess reagents. 250 ug of anti-CD31 antibody (BD Biosciences, San Jose, CA, United States) was added to 1 mg of the “activated” NPs and incubated for 6 hours. Excess antibody was removed by PBS washes. NPs were suspended at a stock concentration of 10 mg/ml in 0.22um-sterile filtered PBS for tail vein delivery.

3.3.8. FACS analysis of CD11b-NPs

Targeting of bloodstream monocytes and neutrophils by anti-CD11b OH-Tam-loaded NPs was studied in the *Rosa26^{CreER};tdT$^{flox/+}$* transgenic mouse model. Briefly, anti-CD11b-conjugated NPs were prepared as described above. As a control, OH-Tam-loaded NPs that did not undergo any antibody conjugation were also prepared. For each of these conditions, 900 µg of conjugated NPs (300 µg for 3 consecutive days) were injected into the lateral tail vein of *Rosa26^{CreER};tdT$^{flox/+}$* transgenic mice. Triplicates were performed of each condition. After the fourth day, the mice were injected with heparin, and blood from each mouse was collected through retro-orbital capillary collection. For each mouse, 500 µL of blood was mixed with 10 mL RBC lysing buffer at room temperature for 5 minutes. The mixture was then centrifuged at 300g for 5 minutes, the aspirate removed, and the cell pellet gently resuspended and washed with cold PBS. This was again centrifuged at 300g for 5 minutes. The pellet was resuspended in 200 µL FACS buffer containing 1:50 AlexaFluor 647-conjugated anti-CD11b Ab. The antibody was allowed to incubate for 30 minutes at room temperature in the dark, after which excess antibody was washed off by adding 3ml of PBS and centrifuging at 300g for 3 minutes. The cells were resuspended in FACS buffer for analysis. Samples were acquired on a FACSAria Cell Sorter (BD Biosciences, San Jose, CA, United States), and data were analyzed with FlowJo software. Numerical results are presented as a percentage of tdTomato positive cells to CD11b positive cells.

3.3.9. Loading of bioactive molecules

PLGA NPs loaded with OH-Tam and pMAXGFP were generated as follows. pMAXGFP was obtained commercially (Lonza) and vortexed with 0.4 mg of mannitol and 2 mg of NH_4HCO_3 until a clear solution forms (plasmid solution). Then 25 mg of PLGA and 2.5 mg of polyethyleinimine was dissolved along with 2 mg OH-Tam in 0.25 ml of dichloromethane (PLGA solution). The plasmid and PLGA solutions were sonicated using a tip sonicator for 60s. The resulting emulsion was mixed with 2.5 ml of 2% w/v of PVA aqueous solution for 120s to form a second emulsion.

The mixture was magnetically stirred overnight at room temperature. NPs were collected by centrifugation at 13.5 krpm for 15 min and washed three times with deionized water to removed excess surfactant. 1% mannitol solution was added to disperse the NPs and the resulting solution lyophilized to generate porous PLGA NPs containing OH-Tam and pMAXGFP.

3.3.10. Clonal analysis using the Rainbow system

Rosa26^{CreER};R26$^{VT2/GK3}$ neonates two days old were injected with 10 µg of CD31-conjugated OH-Tam NPs. Twenty-eight days post injection, hearts were harvested for clonal expansion analysis.

3.3.11. Statistical analysis

Student's unpaired t-test and one-way ANOVA were used for statistical analyses. All data are presented as mean ± SEM. A probability value $p \leq 0.05$ was considered statistically significant. All analyses were performed with GraphPad Prism 5.04 (San Diego, CA, United States).

3.4. RESULTS

3.4.1. Tamoxifen loading allows for high-resolution detection of NP uptake and drug delivery in an inducible CreER mouse model

PLGA NPs were fabricated using an emulsion-evaporation technique (Figure 3.2**A**). Briefly, OH-Tam and PLGA were dissolved in dichloromethane and sonicated with a solution containing polyvinyl alcohol. OH-Tam loaded nanoparticles were extracted via evaporation and lyophilization. Scanning and transmission electron microscopy showed consistency of size and spherical shape (**Figure 3.2B**) and zetasizer analysis demonstrated particles ranging from 220-230 nm in diameter (**Figure 3.2C, D**). Surface zeta potential of the NPs was approximately -30mV, indicating stability and low risk of aggregation (**Figure 3.2E**).

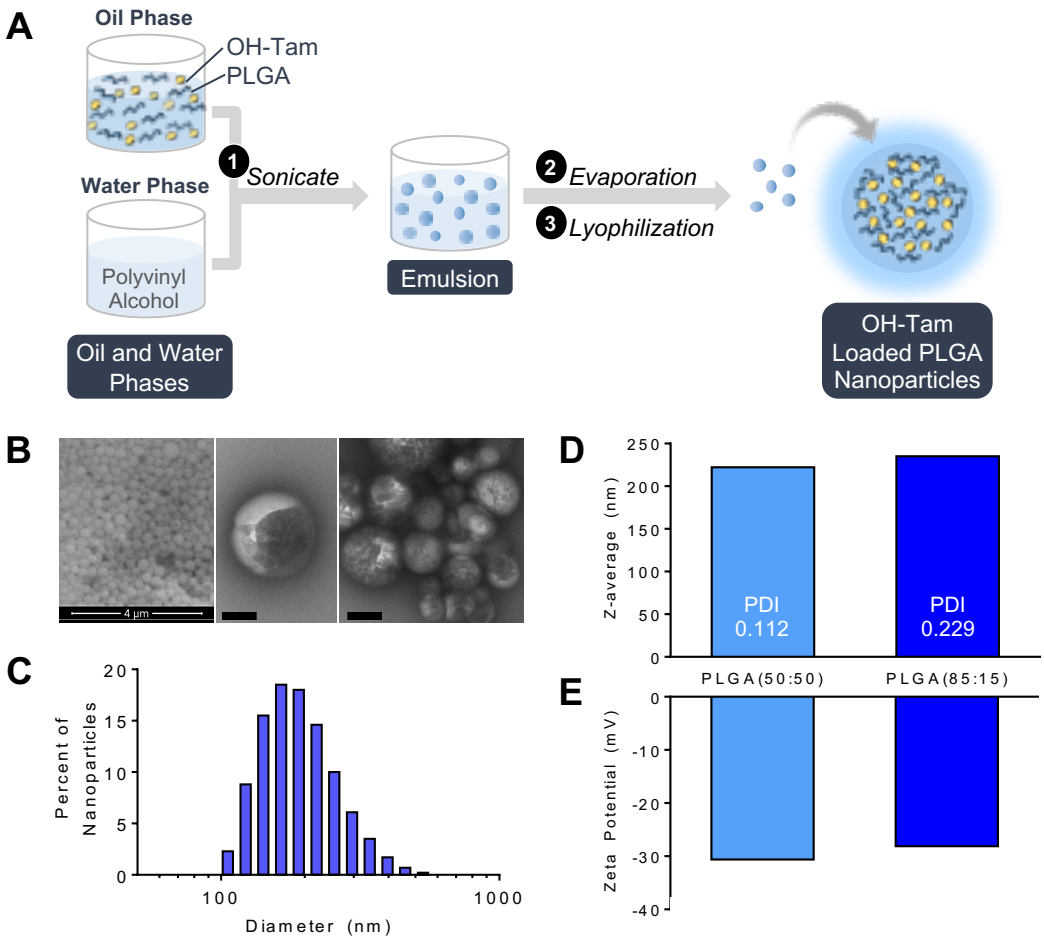

Figure 3.2: Fabrication and characterization of of 4-hydroxytamoxifen loaded PLGA NPs. **(A)** Schematic of NP generation using the emulsion-evaporation technique. **(B)** Scanning electron microscopy (*left*), transmission electron microscopy (*middle, right*) of PLGA NPs, bar = 200 nm. **(C)** Histogram of NP size distribution. **(D)** Average particle size, polydispersity, and **(E)** zeta-potential of OH-Tam-loaded PLGA(50:50) and PLGA(85:15) NPs.

To assess nanoparticle uptake and drug delivery at a cellular level, we used the inducible CreER/LoxP system as a fluorescent readout. We generated a double transgenic mouse model, *Rosa26*^{CreER}*;tdTomato*$^{flox/+}$, in which the presence of OH-Tam leads to Cre-mediated recombination and permanent labeling of cells with tdTomato (tdT) (**Figure 3.3A**). Successful delivery of OH-Tam-loaded NPs to this mouse model would lead to the expression of the reporter protein, enabling accurate and sensitive confirmation of drug uptake and release. *In vitro* drug release profiles of OH-Tam-encapsulated NPs showed an initial burst of OH-Tam release within the first hour, with ~95% of the drug released within 24 hours (**Figure 3.4A**). Modulation of

lactic:glycolic acid ratio of PLGA to 85:15 decreased the rate of drug release. Measurement of blood OH-Tam levels over the span of 5 days showed minimal drug release while in circulation (**Figure 3.4B**). To evaluate the effectiveness of the NPs in inducing Cre-recombination, OH-Tam-loaded NPs were added to cultures of dermal fibroblasts isolated from *Rosa26^{CreER};tdT$^{flox/+}$* and another independent inducible Cre/LoxP reporter mouse model, *Rosa26^{CreER};R26$^{VT2/GK3}$*. Effective uptake of NPs and subsequent release of OH-Tam within *Rosa26^{CreER};R26$^{VT2/GK3}$* fibroblasts results in Cre recombinase activity and random expression of one of three fluorescent proteins, mCerulean, mCherry, or mOrange (**Figure 3.3B**). As expected, tdT was abundantly expressed in *Rosa26^{CreER};tdT$^{flox/+}$* fibroblasts (**Figure 3.4C** and **Figure 3.3C**) and a mosaic of colors were present in *Rosa26^{CreER};R26$^{VT2/GK3}$* fibroblasts (**Figure 3.3D**). NP delivery to *Rosa26^{CreER};tdT$^{flox/+}$* fibroblasts showed a dose-dependent increase in Cre recombination (**Figure 3.4D**), as observed by an increase in the percent of tdT+ fibroblasts with greater amount of tamoxifen-loaded NPs. Additionally, as we increased the amount of OH-Tam in the encapsulated NPs, we observed an increase in tdT expression (**Figure 3.3E**). We next evaluated whether *in vivo* delivery of OH-Tam-loaded NPs results in tissue recombination. Intravenous delivery of NPs loaded with OH-Tam showed high recombination rates within the liver and spleen, and only a few cells within the heart, kidney, and lung. The biodistribution profile of OH-Tam NPs is comparable to standard intraperitoneal (IP) injection of free OH-Tam although it appears that IP delivery resulted in more recombination events within the spleen, liver, and kidney compared to the lung and heart. This observation was consistent in both *Rosa26^{CreER};tdT$^{flox/+}$* (**Figure 3.4E**) and *Rosa26^{CreER};R26$^{VT2/GK3}$* (**Figure 3.3F**) mouse models.

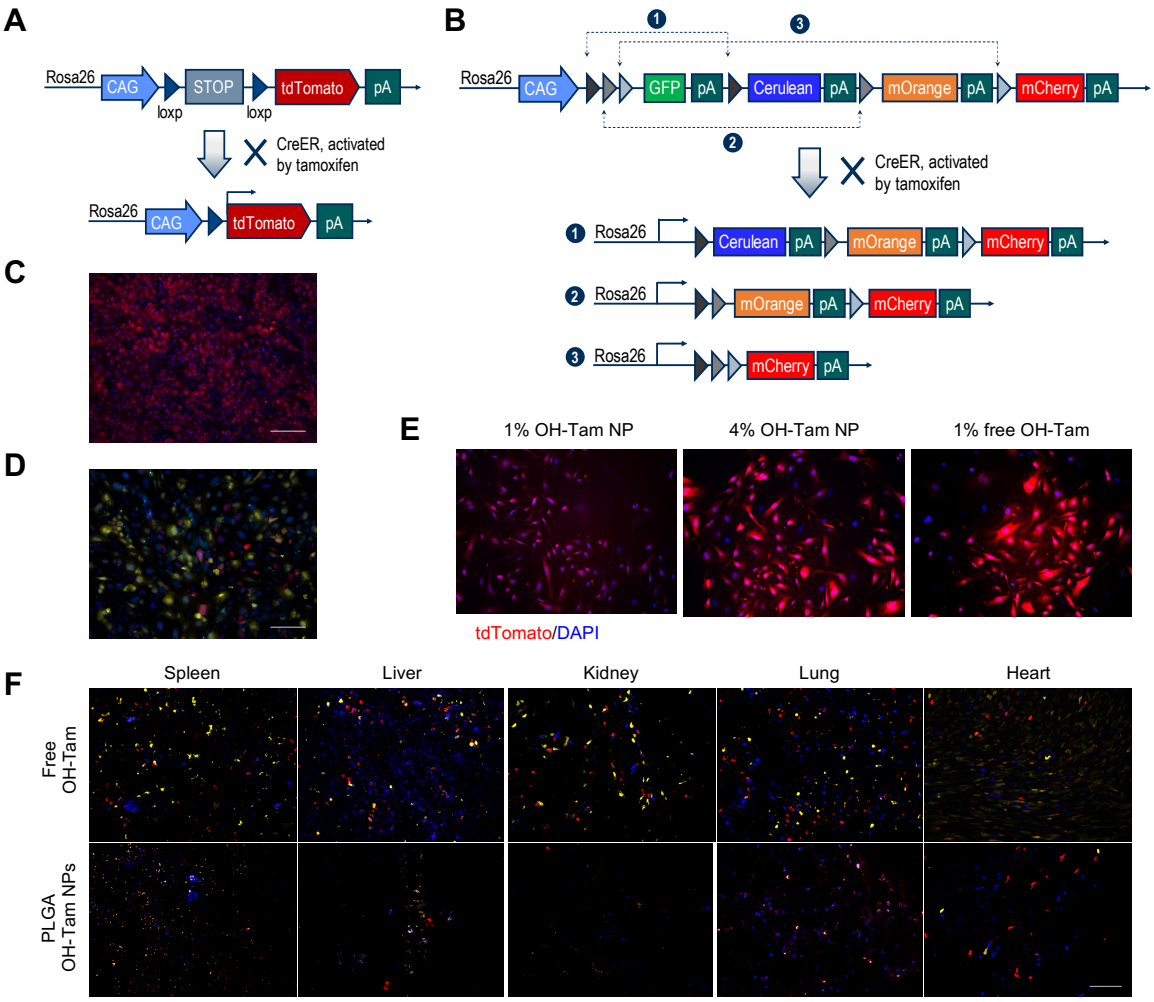

Figure 3.3: Induction of Cre recombination using OH-Tam-loaded PLGA NPs. Schematic of the inducible Cre-LoxP technology in **(A)** *Rosa26CreER;tdTF/+* and **(B)** *Rosa26CreER;R26VT2/GK3* mice. Fluorescence microscopy of dermal fibroblasts isolated from **(C)** *Rosa26CreER;tdTF/+* and **(D)** *Rosa26CreER;R26VT2/GK3* mice cultured with OH-Tam loaded NPs showing efficient recombination and expression of reporter proteins. **(E)** Dermal fibroblasts from *Rosa26CreER;tdTF/+* mice treated with NPs loaded with varying percentage (w/w) of OH-Tam compared to free OH-Tam treatment. **(F)** Comparison of recombination in various organs of *Rosa26CreER;R26VT2/GK3* mice receiving either intraperitoneal injection of free OH-Tam or intravenous administration of OH-Tam encapsulated PLGA NPs.

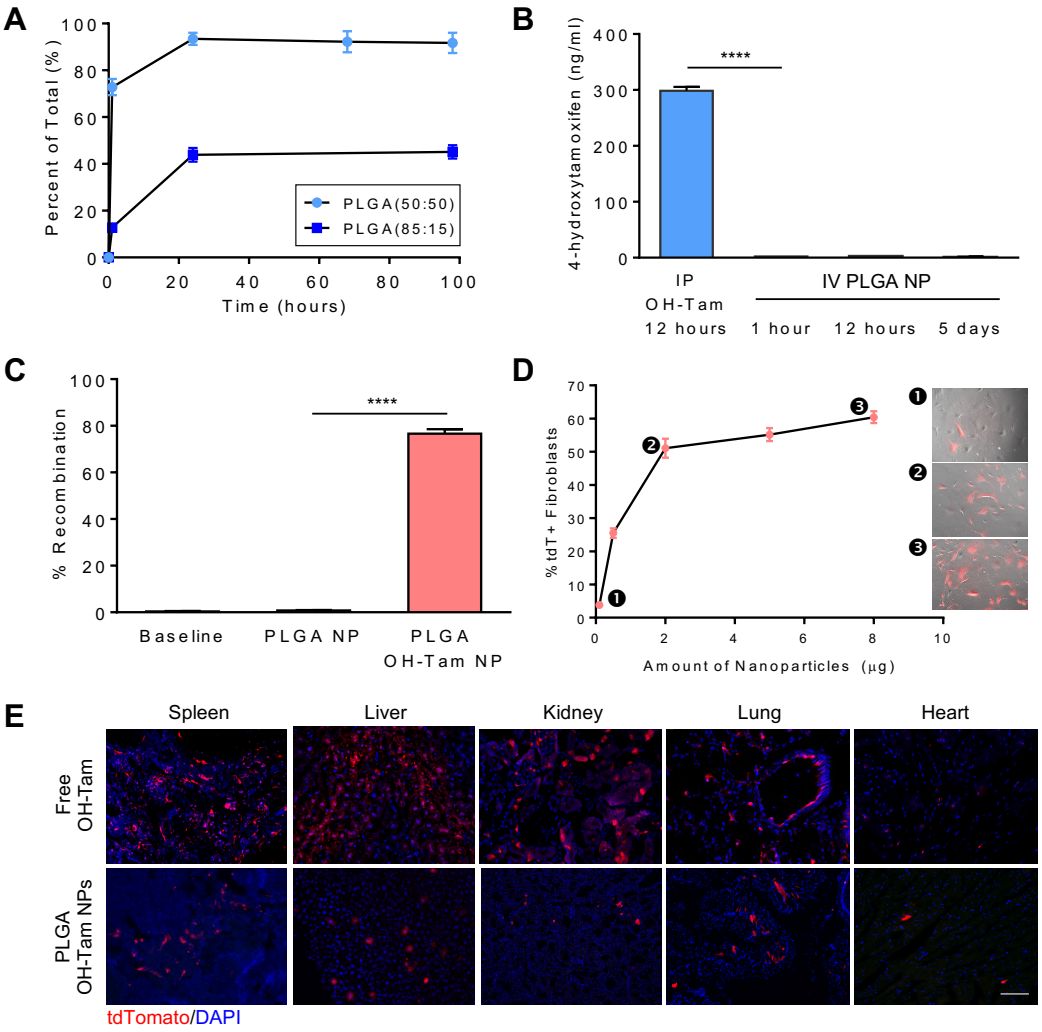

Figure 3.4: Cre-mediated recombination using PLGA NPs loaded with OH-Tam.
(A) Elution of OH-Tam from PLGA(50:50) and PLGA(85:15) NPs. **(B)** Comparison of blood OH-Tam levels between intraperitoneal injection of free OH-Tam and intravenous injection of OH-Tam encapsulated PLGA NPs over the span of 5 days. **(C)** *In vitro* quantification of recombination within *Rosa26*^{CreER};*tdT*$^{F/+}$ fibroblasts upon delivery of PLGA NPs containing OH-Tam. **(D)** Dose-dependent increase in recombination within *Rosa26*^{CreER};*tdT*$^{F/+}$ fibroblasts (as indicated by %tdT+ cells) analyzed by flow cytometry. Numbered insets depict merged brightfield and fluorescent images of cells prior to flow cytometry analysis. **(E)** Comparison of Cre-recombination in *Rosa26*^{CreER};*tdT*$^{F/+}$ mice between intraperitoneal delivery of free OH-Tam vs tail vein delivery of OH-Tam loaded PLGA NPs, bar = 100 μm. **** $p < 0.0001$

3.4.2. Antibody surface-conjugation enhances targeted-delivery of NPs

After validation of successful Cre recombination and delivery of biomolecules using PLGA NPs described above, we sought to actively target the NPs to specific cell types through NP surface conjugation of antibodies. The precise targeting of OH-Tam containing NPs to specific

cell types that harbor Cre/LoxP transgene can offer an alternative strategy to generate transgenic mice, where NP delivery would lead to tissue specific Cre-mediated recombination. This approach would enhance NP recognition by a subset of cells that express specific antigens capable of recognizing and binding to the conjugated surface antibody. Antibody conjugation was achieved using 1-Ethyl-3-[3-dimethylaminopropyl]carbodiimide hydrochloride (EDAC) linker chemistry (**Figure 3.5A**) and characterization of the conjugated NPs showed an increase in size (**Figure 3.5B**) and zeta potential (**Figure 3.5C**) consistent with antibody addition. The addition of EDAC crosslinkers almost doubled the amount of antibody binding to the surface of the NP compared to normal surface adsorption, thereby increasing efficiency of surface conjugation (**Figure 3.5D**).

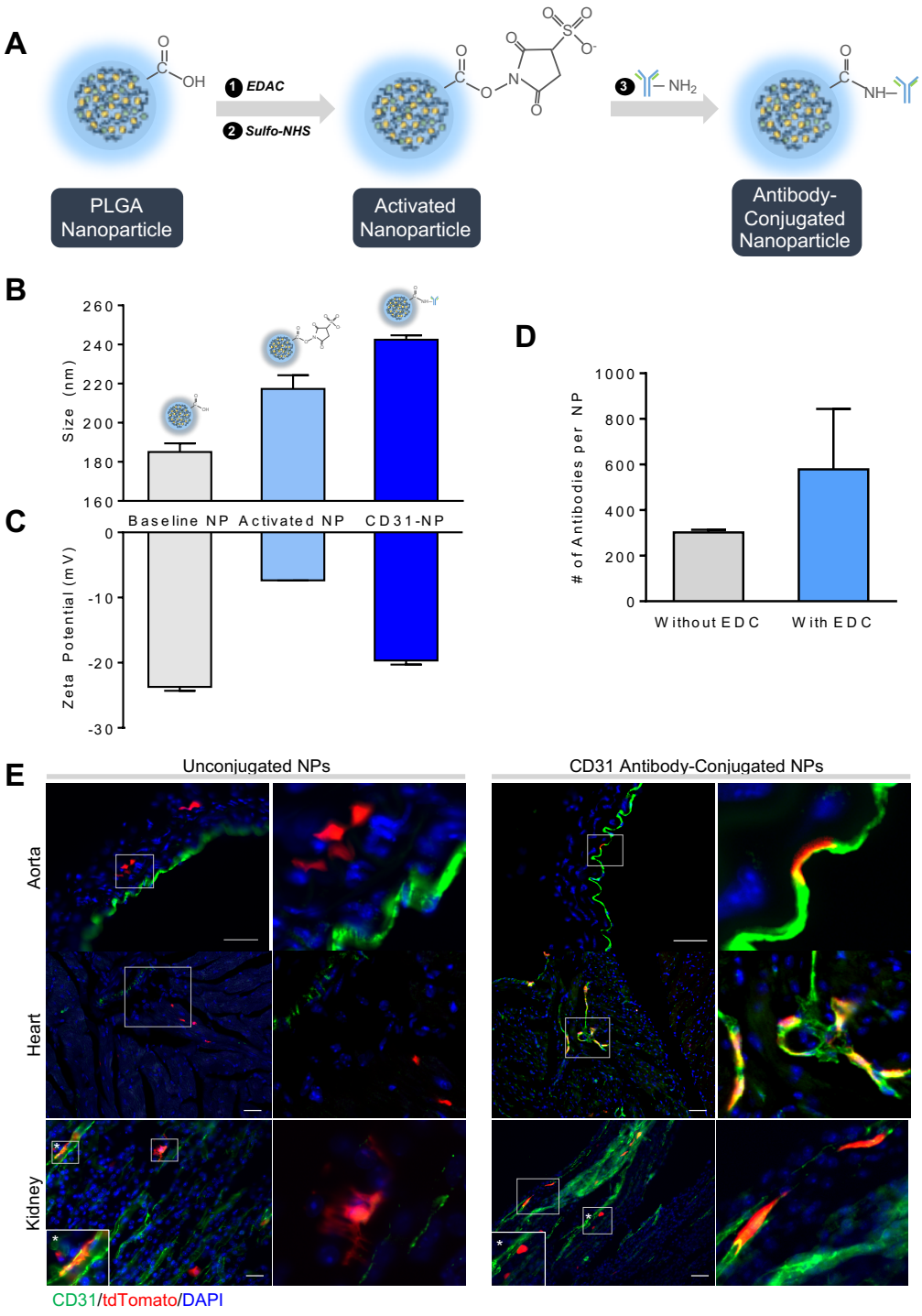

Figure 3.5: Antibody conjugation improves targeting of NPs to specific cells.
(A) Schematic of the antibody conjugation process using EDC-NHS chemistry. **(B)** Size and **(C)** zeta potential changes before and after antibody conjugation. **(D)** Quantitation of the number of antibodies conjugated to the NP surface with and without EDC chemistry. **(E)** Comparison of NP uptake and Cre recombination in the aorta, kidney, and heart between unconjugated and anti-CD31 antibody conjugated NPs loaded with OH-Tam within *Rosa26*^{CreER};*tdT*$^{F/+}$ mice, bar = 50 μm. Inset shows magnified view of boxed regions.

To test the specificity of NP uptake by cells of interest, we generated two different sets of targeted, OH-Tam-loaded NPs for delivery to (i) endothelial cells and (ii) monocytes/macrophages, using antibodies for CD31 and CD11b, respectively. First, we generated and delivered anti-CD31 antibody-conjugated NPs (CD31-NPs) to *Rosa26*^{CreER}*;tdT*$^{flox/+}$ mice. Immunofluorescence imaging showed co-localization of tdT (indicating successful recombination) in vascular endothelial cells (stained green for CD31), confirming specificity of targeting and OH-Tam release (**Figure 3.5E**). Compared to unconjugated NPs which resulted in single tdT+ cells randomly distributed within the aortas, kidneys, and hearts of the *Rosa26*^{CreER}*;tdT*$^{flox/+}$ mice, delivery of CD31-NPs led to preferential recombination events in endothelial cells. However, particularly in the kidney, we observed non-specific uptake with CD31-antibody conjugated NPs (starred inset). To further explore and quantify targeting efficiency, we conjugated anti-CD11b antibody to NPs containing OH-Tam as a way to target monocytes and macrophages within the blood. After injection of anti-CD11b-conjugated NPs (CD11b-NPs) loaded with OH-Tam, FACS analysis of blood showed a ~6-fold increase in tdT+ cells within the total CD11b+ population (**Figure 3.6A,B**) compared to untargeted PLGA nanoparticles. Again, we observed that while untargeted NPs loaded with OH-Tam resulted in cell labeling indiscriminately, CD11b-NPs led to more selective labeling of CD11b+ cells.

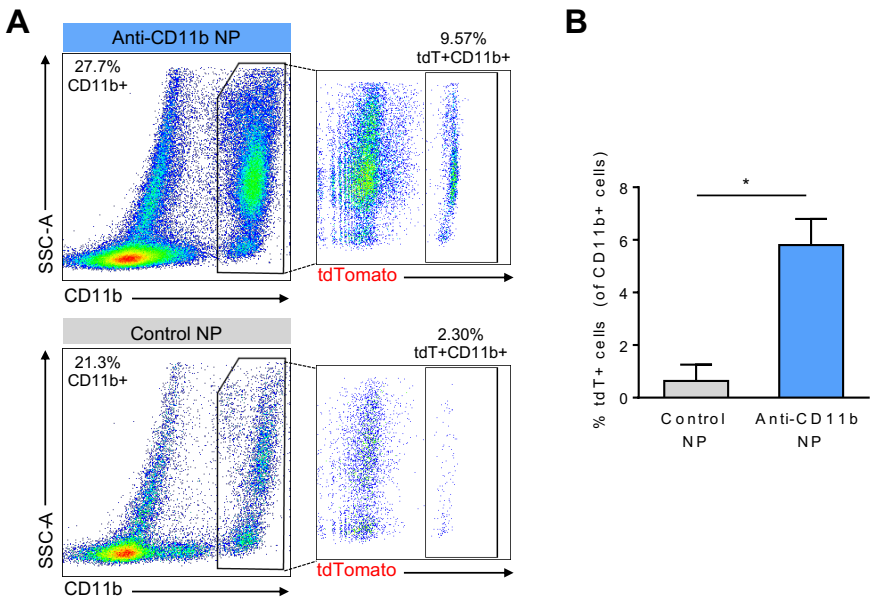

Figure 3.6: Targeting of monocytes/macrophages with CD11b-conjugated PLGA NPs. **(A)** FACS analysis of peripheral blood after intravenous delivery of CD11b-conjugated, OH-Tam loaded PLGA NPs to *Rosa26*^{CreER};*tdT*$^{F/+}$ mice. **(B)** Quantification of percent of recombined (tdT+) cells within CD11b+ cells, * $p < 0.05$.

3.4.3. Combined delivery 9of OH-Tam and Proteins/Plasmid DNA

To demonstrate the use of OH-Tam as a means of detecting effective NP uptake and drug delivery, we performed proof-of-concept applications with delivery of FITC-albumin protein and a GFP DNA plasmid. We utilized a water-in-oil-in water double emulsion method (**Figure 3.7A**) to generate these two sets of PLGA NPs. For protein delivery, PLGA and OH-Tam were dissolved together to form the oil phase and an aqueous solution of FITC-BSA comprised the first water phase. After sonication of these two phases to form a primary emulsion, another water phase consisting of PVA was used to generate a secondary emulsion from which the NPs were extracted through evaporation and lyophilization. Delivery of these NPs to cultured dermal fibroblasts from *Rosa26*^{CreER};*tdT*$^{flox/+}$ showed aggregates of FITC-albumin within recombined cells (**Figure 3.7B**). These *in vitro* observations were corroborated by *in vivo* tail vein administration of the NPs showing only FITC-BSA within recombined cells (**Figure 3.7C**). These results confirmed NP

uptake and concomitant release of both OH-Tam to mediate Cre-recombination and FITC-albumin into the cytoplasm of the same cell.

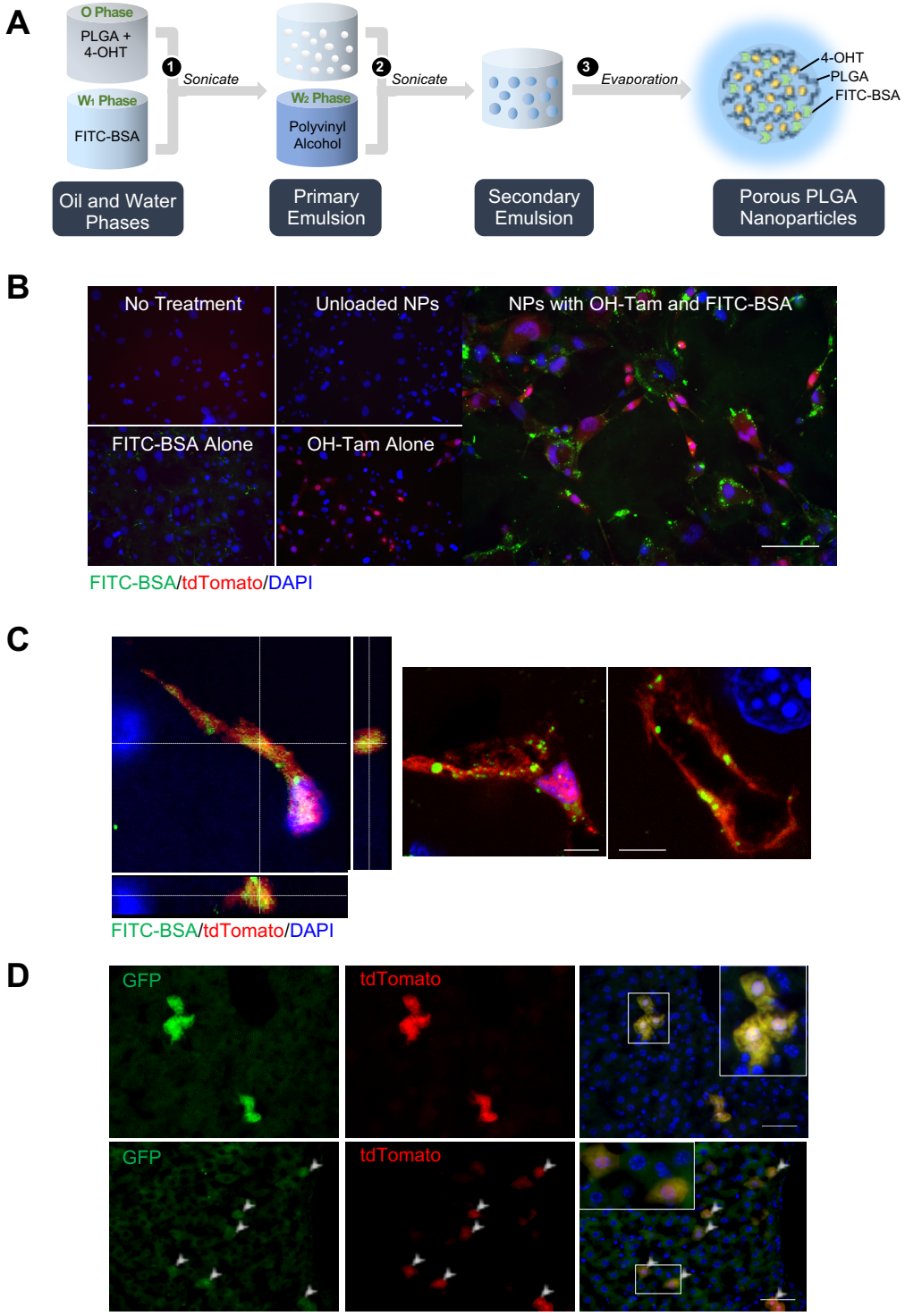

Figure 3.7: Combined delivery of OH-Tam and Proteins/Plasmid DNA.

(A) Schematic of FITC-albumin NP fabrication. **(B)** Mouse dermal fibroblasts isolated from *Rosa26CreER;tdTF/+* mice treated with NPs loaded with OH-Tam and FITC-albumin showing aggregates of FITC-albumin within recombined cells, bar = 100 um. **(C)** *In vivo* delivery of OH-Tam and FITC-BSA encapsulated PLGA NPs in *Rosa26CreER;tdTF/+* mice. Images show recombination in hepatocytes containing FITC-albumin aggregates, bar = 5 μm. **(D)** Tail vein delivery of PLGA NPs containing 4-OHT and pMAXGFP in Rosa26CreER;tdTF/+ mice. Liver section showing recombined hepatocytes expressing both tdT (red) and GFP (green), bar = 50 μm.

We achieved similar results with delivery of pMAXGFP (Lonza), a 3.5 kbp plasmid driven by a CMV promoter, which expresses an enhanced green fluorescent protein (eGFP). *In vivo* delivery of NPs containing OH-Tam and pMAXGFP into *Rosa26*^{CreER}*;tdT*$^{flox/+}$ mice revealed successful uptake of both pMAXGFP and OH-Tam within the same cells, based on GFP and tdTomato co-expression (**Figure 3.7D**).

3.4.4. Clonal expansion analysis using our targeted PLGA system

In addition to serving as a readout of effective uptake and drug release, another benefit with the loading of OH-Tam into PLGA NPs is its potential application in developmental biology, particularly for clonal expansion analysis. Our developed NPs provide an ideal platform for clonal analysis as we can examine any cell type of interest by modulating the surface antibody and adjusting the extent of recombination through dose-titration of NPs. To test this application, we delivered a limiting amount of CD31-NPs containing OH-Tam to *Rosa26*^{CreER}*;R26*$^{VT2/GK3}$ neonates to induce rare recombination events. When the neonates reached 30 days old, we collected tissues for clonal expansion analysis (**Figure 3.8A**). In this model, endothelial cell clones are expected to randomly express one of three fluorescent proteins, mCerulean, mCherry, or mOrange. Each clone of cells would be distinguishable by the fluorescent protein they express, and clonal analysis can be achieved by counting the total number of cells from each clone. Recombination was observed in endothelial cells as confirmed with CD31 staining. Clusters of cells were identified and expressed the same reporter protein, indicating clonal expansion of a parental cell that recombined after NP uptake and passed on the genetic labeling to its progeny (**Figure 3.8B**).

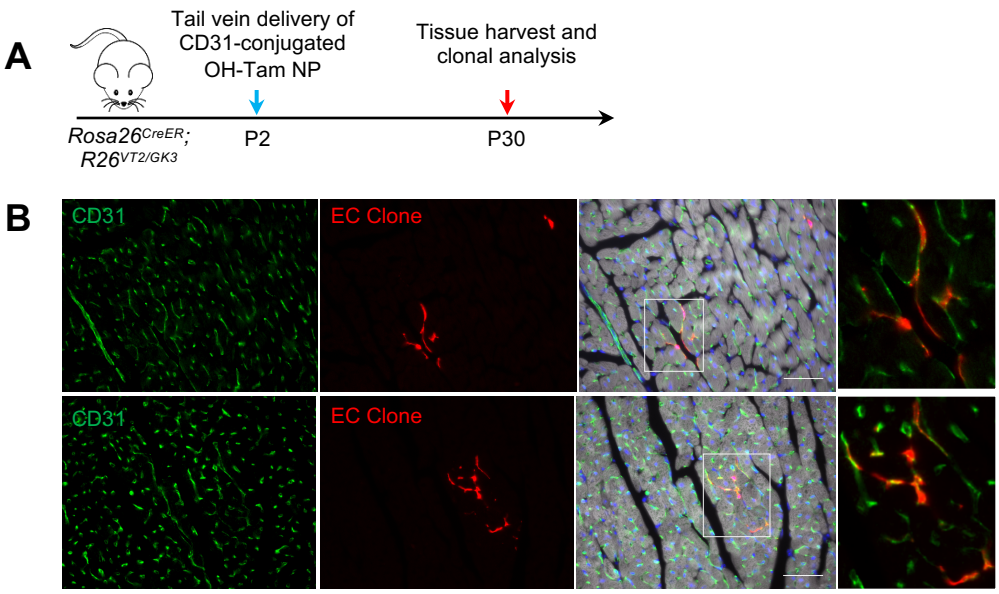

Figure 3.8: Clonal expansion analysis within Rainbow hearts.
(A) Schematic of NP delivery. Neonatal day 2 pups were injected intraperitoneally with CD31-NPs loaded with OH-Tam and hearts harvested 3 weeks post-injection for clonal analysis. **(B)** Cell clones (red) within Rosa26CreER;R26VT2/GK3 neonatal hearts identified as CD31+ from immunohistochemistry (green), bar = 50 μm.

3.5. DISCUSSION

Nanoparticles have long been utilized as a platform for targeted and controlled drug delivery. Methods to directly track nanoparticle targeting and distribution rely on imaging techniques such as fluorescence microscopy, optical imaging, or magnetic resonance imaging. However, they rarely address the success of drug delivery itself. The inducible Cre/LoxP system has been a powerful tool in developmental and molecular biology, with temporal and spatial control of gene recombination by administration of tamoxifen and utilization of tissue-specific promoters, respectively. We have combined the precision and versatility of PLGA nanoparticles as a drug delivery platform with the sensitive and robust CreER/LoxP construct to develop a system that accurately reports successful uptake and drug release. This capability is vital for determining efficiency and specificity of drug delivery, which are current limitations with NP-based carriers.

We used PLGA to design our NP system for several reasons, including their biocompatibility, versatility in modulating their physico-chemical properties, and their FDA approval for clinical use. As the constituent building blocks of PLGA are monomers of lactic acid and glycolic acid, its degradation products are therefore physiological molecules naturally processed during the citric acid cycle. The double-emulsion method for NP fabrication allows for the encapsulation of both hydrophilic as well as hydrophobic compounds, increasing its versatility for drug delivery. We validated this strategy by co-delivery of DNA plasmids along with OH-Tam. This approach could be applied to a variety of biological systems, in which a reporter gene will permanently mark cells that successfully received DNA plasmids. Additionally, this method of fabrication allows for fine-tuning of payload encapsulation, enabling adjustment in the amount of OH-Tam or drug delivered in a specified dose of NP. Utilizing this method, we provide proof-of-concept for delivery of both macromolecules as well as plasmid DNA.

An important extension to efficient and specific reporting of drug delivery is the applicability of our system in the generation of tissue-specific transgenic mice for biomedical studies. Alteration of mouse genome by gene-targeting approaches has greatly facilitated studies in developmental and cellular biology. Additionally, transgenic mouse models can be utilized to turn on a reporter gene to track individual cells for lineage tracing. A major technical advance in this field has been the development of models that allow for control of the timing, cell-type, and tissue-specificity of gene activation or repression. However, the generation of tissue-specific CreER/LoxP mouse models is a rigorous process that can be costly and time-consuming. Therefore, the development of a system that combines a generic CreER/LoxP mouse with ‘smart’, OH-Tam-loaded NPs capable of targeting specific cell types would convert this generic mouse into a tissue-specific transgenic mouse. This is advantageous for several reasons. First, it circumvents the need to generate and maintain different transgenic mice with cell-type specific promoters. Second, it allows for the use of a single mouse model, reducing possible genetic and phenotype variability. Finally, by using nanoparticles with several different ligands, it may be possible to induce

recombination within more than one cell type of interest. We have shown that by utilizing an actively-targeted approach via surface conjugation of antibodies, we can improve delivery of biomolecules to specific cells within the body. Our study sets the stage for a timely, cost-effective, and novel application of NPs in the potential generation of transgenic mouse models. We also envision their applicability in improving CRISPR/Cas9 technology for targeted delivery of Cas9 mRNA, guide RNA, or donor DNA to induce gene editing in specific cell types.

However, there are limitations with our current system that need to be addressed before it can be fully applied to biological systems. First, targeting to specific cell types was not achieved at a high efficiency, since there is non-specific uptake of nanoparticles, especially within the reticuloendothelial system. We observed recombination events in the liver and spleen resulting from high trafficking of the nanoparticles within these organs. Second, it is well established that there is rapid protein adsorption onto surfaces of circulating nanomaterials, known as the protein corona[124-126]. The coating of nanoparticles with circulating proteins and peptides may adversely affect the targeting of the particles to the cells of interest and may modify NP size, surface charge, surface composition, and functionality[127]. And finally, in order to utilize this system to generate tissue-specific transgenic mice, surface antibodies to the tissue of interest must be available for nanoparticle surface modification. While further studies are needed to refine the targeting efficiency, particularly within solid organs, the versatility and sensitivity of our targeted PLGA NP system provides it with the potential to significantly improve the cost and time of biomedical research. Together, our results demonstrate that NP surface antibody conjugation improves recognition and uptake by cells that express specific ligands to the surface receptor. In combination with OH-Tam loading, this system holds promise for future application of inducing Cre-recombination in specific cell types to generate transgenic models and perform developmental studies such as clonal expansion analysis.

CHAPTER 4: PROTECTIVE EFFECTS OF NEONATAL PLASMA ON CARDIAC ISCHEMIA-REPERFUSION INJURY

This work has not been submitted to a peer-reviewed journal. It is written by Ngoc B Nguyen and reviewed by committee members.

4.1. ABSTRACT

In the heart, age-related changes are important risk factors for ischemic heart disease, which is the leading cause of morbidity and mortality in the United States. Recent studies have shown that circulating factors found in young blood can partially reverse age-related loss of cognitive function, restore muscle dysfunction, and improve strength and endurance exercise capacity. In the clinical setting, it is observed that pediatric patients are able to restore baseline cardiac function after injury faster than in the aged population. Given these observations, as well as the known ability of the heart to regenerate after apical resection within the first 7 days of life, we examined whether neonatal plasma contains “pro-youthful” factors that offer a protective milieu and prevent irreversible myocardial damage in adult mice after ischemia-reperfusion injury. We observe reduced scar sizes, improved cardiac function, and increased vascular density in hearts of adult C57BL/6 mice treated with neonatal plasma two months post-injury. Neonatal plasma also reduced the percentage of TUNEL+ cardiomyocytes after exposure to hypoxia and improved the angiogenic ability of endothelial cells as measured by tubal formation assay. Single cell RNA sequencing and gene ontology analysis revealed a possible role of neonatal plasma in downregulation of apoptosis-related pathways. Mass spectrometry identified several thymosin-related proteins to be differentially abundant between neonatal and old plasma. Among many factors, several thymosin-related proteins were deemed promising. Validation studies using an *in vitro* hypoxia assay showed reduced numbers of apoptotic cardiomyocytes when treated with recombinant forms of these candidate proteins. Our study offers critical insights into a more

relevant neonatal period for assessment of young circulating factors and highlights potential beneficial role(s) of thymosin proteins in ischemic heart disease. This study also brings to light the potential of neonatal plasma as a rejuvenative therapy for cardiovascular as well as other age-related diseases.

4.2. INTRODUCTION

It is well established that aging drives the impairment and degenerative processes of various organ systems within the body. Much of this has been attributed to reduced responsiveness of stem/progenitor cells, particularly within muscle, blood, liver, and brain[128-132]. These critical cell types, with their ability to self-renew and produce new adult cells, play a vital role in the maintenance of normal tissue function and regeneration in response to injury or disease[133]. For instance, studies suggest that the decline in skeletal muscle function and mass with age is due to reduced ability of muscle satellite/progenitor cells to regenerate muscle fibers[73]. Other cell types previously associated with low regeneration rates are cardiomyocytes in the heart and neurons of the central nervous system, both of which are classified as terminally differentiated and precluded from re-entering the cell cycle. There is a general consensus that the existence of endogenous cardiac stem cells is very limited and unlikely to be a source of cardiac regeneration[45-47]. Recent studies have shown that adult cardiomyocytes can be stimulated to proliferate under specified cues, albeit at low rates[60, 134, 135]. These pivotal studies have now shifted the focus toward finding ways to induce the proliferation of existing cardiomyocytes as a means of cardiac therapy.

On the flip side, young age is generally associated with high regenerative ability and increased cellular plasticity[136]. In the context of the heart, it has been shown that fetal and neonatal cardiomyocytes have the ability to proliferate and that cardiac regeneration in the face of injury occurs without scar formation[65-67]. While the cellular mechanisms driving these changes are not well understood, researchers have pondered whether exposure of aged cells to a young

environment can reverse the degenerative processes associated with aging. In recent years, there has been a renewed interest in examining this phenomenon, in which researchers have tuned to parabiosis as a model to examine effects of shared circulation. Much of the initial studies were within the neurology field in which heterochronic parabiosis showed that exposure to young circulation improves long-term potentiation of the dentate gyrus[137], enhanced learning, memory, and cognitive function[138-140], remyelination[141], as well as vascular remodeling and neurogenesis[75] within the aged mouse. It is postulated that the beneficial effects of young plasma were likely soluble, heat-labile factors as heat denaturation mitigated these effects[138]. These studies fueled further investigations within other organ systems, particularly in the muscle and cardiac fields. Conboy et al[73] examined the efficacy of muscle regeneration in young and aged mice in heterochronic and isochronic pairings after hind limb injury. They noted that parabiosis with young mice significantly enhanced the regeneration of muscle in old partners and induced muscle stem cell activation, with the appearance of nascent myotubes similar to those found in young mice. In addition to improving regeneration in response to injury, exposure to young systemic environment was shown to reverse age-related pathology. Loffredo et al examined hearts of heterochronic pairings and noted a reversal of age-related cardiac hypertrophy after 4 weeks[77].

Together, these studies point to the possibility that there may be specific factors in young blood that offer a protective milieu and prevent age-related degeneration. However, the identification of these “pro-regenerative” factors remains elusive. Of note, prior studies have categorized “young circulation” to a much later period of development during which “pro-regenerative” factors may have already declined. In this study, we aim to understand the role of systemic factors in the context of cardiac ischemia-reperfusion injury, with a focus on the neonatal period during which the heart’s ability to fully regenerate after injury is well established[67]. Our results show that neonatal plasma significantly improved cardiac function and scar sizes of adult mice after ischemia-reperfusion injury and that these effects may be mediated by thymosin proteins via apoptosis-associated pathways. Our study highlights a distinct proteomic profile of

neonatal plasma and brings to light its potential as a rejuvenative therapy for cardiovascular as well as other age-related diseases.

4.3. METHODS

4.3.1. Neonatal and adult mouse plasma collection

Neonatal mice (postnatal days 2-5) were anesthetized on ice for 2 minutes. Aged mice were anesthetized using a 3% isoflurane chamber. A thoracotomy was then performed to reveal the heart for cardiac puncture blood collection into a K_2EDTA-microtainer (BD, 365974). Blood samples were centrifuged 10 min at 1000 x g and supernatant (plasma portion) collected and stored at -80°C until use.

4.3.2. Ischemia-reperfusion injury and plasma administration

Ischemia-reperfusion injury was induced via permanent ligation of the left anterior descending artery (LAD). C57BL/6 mice six months of age were anesthetized by intraperitoneal injection of ketamine (100 mg/kg) and xylazine (10 mg/kg). A left thoracotomy was performed through an incision between the fourth and fifth intercostal muscles followed by removal of the pericardium. An 8-0 silk suture was used to temporarily ligate the LAD and released after 45 minutes. Post-operative discomfort was treated with buprenorphine (0.03-0.06 mg/kg). Sham-operated mice were submitted to the same procedure lacking the LAD ligation. Plasma (200 µl each dose) was administered via the tail vein on day of surgery and daily for designated subsequent number of days. All animal studies were performed according to the guidelines of UCLA's animal care and use committee and the National Institutes of Health Guide for the Care and Use of Laboratory Animals. Studies performed are in accordance with humane treatment of the animals.

4.3.3. Echocardiography

Transthoracic echocardiography was performed at baseline and 60 days post injury using the Vevo 770 high resolution ECHO system equipped with a 35 MHz transducer. Chest fur from mice were removed and then animals were anesthetized with vaporized isoflurane (2.5% for induction, 1.0% for maintenance) in oxygen and body temperature maintained at 37°C using a heating pad. Heart rates were maintained between 500 – 600 beats per minute throughout the imaging period. The probe was placed along the short axis of the left ventricle with the papillary muscles providing a guide for the proper depth. 2D images were captured to measure internal wall dimensions during both systole and diastole. Images were analyzed using the Vevo 2100 software. The left ventricle (LV) chamber dimensions and posterior wall thickness were obtained from M-mode images; LV systolic function was also assessed from these measurements by calculating ejection fraction (EF, stroke volume/end diastolic volume) and fractional shortening (FS).

4.3.4. Heart weight, body weight, and tibia length measurements

Sixty days post-IR injury, mice from each experimental group were sacrificed and their body weights recorded. Hearts were removed, perfused in PBS, and wet weights measured. Additionally, the right tibia of each mouse was removed and measured with a caliper.

4.3.5. Tissue processing

Hearts were harvested, perfused and incubated in 4% (vol/vol) paraformaldehyde (12-18 hours at 4^{o}C) followed by incubation in 30% (wt/vol) sucrose in PBS at 4^{o}C for 12-18 hours. The samples were removed from the sucrose solution and tissue blocks were prepared by embedding in Tissue Tek O.C.T. (Sakura Finetek, 4583). Blocks were kept frozen in -80^{o}C. Frozen whole heart blocks were sectioned into 7-10 μm thick sections with a Leica CM1860 cryostat and mounted on Superfrost/Plus slides (Fisher Scientific, 12-550-016).

4.3.6. Histology and immunofluorescence

Masson's trichrome staining (Sigma, HT15-1KT) was performed according to the manufacturer's instructions and images were taken of the entire cross-section of the heart using bright-field microscopy (Leica). ImageJ software[142] was used to quantify fibrosis area by comparing the area of blue (collagen) staining to the total pink/red (normal tissue) area of the left ventricle.

For immunohistochemistry, sections were washed three times with PBS followed by permeabilization with 0.25% TritonX (Fisher Scientific, BP151-100) for 10 minutes. Samples were blocked for 30 min in 10% goat serum/PBS followed by incubation with primary antibodies overnight at 4°C. Antibodies against α-sarcomeric Actinin (1:400, Sigma, A7811), pHH3 (1:800, Cell Signaling Technology, 9701S), and periostin (1:150, R&D Systems, AF2955) were used. Secondary antibodies (1:150, Invitrogen) were incubated for 1 hour at RT. Isolectin B4 (Vector Laboratories, DL-1207) was used to visualize vascular density. Slides were mounted with DAPI-containing mounting media (Vector, H-1200).

4.3.7. In vitro hypoxia assay

HL-1 cardiomyocytes (Sigma, cat. SCC065) were maintained in growth media consisting of 10% FBS in Claycomb Media (Sigma, cat. 51800C) supplemented with 10 mM norepinephrine (Sigma, cat. A0937) and 200 mM L-glutamine (Gibco, cat. 25030081). Primary cardiac fibroblasts were isolated from Col1a1GFP/+ mice 2 months of age. Mice were injected with heparin prior to sacrifice and the heart collected. The tissue was then cut into 1-2 mm pieces and digested with Liberase Blendzyme TH and TM (Roche, cat. LIBTM-RO) in Hank's Balanced Salt Solution (HBSS) (Gibco, cat. 1417507) supplemented with DNAse I and polaxamer (10 mg/ml, Sigma, cat. 16758) in 37°C for 1h. Cells were passed through a 100 μm cell strainer and centrifuged at 300 g for 5 min. Cells were resuspended in 20% FBS/DMEM and transferred to a 10 cm dish precoated with 0.1% gelatin. Media was changed the next day to 10% FBS/DMEM and cells

maintained in this media until start of experiment. HL-1 or Col1a1 fibroblasts were seeded into 96-well plates at a density of 17,000 cells/well and 5,000 cells/well, respectively. 24 hours after plating, cells were switched to serum starvation (1% serum) media and placed in a hypoxia chamber flushed with 1%O_2/10%CO_2/balanced N_2 for 3 min at a rate of 4 L/min. After 6 hours, cells were removed from the chamber and media switched to either normal growth media or media containing recombinant protein with or without EdU.

4.3.8. EdU and live/dead assay

EdU incorporation and detection were performed according to manufacturer's instructions (Invitrogen, C10640). Cells were labeled with EdU diluted in PBS (5 μM). After labeling period, cells were fixed in 4% paraformaldehyde followed by permeabilization with 0.5% Triton X-100. Wells were washed twice with 3% BSA in PBS. The Click-iT reaction cocktail was prepared according to instructions and cells were incubated with this solution for 30 min at room temperature. Cells were washed with 3% BSA in PBS to remove the reaction cocktail and DAPI added for imaging. To label live and dead cells, calcein AM (Thermo Fisher Scientific, C3099) and DAPI, respectively, were added to growth media and incubated for 10 minutes prior to imaging.

4.3.9. Imaging acquisition and quantification

Fluorescent images were acquired with Leica fluorescence inverted microscope DMI6000B equipped with an EL6000 light source. For 96-well hypoxia assay, 5 images per well were taken at 10x magnification, with 4 technical replicates per treatment condition. Image quantification was performed using ImageJ's "threshold" and "analyze particles" functions. Assessment of live/dead was determined as the number of DAPI+ cells/ HPF. EdU and pHH3 quantification were recorded as the number of EdU+ or pHH3+ nuclei over the total number of DAPI.

4.3.10. BrdU and annexin flow cytometry

I/R injury was performed as described above on C57BL/6 mice six months of age and 200 µl of plasma or saline were administered intravenously on day of surgery and for 4 consecutive days following. Mice were supplied BrdU in their drinking water (1 mg/mL) for 3 days. Intracellular staining for BrdU was performed in accordance to manufacturer's instructions (BD, 552598). In short, hearts were isolated and digested into single cells. Cells were fixed and permeabilized in Cytofix/Cytoperm Buffer (BD, 554714), followed by incubation in Cytoperm Permeabilization Buffer plus (BD, 561651). Cells were then exposed to fluorescent anti-BrdU antibody, washed, resuspended in staining buffer, and analyzed using a BD FACSAria II flow cytometer. For annexin V labeling, cells were stained with FITC-Annexin V antibody (BD, 556419). Thy1 (eBioscience, 47-0900-82) and CD31 (eBioscience, 25-0311-81) antibodies were used to gate fibroblast and endothelial cell populations, respectively.

4.3.11. Single cell RNA sequencing

I/R injury was performed as described above on C57BL/6 mice six months of age and 200 ul of plasma or saline were administered intravenously on day of surgery and for 4 consecutive days following. Sham surgery with no injections served as control. On day 7 after surgery, hearts were collected and perfused with 30 ml each of HBSS. The left ventricle of each heart was obtained and the tissue chopped into 1-2 mm pieces and digested with Liberase Blendzyme TH and TM (Roche, cat. LIBTM-RO) in Hank's Balanced Salt Solution (HBSS) (Gibco, cat. 1417507) supplemented with DNAse I and polaxamer (10 mg/ml, Sigma, cat. 16758) in 37°C for 45 minutes. Cells were passed through a 100 µm cell strainer, enzymes deactivated with 1 ml FBS, and centrifuged at 300 g for 3 min. Cells were resuspended in 0.04% BSA/PBS at approximately 1 million cells/ml for capture using the 10X Genomics Chromium Single Cell v3.0 platform. cDNA libraries were sequenced together on one lane of the Illumina NovaSeq.

Digital expression matrix was generated by de-multiplexing, barcode processing, and gene unique molecular index counting using the Cell Ranger v3.0 pipeline and the mouse mm10 reference genome. Cells that express less than 200 genes, and genes detected in less than 3 cells were filtered out. The Seurat 3.0 R toolkit for single cell genomics was used to analyze sequencing results. Downstream analysis was restricted to cells associated with at least 1150 unique molecular identifiers (UMIs) and less than 50 percent mitochondrial genes. Known marker genes for each cell type were used to identify cell clusters: cardiomyocytes (*Tnnt2, Actn2, Myl2, Myl7*), fibroblasts (*Ddr2, Col1a1, Pdgfra, Tcf21*), endothelial cells (*Pecam1, Tek, Cdh5, Mcam*), immune cells (*Cd48, Cd68, Itgam, Ptprc*), smooth muscle (*Acta2, Cnn1, Myh11, Tagln*), and pericytes (*Notch3, Cspg4, Pdgfrb, Rgs5*). Smooth muscle and pericytes were later grouped into one cluster labeled as MCs. 'FindMarkers' function was used to determine differential gene expression between clusters of interest. Pseudotime analysis was performed using Monocle 3.0.

4.3.12. Mass spectrometry

High abundance proteins were depleted from plasma samples according to manufacture instructions (ProteoExtract Albumin Removal Kit, Calbiochem, 122640). Samples were digested with trypsin (Promega, V1061) and labeled with TMT Label Reagents (TMT10plex Isobaric Label Reagent Set, ThermoFisher, 90110). Digested samples were fractionated using spin columns and elution solutions of varying percentages of acetonitrile in a 0.1% TEA solution. Nano LC was performed using the Easy-nLC1000 (Thermo Fisher Scientific, LC120) instrument followed by mass spectrometry using the Obitrap Q Exactive^{TM} mass spectrometer (Thermo Fisher Scientific, IQLAAEGAAPFALGMBCA) with resolution set at 70000 at 400 m/z and precursor m/z range of 300-1650. MS files were analyzed and searched against mouse protein database based on the species of the samples using Maxquant (1.5.6.5). The parameters were set as follows: the protein modifications were carbamidomethylation (C) (fixed), oxidation (M) (variable); the enzyme specificity was set to trypsin; the maximum missed cleavages were set to 2; the precursor ion

mass tolerance was set to 10 ppm, and MS/MS tolerance was 0.6 Da. Only high confident identified peptides were chosen for downstream protein identification analysis. Differentially abundant proteins between neonatal and aged mouse plasma were identified by comparing the average of normalized intensities within each sample group and calculating the ratio of neonatal over aged mouse plasma. Increased and decreased abundance proteins in neonatal compared to aged plasma were identified as ratios > 2.0-fold and < 0.5-fold, respectively. Pathway and molecular function analysis were performed using Metascape[143].

4.3.13. Statistical analysis

Statistical significance was determined by using student's t test (unpaired, two-tailed) or one-way ANOVA in GraphPad Prism 8 software. Results were significant at $p < 0.05$ (*), $p < 0.01$ (**), $p < 0.001$ (***), and $p < 0.0001$ (****). All error bars are depicted as SEM.

4.3.14. Data availability

The authors declare that all data supporting the findings of this study are available within the article and its supplementary information files or from the corresponding author upon reasonable request.

4.4. RESULTS

4.4.1. Neonatal plasma improves cardiac function, reduces scar size, and increases vascular density of mouse hearts after I/R injury

To determine whether systemic factors found in neonatal plasma may offer protection from scar formation and heart failure after ischemic injury, experimental I/R on mice 6 months of age was induced by ligation of the left anterior descending artery (LAD) and release after 45 minutes. Neonatal plasma collected from mice 2-5 days old were intravenously administered on day of surgery and for 5 consecutive days following (**Figure 4.1a**). Functional studies at baseline and 60

days post injury showed improvement in ejection fraction and fractional shortening in groups receiving neonatal plasma, whereas denatured neonatal plasma and saline controls offered no significant protection from left ventricular dysfunction (**Figure 4.1b,c and Figure 4.2a**). Additionally, assessment of fibrosis by Masson's trichrome revealed a reduction in infarct size in mice receiving neonatal plasma (**Figure 4.1d,e** and **Figure 4.2b,c**). Quantification of isolectin at border zones as assessment of capillary density showed a significant increase in the number of capillaries in hearts treated with neonatal plasma compared to saline or denatured plasma controls (**Figure 4.1f,g**). Despite the decrease in scar sizes, neonatal plasma treatment did not affect periostin expression, a marker of activated fibroblasts (**Figure 4.1h,i**).

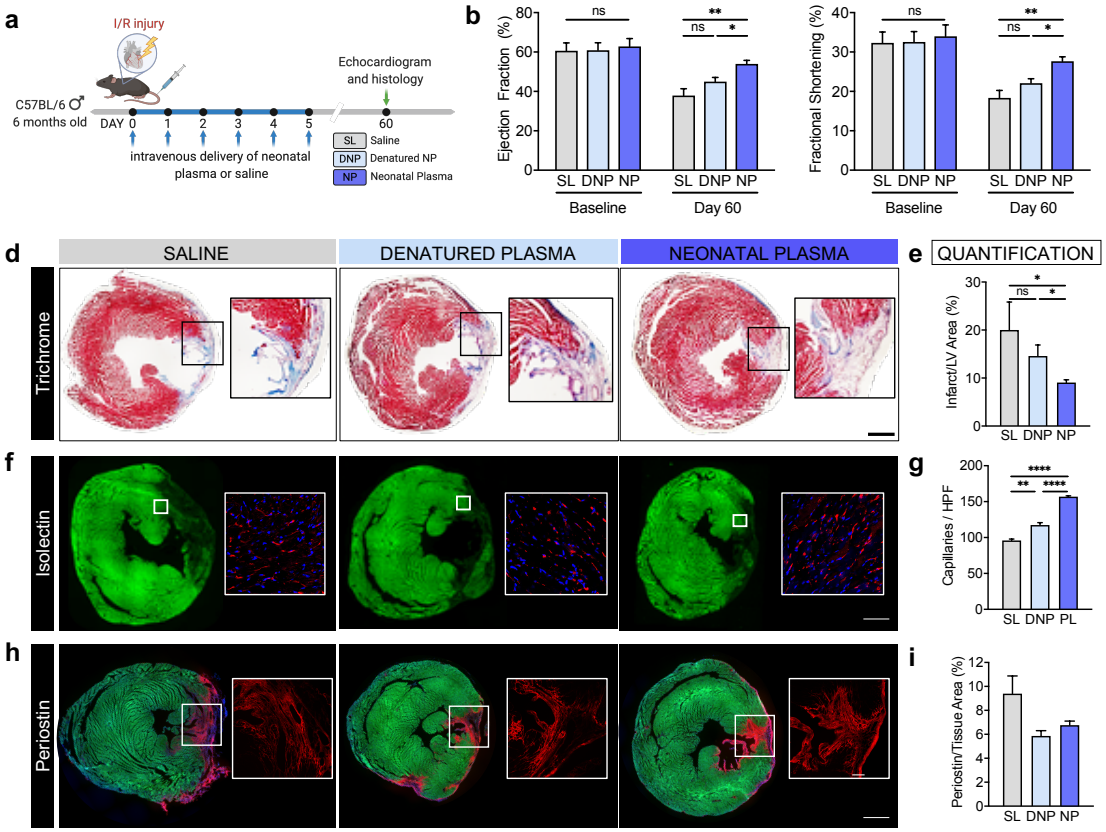

Figure 4.1: Functional and histological analysis of mouse hearts treated with neonatal plasma after I/R injury.
(a) Schematic of experimental timeline. **(b)** Ejection fraction and **(c)** fractional shortening at baseline and 60 days post injury. **(d)** Trichrome staining and **(e)** quantification to assess scar size. **(f)** Isolectin staining and **(g)** quantification to assess vascular density. **(h)** Periostin staining and **(i)** quantification to assess for activated fibroblasts. Scale bars = 1 mm.

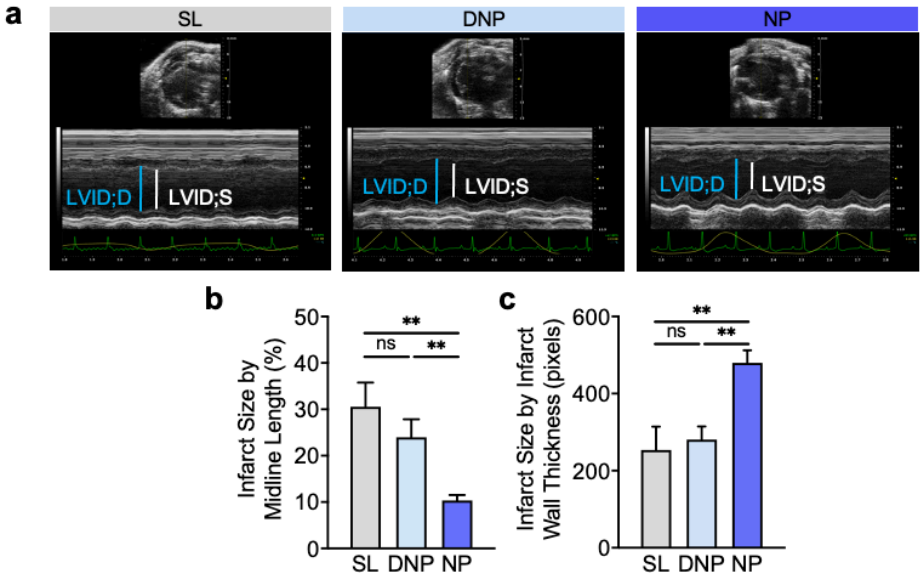

Figure 4.2: Echocardiography and quantification of scar size and heart weight.
(a) Representative M-mode echocardiographic images of hearts 60 days following injury and treatment. Scar size as assessed by **(b)** midline length and **(c)** infarct wall thickness. Heart weights normalized to **(d)** body weight and **(e)** tibia length.

4.4.2. Neonatal plasma ameliorates apoptosis and enhances proliferation of cardiac cells

As systemic factors have been previously shown to mediate a wide variety of effects in different cell types, we examined whether the improvement in cardiac function and scar size can be attributed to specific responses within the major cardiac cell types, namely cardiomyocytes, fibroblasts, and endothelial cells. We first examined whether neonatal plasma affects the extent of hypoxia-induced apoptosis in neonatal rat ventricular myocytes (NRVMs). NRVMs were stressed with cobalt chloride for 3 hours and then switched to normal growth media supplemented with plasma for 24 hours (**Figure 4.3a**). TUNEL staining revealed a significant decrease in the percent of TUNEL+ cells with neonatal plasma treatment compared to controls (**Figure 4.3b,c**). We then examined the effect of neonatal plasma on proliferation and tubal formation capability of human umbilical vein endothelial cells (HUVECs). Quantification of well confluence (as an indirect measure of proliferation) over 28 hours showed that neonatal plasma increased the rate of proliferation compared to FBS controls and interesting, this effect was not observed in denatured

neonatal plasma (**Figure 4.3d** and **Figure 4.4a**). Similarly, neonatal plasma treatment improved various metrics of tubal formation compared to PBS and denatured neonatal plasma in an *in vitro* angiogenesis assay (**Figure 4.3e-i**). We also examined proliferation and apoptosis of endothelial cells and fibroblasts *in vivo*. C57BL/6 adult mice were given 4 doses of neonatal plasma after I/R injury and the extent of BrdU and Annexin V labeling were determined with flow cytometry (**Figure 4.3j**). Within endothelial cells, neonatal plasma treatment significantly increased the percent of BrdU+ cells, with a concomitant decrease in the percent of Annexin V+ labeling (**Figure 4.3k** and **Figure 4.4b**). Fibroblasts, determined as Thy1+ cells, showed similar trends although were not significant compared to controls (**Figure 4.3l** and **Figure 4.4b**).

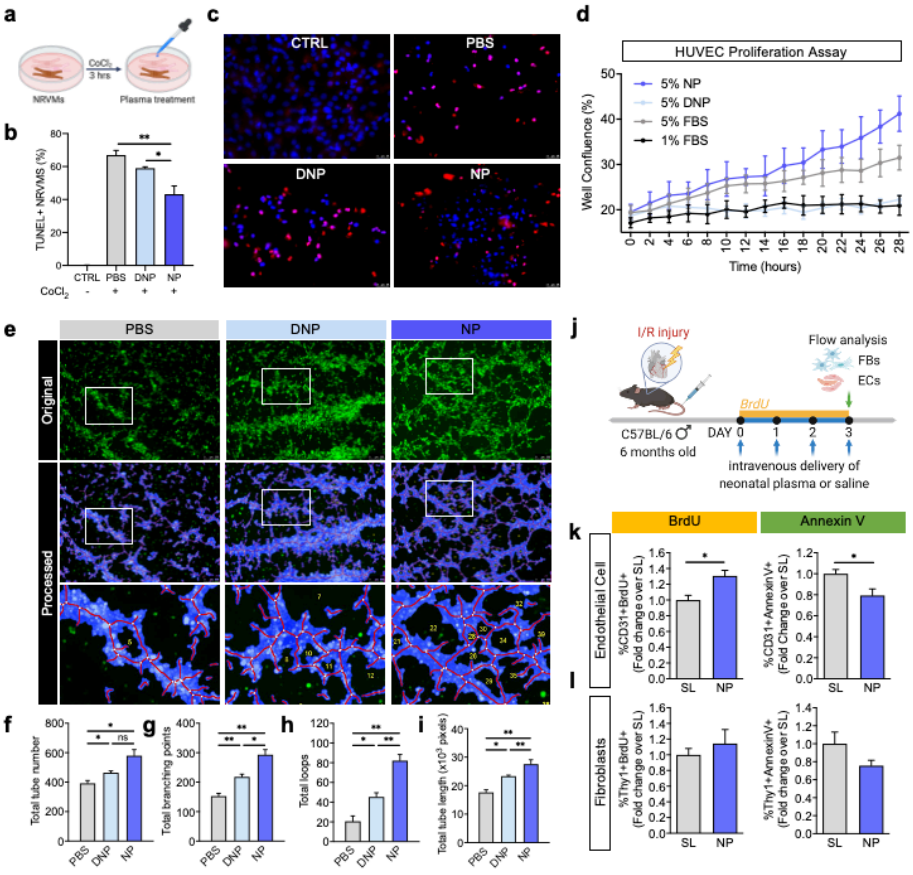

Figure 4.3: Effect of neonatal plasma on the proliferation and apoptosis of cardiac cells. **(a)** Schematic of NRVM exposed to hypoxia followed by neonatal plasma treatment. **(b)** Quantification of the percent of TUNEL+ NRVMs with **(c)** corresponding images. * $p < 0.05$, ** $p < 0.01$. **(d)** Percent well confluence as a measure of cellular proliferation using the Incucyte cell imaging system on HUVECs. **(e)** Tubal formation assay of endothelial cell analyzed for **(f)** total tube number, **(g)** total branching points, **(h)** total loops, and **(i)** total tube length. **(j)** Schematic of BrdU and Annexin V flow experiment of **(k)** endothelial cells and **(l)** fibroblasts.

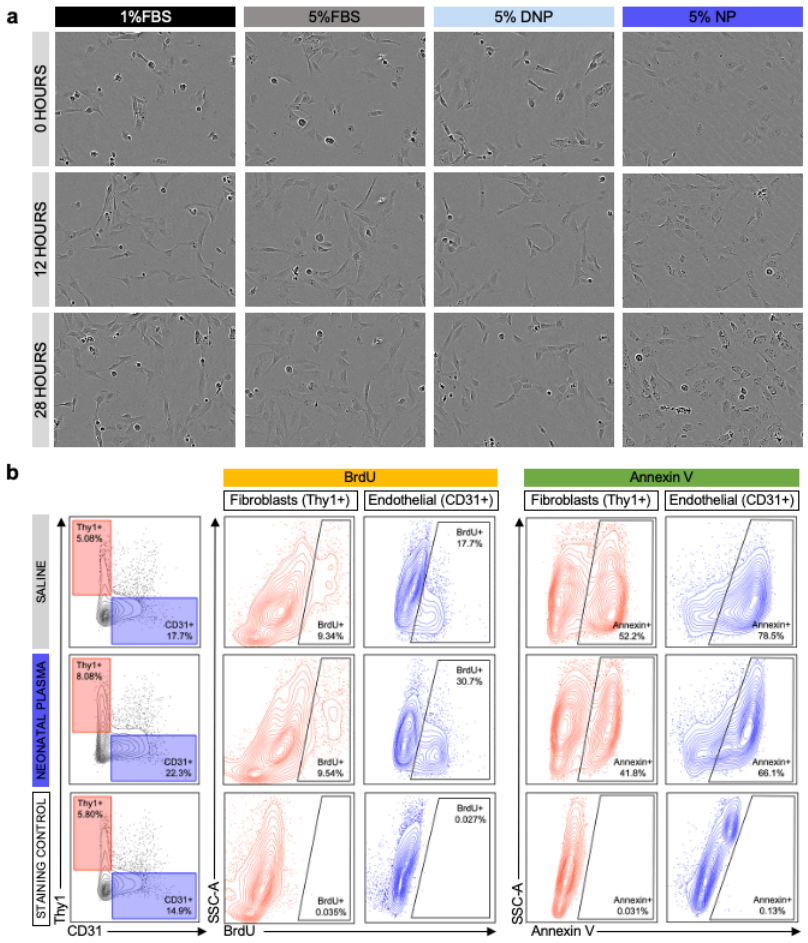

Figure 4.4: Effect of neonatal plasma on the proliferation and apoptosis of endothelial and fibroblasts. **(a)** Incucyte images of endothelial cells treated with reduced serum media (1% FBS, 3% FBS), denatured neonatal plasma, or neonatal plasma at (top) baseline, (middle) 12 hours, and (bottom) 28 hours. **(b)** Analysis of percent BrdU+ and Annexin V+ within fibroblasts and endothelial cells treated with neonatal plasma or saline.

4.4.3. Single cell RNA sequencing highlights an anti-apoptosis role of neonatal plasma

Given both the phenotypic and cellular changes observed in response to neonatal plasma treatment, we next sought to examine its effect at the transcriptomic level. To do so, we turned to single cell RNA sequencing (scRNA seq) as a platform that would allow for profiling of the whole heart at the level of individual cells. Male C57BL/6 mice 6 months of age were subjected to experimental I/R injury followed by intravenous delivery of neonatal plasma or saline control for 4 consecutive days (**Figure 4.5a**). Sham animals served as surgery control. On Day 7 after injury, single cells digested from the left ventricles of hearts within each experimental group were pooled

and captured for RNA sequencing using the 10X Genomics platform. In total, 3,250 (Sham), 5,118 (IR Saline), and 2,754 (IR Plasma) passed quality control processing. UMAP analysis shows a general overlap of cells from different treatment groups (**Figure 4.5b** and **Figure 4.6a**). By plotting expression of established cardiac cell type markers, we were able to identify distinct clusters as endothelial cells (ECs), immune cells (IMs), fibroblasts (FBs), cardiomyocytes (CMs), and combined smooth muscle and pericytes (MCs) (**Figure 4.5c** and **Figure 4.6b**). GO analysis of the top 100 genes within each of the cell clusters confirmed their identity (**Figure 4.6c**).

We first looked at differential gene expression between the different treatment groups to determine whether the transcriptomic profile of hearts treated with neonatal plasma differs from saline control. As expected, the profile of sham control, in which the LAD was not ligated, was distinct from both the saline and neonatal plasma treated groups (**Figure 4.5d-f**) and GO biological process of the top 50 genes enriched in this group revealed pathways associated with normal cardiac function such as “ATP synthesis coupled electron transport” and “cell junction assembly” (**Figure 4.5e**). In both saline and neonatal plasma treated groups, processes such as “cytoplasmic translation” and “ribosome biogenesis” were enriched, likely attributed to the ischemia-reperfusion injury. Interestingly, apoptosis-related pathways were observed in saline treated groups whereas cell chemotaxis and immune-related pathways were enriched in neonatal plasma treated group (**Figure 4.5e-f**).

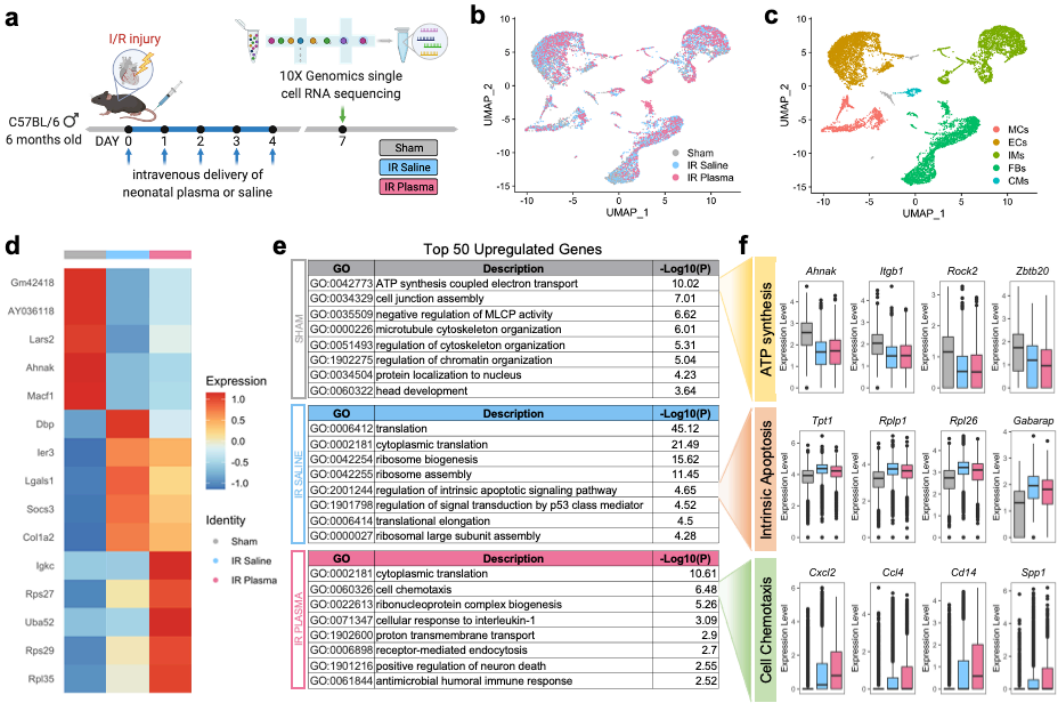

Figure 4.5: Single cell RNA sequencing of mouse hearts treated with neonatal plasma. **(a)** Schematic of experimental plan. **(b)** UMAP of cells captured from single cell RNA sequencing. **(c)** UMAP of identified cardiac subpopulations using known cell type markers. **(d)** Heat map of top 5 genes enriched in each experimental group. **(e)** GO Biological Processes of the top 50 genes enriched in each experimental group with **(f)** corresponding boxplots of selected pathways.

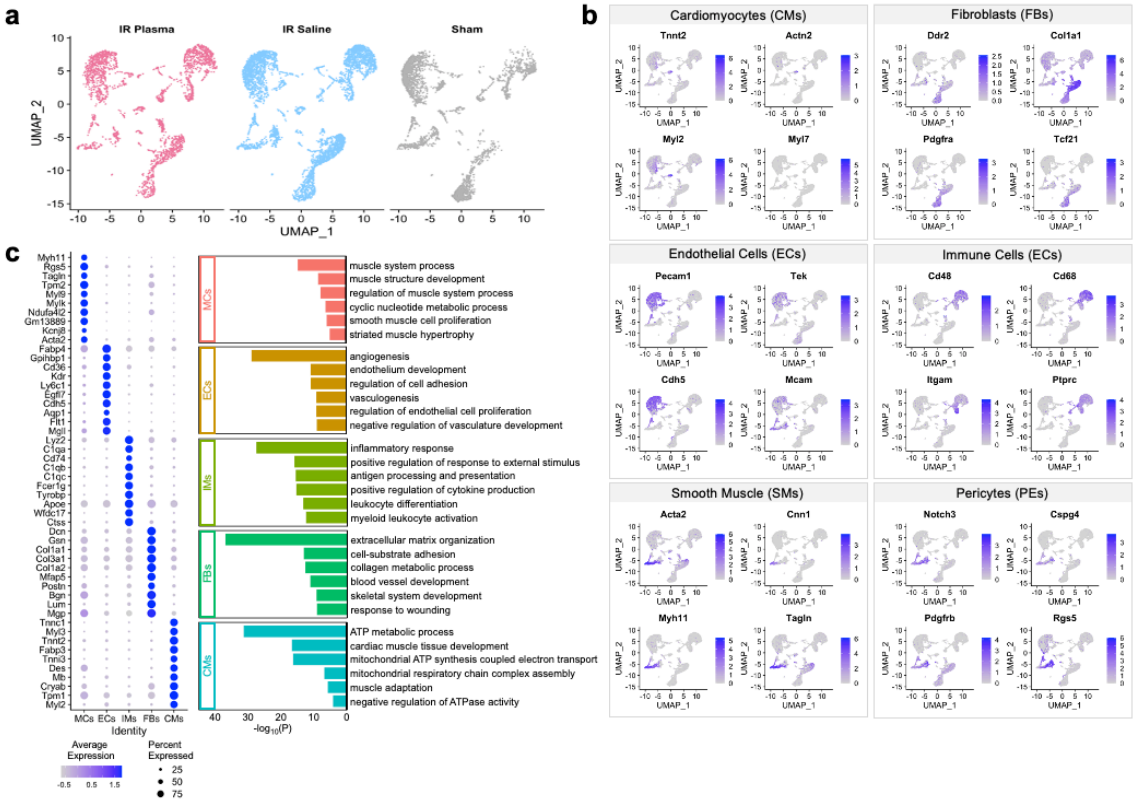

Figure 4.6: Identification and verification of cardiac subpopulations using established cell type markers.
(a) UMAP of cells isolated from whole heart, split into separate treatment groups. **(b)** FeaturePlot of known cell type markers for identification of cardiac subpopulations. **(c)** Verification of selected cardiac subpopulations using dotplot (left) of top genes within each cluster and corresponding GO Biological Process of the top 100 genes within each subpopulation (right).

To examine cell-type specific responses to neonatal plasma administration, CMs were subsetted for further analysis (**Figure 4.7a-c**). UMAP dimension reduction shows a visually distinct cluster of CMs composed predominantly of cells from the saline group (**Figure 4.7b**). Differential gene expression and pathway analysis revealed that CMs from the saline group expressed more genes associated with translation and apoptosis pathways whereas neonatal plasma promoted more immune-related pathways (**Figure 4.7d**). As the location of cells relative to the infarct region may result in differences in severity of ischemic injury (i.e., cells closer to the ligated region may experience more severe ischemia compared to remote regions), it is possible that these CM clusters identified may be separated by extent of injury, in which we can expect

CMs with less severe ischemia to cluster with cells from the sham control. To investigate this, we performed clustering analysis of CMs which showed three distinct clusters of cells, of which Cluster 1 is predominantly composed of CMs from saline group and Cluster 2 from neonatal plasma group (**Figure 4.7e,f**). Differential gene expression and pathway analysis shows an enrichment of Cluster 0 in pathways such as ATP metabolic process and cellular respiration, suggestive of normal CM function (**Figure 4.7g-i**). Cluster 1, containing the majority of CMs from the saline group, exhibited pathways relating to translation and ribosome biogenesis whereas Cluster 2, containing a majority of plasma treated CMs, were enriched in ATP synthesis coupled electron transport and muscle cell differentiation, suggestive of their shift toward normal CM function (Cluster 0), which is also visually observed on UMAP (**Figure 4.7e**). Of note, we identified several genes (*Crct1*, *Sprr1a*, *Serpinb1a*, *Lgals3*) whose expression was mostly specific to only Cluster 1 (**Figure 4.7h**). Together, our scRNA seq profiling shows distinct gene expression changes with neonatal plasma administration, indicating their effect at the transcriptomic level.

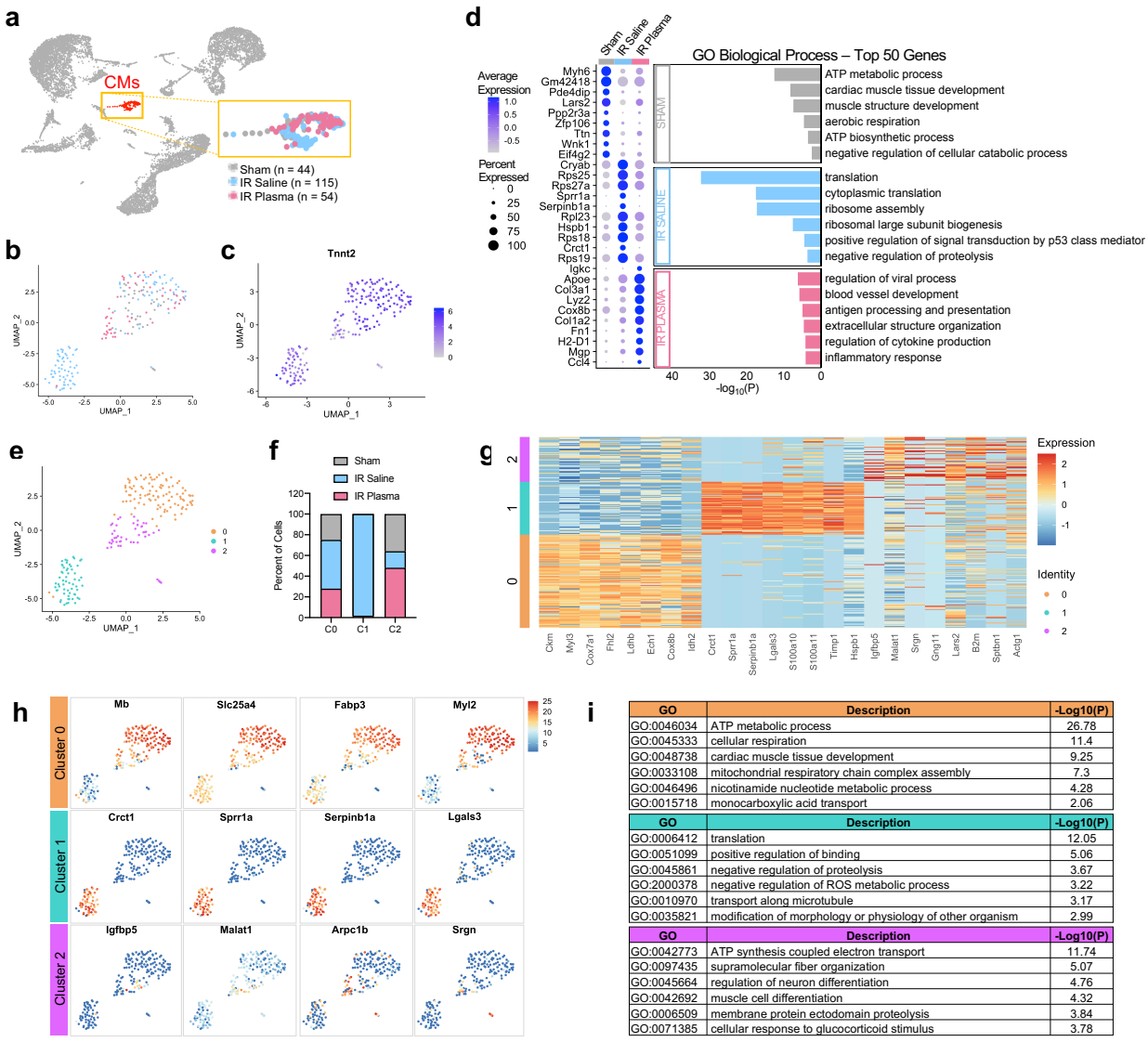

i

GO	Description	-Log10(P)
GO:0046034	ATP metabolic process	26.78
GO:0045333	cellular respiration	11.4
GO:0048738	cardiac muscle tissue development	9.25
GO:0033108	mitochondrial respiratory chain complex assembly	7.3
GO:0046496	nicotinamide nucleotide metabolic process	4.28
GO:0015718	monocarboxylic acid transport	2.06

GO	Description	-Log10(P)
GO:0006412	translation	12.05
GO:0051099	positive regulation of binding	5.06
GO:0045861	negative regulation of proteolysis	3.67
GO:2000378	negative regulation of ROS metabolic process	3.22
GO:0010970	transport along microtubule	3.17
GO:0035821	modification of morphology or physiology of other organism	2.99

GO	Description	-Log10(P)
GO:0042773	ATP synthesis coupled electron transport	11.74
GO:0097435	supramolecular fiber organization	5.07
GO:0045664	regulation of neuron differentiation	4.76
GO:0042692	muscle cell differentiation	4.32
GO:0006509	membrane protein ectodomain proteolysis	3.84
GO:0071385	cellular response to glucocorticoid stimulus	3.78

Figure 4.7: Single cell RNA sequencing analysis of cardiomyocyte subpopulations. **(a)** UMAP of cells isolated from left ventricle with inset depicting cardiomyocyte subpopulation. **(b)** UMAP of cardiomyocyte subpopulation labeled by treatment group. **(c)** FeaturePlot of Tnnt2 expression. **(d)** Dotplot (left) of top 10 genes and corresponding GO Biological Process of the top 50 genes enriched in each treatment group. **(e)** UMAP of cardiomyocyte subpopulation labeled by clusters. **(f)** Quantification of the proportion of cells from each treatment group within each cluster. **(g)** Heatmap of the top 8 genes from each cardiomyocyte cluster identified with the **(h)** top 4 genes displayed as FeaturePlot. **(i)** GO Biological process of the top 100 genes from each cluster.

4.4.4. Mass spectrometry reveals differences in associated pathways and molecular functions of differentially abundant proteins between neonatal and adult mouse plasma

To identify candidates that may mediate both the functional and transcriptomic changes observed, we performed quantitative mass spectrometry on plasma from neonatal and aged mice

using the isobaric tag for relative and absolute quantitation (iTRAQ) methodology (**Figure 4.8a** and **Figure 4.9a**). In brief, proteins were extracted from plasma samples and high abundance proteins were depleted (immunoglobulins and albumin). Samples were then digested, labeled with iTRAQ reagents, and fractionated for mass spectrometry. Database analysis revealed a total of 872 proteins, of which 310 and 85 were determined to be of increased (>2.0) and decreased (<0.5) abundance, respectively, within neonatal plasma compared to aged plasma (**Figure 4.8b-e** and **Table 4.1**). Biological pathway analysis of all decreased abundance proteins shows enrichment of immune-related processes whereas increased abundance proteins show a mixture of metabolic and ribonucleoprotein biogenesis (**Figure 4.8f,g**). Protein mass and peptide length histograms demonstrate low molecular weights and lengths of identified proteins, with "binding" as the key molecular function (**Figure 4.9b-e**).

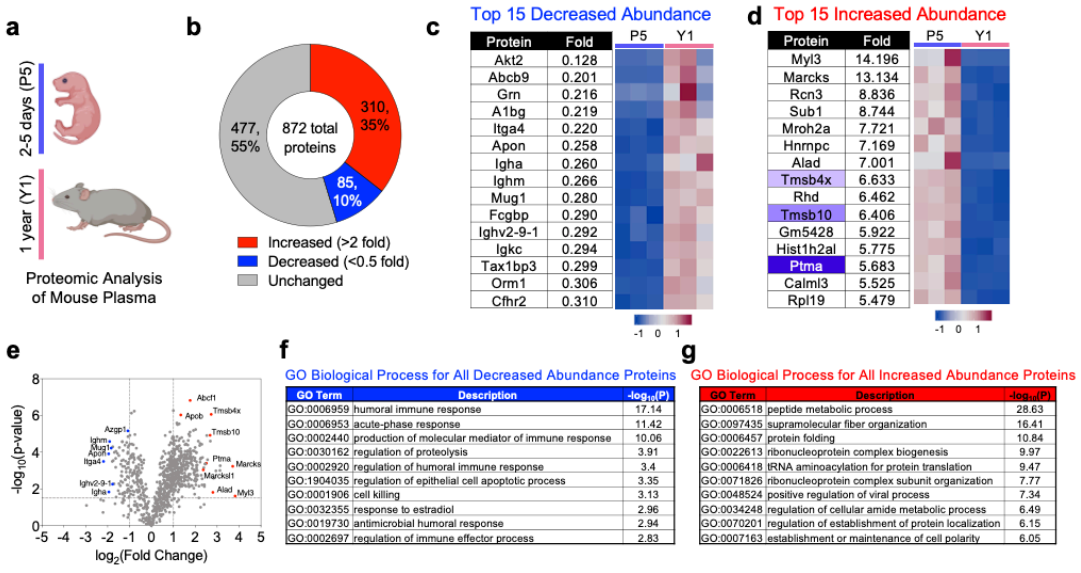

Figure 4.8: Mass spectrometry of neonatal and aged plasma.
(a) Plasma of neonatal mice 2-5 days and adult mice 1 year of age were obtained for mass spectrometry. **(b)** 872 proteins were identified, of which 310 were increased (> 2-fold) and 85 were decreased (< 0.5-fold) in abundance in neonatal compared to adult plasma. List and corresponding heatmaps of the top 15 **(c)** decreased and **(d)** increased abundance proteins found in neonatal plasma compared to adult plasma. Thymosin proteins Tmsb4x, Tmsb10, and Ptma are highlighted. **(e)** Volcano plot of proteins identified. GO Biological Process of **(f)** decreased and **(g)** increased abundance proteins.

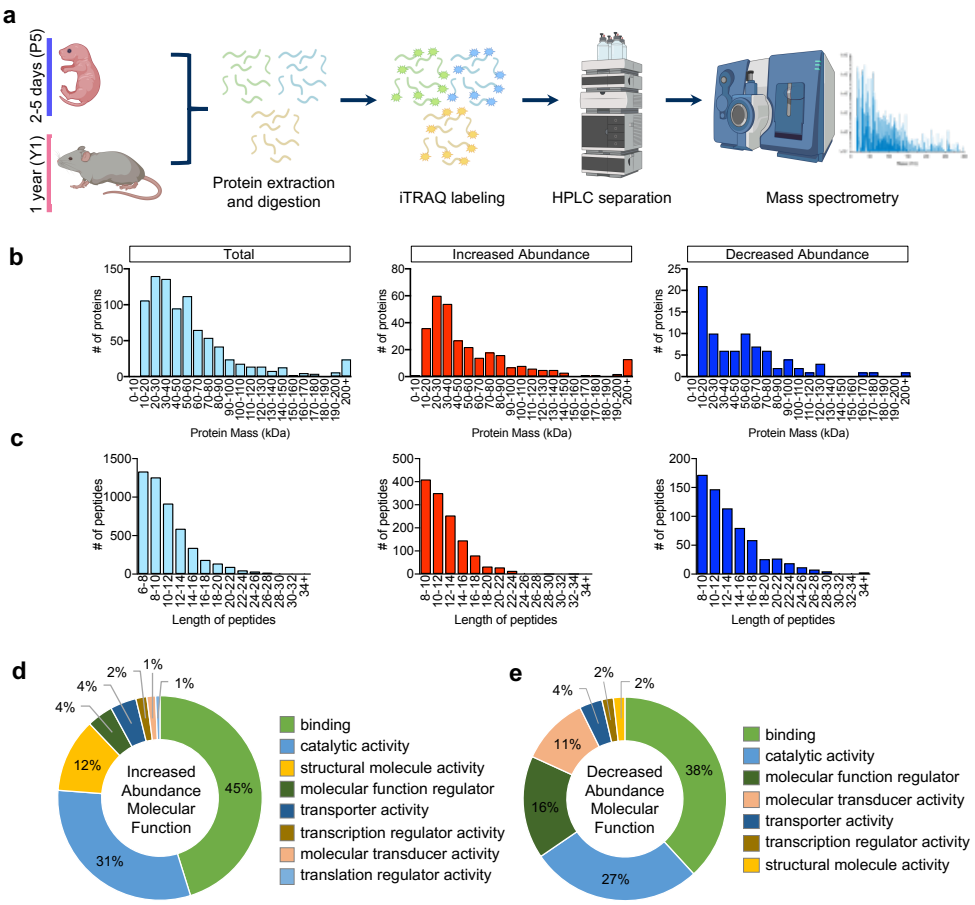

Figure 4.9: Categorization of proteins identified from mass spectrometry.
(a) Schematic of mass spectrometry process. **(b)** Protein mass and **(c)** peptide length distribution of total, increased, and decreased abundance proteins. **(d-e)** Component analysis of plasma samples to show variability across biological samples. Categorization of molecular function of **(f)** increased and **(g)** decreased abundance proteins.

Table 4.1: Normalized intensity values of the top 15 increased and decreased abundance proteins between neonatal plasma and aged plasma.

	PROTEIN ID	GENE ID	P5_1	P5_2	P5_3	AVG P5	Y1_1	Y1_2	Y1_3	AVG Y1	P5/Y1	P-VALUE
INCREASED ABUNDANCE	A0A0G2JDW2	Myl3	0.0006183	0.0005952	0.0012613	0.0008249	0.0000617	0.0000571	0.0000555	0.0000581	14.1960765	0.0246034
	P26645	Marcks	0.0000811	0.0000589	0.0000762	0.0000721	0.0000056	0.0000044	0.0000065	0.0000055	13.1344740	0.0005910
	A0A1B0GS22	Rcn3	0.0000507	0.0000465	0.0000615	0.0000529	0.0000085	0.0000056	0.0000039	0.0000060	8.8359347	0.0005417
	P11031	Sub1	0.0000692	0.0000508	0.0000713	0.0000638	0.0000074	0.0000084	0.0000061	0.0000073	8.7435780	0.0009927
	F5H8M8	Mroh2a	0.0007490	0.0009972	0.0007409	0.0008290	0.0000960	0.0001248	0.0001013	0.0001074	7.7206838	0.0010366
	Q9Z204-4	Hnrnpc	0.0003733	0.0002364	0.0003172	0.0003090	0.0000445	0.0000457	0.0000391	0.0000431	7.1687040	0.0026021
	P10518	Alad	0.0000362	0.0000337	0.0000629	0.0000442	0.0000059	0.0000059	0.0000072	0.0000063	7.0006149	0.0153986
	P20065-2	Tmsb4x	0.0002126	0.0002060	0.0002068	0.0002085	0.0000348	0.0000335	0.0000260	0.0000314	6.6330657	0.0000009
	A0A0R4J0A2	Rhd	0.0002332	0.0002060	0.0002208	0.0002200	0.0000395	0.0000334	0.0000292	0.0000340	6.4618613	0.0000248
	Q6ZWY8	Tmsb10	0.0008286	0.0007589	0.0007529	0.0007801	0.0001263	0.0001272	0.0001119	0.0001218	6.4059489	0.0000119
	E9PUX4	Gm5428	0.0006513	0.0005379	0.0006745	0.0006213	0.0001024	0.0001011	0.0001112	0.0001049	5.9222976	0.0002589
	F8WIX8	Hist1h2al	0.0004361	0.0004178	0.0004060	0.0004200	0.0000663	0.0000599	0.0000920	0.0000727	5.7749637	0.0000123
	P26350	Ptma	0.0009620	0.0007784	0.0010014	0.0009139	0.0001508	0.0001599	0.0001717	0.0001608	5.6831727	0.0003996
	Q9D6P8	Calml3	0.0005811	0.0005130	0.0006685	0.0005875	0.0001032	0.0001080	0.0001078	0.0001063	5.5254179	0.0004339
	A2A547	Rpl19	0.0003701	0.0002852	0.0003196	0.0003250	0.0000675	0.0000545	0.0000559	0.0000593	5.4789257	0.0004432
DECREASED ABUNDANCE	Q61405	Cfhr2	0.0000798	0.0000815	0.0000811	0.0000808	0.0002740	0.0002701	0.0002374	0.0002605	0.3101455	0.0001017
	Q60590	Orm1	0.0004247	0.0003866	0.0003809	0.0003974	0.0014947	0.0014296	0.0009763	0.0013002	0.3056637	0.0052695
	B1AUD9	Tax1bp3	0.0000943	0.0000898	0.0000829	0.0000890	0.0002922	0.0003297	0.0002708	0.0002976	0.2990527	0.0002866
	A0A075B5P2	Igkc	0.0010492	0.0010107	0.0011027	0.0010542	0.0036847	0.0037443	0.0033153	0.0035814	0.2943511	0.0000505
	A0A075B697	Ighv2-9-1	0.0000203	0.0000263	0.0000211	0.0000226	0.0000859	0.0000884	0.0000575	0.0000773	0.2922253	0.0055716
	E9Q9C6	Fcgbp	0.0000279	0.0000335	0.0000201	0.0000272	0.0000946	0.0001003	0.0000857	0.0000936	0.2902920	0.0003203
	P28665	Mug1	0.0046498	0.0044863	0.0045922	0.0045761	0.0163233	0.0152164	0.0175122	0.0163506	0.2798710	0.0000596
	P01872	Ighm	0.0034062	0.0031806	0.0034189	0.0033353	0.0132893	0.0124457	0.0118646	0.0125332	0.2661137	0.0000259
	A0A075B6A3	Igha	0.0006095	0.0005702	0.0006133	0.0005977	0.0020648	0.0017245	0.0030992	0.0022962	0.2602916	0.0147717
	G3X9D6	Apon	0.0000493	0.0000516	0.0000454	0.0000488	0.0002066	0.0001752	0.0001843	0.0001887	0.2584166	0.0001231
	Q792F9	Itga4	0.0000351	0.0000349	0.0000251	0.0000317	0.0001502	0.0001567	0.0001266	0.0001445	0.2195470	0.0003169
	Q19LI2	A1bg	0.0032040	0.0028633	0.0031682	0.0030785	0.0169122	0.0187334	0.0065847	0.0140768	0.2186940	0.0438410
	Q3U9N4	Grn	0.0000147	0.0000166	0.0000131	0.0000148	0.0000524	0.0001345	0.0000187	0.0000685	0.2162388	0.1934422
	D6RFD9	Abcb9	0.0000097	0.0000090	0.0000086	0.0000091	0.0000509	0.0000624	0.0000223	0.0000452	0.2014306	0.0387850
	F8WHG5	Akt2	0.0000197	0.0000187	0.0000232	0.0000206	0.0002135	0.0002275	0.0000405	0.0001605	0.1281098	0.0805425

4.4.5. Thymosin proteins are enriched in neonatal plasma

Of the top candidates identified from mass spectrometry, three increased abundance proteins were from the thymosin family: Tmsb4x (Thymosin beta 4), Tmsb10 (Thymosin beta 10), and Ptma (Prothymosin alpha) (highlighted in **Figure 4.8d**). Tmsb4x and Tmsb10 are associated with GO terms relating to actin binding and organization whereas Ptma has been shown to be involved in apoptosis and histone binding/exchange (**Figure 4.10a**). Both Tmsb4x and Tmsb10 were previously identified to be of increased abundance in young compared to aged plasma[144] (**Figure 4.10b**). To further assess the potential of these candidates as age-dependent factors that may be mediating the beneficial effects observed, we used the Kaessmann database[145], containing RNA sequencing results of various organs in 7 different species spanning across developmental age. Interestingly, we observed an overall decline with age in the expression of these three candidate genes across different organs, with the most consistent trend being Ptma expression (**Figure 4.10c**).

a

	Qualifier	GO Term	Reference	Assigned By
Tmsb4x	enables	GO:0003785: actin monomer binding	GO_REF:0000002	InterPro
	involved_in	GO:0007015: actin filament organization	GO_REF:0000002	InterPro
	part_of	GO:0005856: cytoskeleton	GO_REF:0000044	UniProt
Tmsb10	part_of	GO:0005856: cytoskeleton	GO_REF:0000044	UniProt
	enables	GO:0003785: actin monomer binding	GO_REF:0000002	InterPro
	involved_in	GO:0007015: actin filament organization	GO_REF:0000002	InterPro
Ptma	involved_in	GO:0043066: negative regulation of apoptotic process	GO_REF:0000024	UniProt
	part_of	GO:0005634: nucleus	GO_REF:0000043	UniProt
	enables	GO:0042393: histone binding	PMID:20434447	MGI
	acts_upstream_of_or_within	GO:0043486: histone exchange	PMID:20434447	MGI
	acts_upstream_of_or_within	GO:0043486: histone exchange	PMID:20434447	MGI
	part_of	GO:0005634: nucleus	GO_REF:0000044	UniProt

b

MASS SPECTROMETRY COUNT													
PMID: 32396872	Y1	Y2	Y3	Y4	Y5	Y6	O1	O2	O3	O4	O5	O6	Ratio (Y/O)
Tmsb4x	6	6	16	6	13	11	11	6	6	3	10	4	1.45
Tmsb10	6	3	13	1	2	1	5	3	3	0	2	0	2.00
Ptma	0	0	0	0	0	0	0	0	0	0	1	0	0.00
Grn	24	20	20	16	14	13	12	5	14	9	12	14	1.62
A1bg	204	144	312	0	0	0	526	822	1074	0	0	0	0.27
Itga4	2	2	1	0	0	0	0	0	0	0	0	0	--
Igha	3	1	2	1	5	4	13	1	4	4	7	10	0.41
Ighm	66	115	73	45	94	42	189	225	894	415	638	254	0.17
Mug1	750	921	1116	1114	1985	1375	326	331	306	1019	1719	1047	1.53
Igkc	6	8	5	2	4	2	23	14	44	24	40	20	0.16
Orm1	71	101	148	99	104	64	364	70	118	68	99	88	0.73
Y = young mouse plasma (2 months old), O = old mouse plasma (21-23 months)													

c

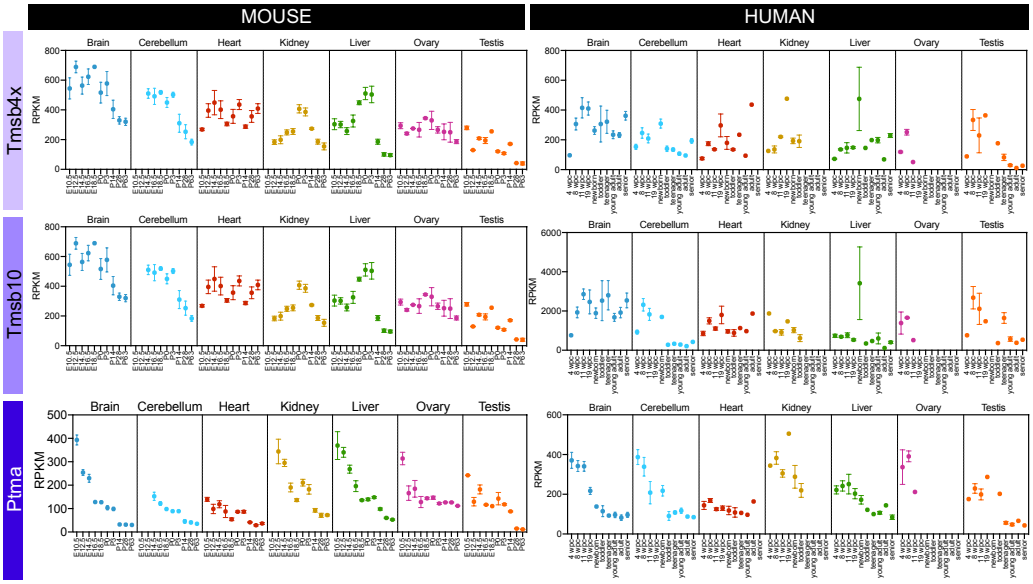

Figure 4.10: Database search and comparison of mass spectrometry results.
(a) GO term classification of thymosin protein candidates. **(b)** Comparison of mass spectrometry results with Yang et al study. **(c)** Gene expression trends across different organs and developmental age of candidates using the Kaessmann database.

4.4.6. Thymosin proteins protect cardiomyocytes from ischemia-induced apoptosis

The cross-examination of the identified candidates with online databases and previously published studies likely demonstrates the age-dependence of these three thymosin proteins. To examine potential functional roles of these candidates, particularly on cellular apoptosis, we next used an *in vitro* hypoxia assay of HL-1 CMs, in which cells were exposed to low oxygen (1%O_2)

for 6 hours prior to treatment with recombinant forms of these proteins. Quantification of the number of DAPI+ cells per field showed that treatment with either thymosin β4 or prothymosin α reduced the number of DAPI+ HL-1 CMs (**Figure 4.11a,c** and Error! Reference source not found.**a**). This effect is not consistently observed with thymosin β10 although a dose-dependent effect was present (**Figure 4.11b,e**). While thymosin β4 displayed a protective effect, we observe a small therapeutic window, as high doses (500 nM) resulted in cellular toxicity (**Figure 4.11d**). This is in contrast to prothymosin α, in which high concentrations did not have a negative effect on cellular viability (**Figure 4.11f**). Quantification of both EdU incorporation and pHH3 immunoreactivity showed no effect of these three candidates on cellular proliferation (data not shown).

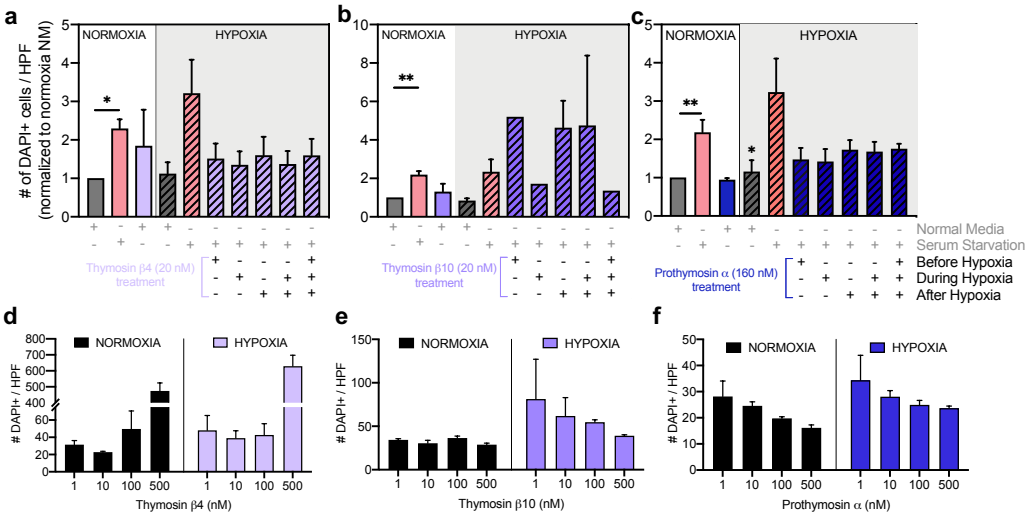

Figure 4.11: *In vitro* assessment of hypoxia-induced apoptosis and treatment with protein candidates in HL-1 cardiomyocytes.
Live/dead analysis of HL-1 cardiomyocytes treated with **(a)** thymosin β4, **(b)** thymosin β10, and **(c)** prothymosin α under normoxic and hypoxic conditions. Effect on cell viability of HL-1 cardiomyocytes to varying dose of **(d)** thymosin β4, **(e)** thymosin β10, and **(f)** prothymosin α.

4.5. DISCUSSION

The search of "pro-youthful" factors to delay the aging process has been an elusive quest. Researchers have turned to parabiosis as a way to examine effects of shared circulation and to identify potential factors as a regenerative therapy. In this study, we aim to understand the role of

systemic factors in the context of cardiac ischemia-reperfusion injury. Given the known ability of the neonatal heart to fully regenerate after injury, we hypothesized that neonatal circulation may be more enriched with factors that promote repair and regeneration. Our *in vivo* study showing improved cardiac function and reduced scar sizes in hearts of mice after ischemia reperfusion injury implicates a protective effect of neonatal plasma. At a cellular level, we find that neonatal plasma ameliorates apoptosis of cardiomyocytes and promotes tubal formation of endothelial cells, both of which are key processes involved in cardiac regeneration. A decrease in the degree of cardiomyocyte apoptosis may shift cells toward autophagy during the early and critical phases of remodeling to minimize cellular loss and maintain cardiac contractile function[146].

Our finding of diminished biological effects via the denaturing process recapitulates the significance of proteins from prior studies[77, 138] and led us to examine the proteomic profile of neonatal and aged mouse plasma. The generated dataset provides a unique look into the proteome during a period of development that is much earlier than prior studies. Of the candidates identified, we were particularly interested in prothymosin α, thymosin β4, and thymosin β10, given their name association with the thymus, an organ whose size and function changes with developmental age[147], as well as the known roles of thymosin β4 in cardiac repair[148-150]. The thymus plays a key role in the development of T cells during fetal and early development and is, therefore, vital for proper function of the adaptive immune response. However, their function is dispensable after puberty leading to involution of the organ[151]. The increased abundance of these thymosin proteins within neonatal plasma reflects the known function and development of this immune organ. Our *in vitro* finding of a protective role of both prothymosin alpha and thymosin β4 in cardiomyocyte apoptosis suggests of their therapeutic potential. It has been previously shown that the anti-apoptotic function of Ptma may be regulated via the Akt signaling pathway[152], which itself is associated with a multitude of cellular processes such as cellular proliferation and growth[153]. Interestingly, our initial analysis of the transcriptomic profile of cardiomyocytes shows

an enrichment of apoptosis-associated pathways in saline control whereas neonatal plasma administration shifts the biological processes toward more immune-related terms.

While we have primarily focused on the existence of “pro-youthful” factors within neonatal plasma, it is worthy to note an alternative therapeutic strategy, one that is focused on the identification and inhibition of “pro-aging” factors that may play a role in the injury response. Our proteomic profile highlights a decrease in immune-related factors within neonatal compared to aged plasma, which is in alignment with the increased presence of thymic proteins. Further studies are warranted to dive deeper into this aspect of cardiac repair. Furthermore, while we observe a protective role of both prothymosin α and thymosin $\beta 4$, it may be likely that their combined treatment may offer greater protection from cardiomyocyte apoptosis. In summary, our study highlights a protective effect of neonatal plasma and the potential role of thymosin proteins in mediating cardiac repair. It brings to light the potential of neonatal plasma as a rejuvenative therapy for cardiovascular as well as other age-related diseases.

CHAPTER 5: CONCLUSIONS AND FUTURE DIRECTIONS

5.1. LIST OF SIGNIFICANT FINDINGS

5.1.1. Chapter 2: Analysis of cardiomyocyte clonal expansion during mouse heart development and injury

- The Rainbow mouse model provides a direct tool for clonal expansion analyses.
- BrdU studies uncover decreasing proliferative capacity of cardiomyocytes over time.
- Epicardial progenitors are unlikely to be sources of cardiomyocytes.
- Single cell RNA sequencing delineates heterogeneity of cardiomyocytes at early stages of development.
- Injury activates proliferation in neonatal but not adult cardiomyocytes.

5.1.2. Chapter 3: Harnessing the versatility of PLGA nanoparticles for targeted Cre-mediated recombination

- Loading of tamoxifen within PLGA nanoparticles enables high-resolution detection of uptake and drug delivery in an inducible CreER mouse model.
- Antibody surface-conjugation enhances targeted delivery of nanoparticles.
- Targeted PLGA antibodies offer a time- and cost-effective strategy for clonal expansion analysis studies

5.1.3. Chapter 4: Protective effects of neonatal plasma on cardiac ischemia-reperfusion injury

- Neonatal plasma improves cardiac function, reduces scar size, and increases vascular density of mouse hearts after I/R injury.
- Neonatal plasma ameliorates apoptosis and enhances proliferation of cardiac cells.
- Single cell RNA sequencing highlights an anti-apoptosis role of neonatal plasma.

- Mass spectrometry reveals differences in associated pathways and molecular functions of differentially abundant proteins between neonatal and adult mouse plasma.
- Thymosin proteins are enriched in neonatal plasma.
- Thymosin proteins protect cardiomyocytes from ischemia-induced apoptosis

5.2. FUTURE DIRECTION

In this dissertation, we present our work on the development of a multi-colored genetic labeling mouse reporter system to more directly understand the proliferative potential of cardiomyocytes during early development and after injury. Our single cell RNA sequencing results highlight the heterogeneity of early embryonic cardiomyocytes and uncovered genes enriched in embryonic day 9.5 that are associated with the high proliferative phenotype of cells at this developmental stage. Pathway analysis associated these groups of genes with developmental growth and cell division and migration, making them worthy for further investigation as potential genes that contribute to the regenerative potential of these early CMs. We also discuss our approach to develop biodegradable and biocompatible PLGA nanoparticles as a tool for clonal expansion analysis. While we have tested the ability of specific targeting using surface conjugation of nanoparticles with antibodies, it would be interesting to determine whether the addition of multiple targeting antibodies can be achieved and how this modification affects their specific binding of different cell types. Lastly, in our chapter addressing the presence of “pro-youthful” factors in neonatal plasma, we are pursuing *in vivo* studies to examine the functional benefits of recombinant forms of the identified thymosin candidates. We are also performing more in-depth characterization and quantification of these candidates in both mouse and human plasma across different developmental ages to further validate our mass spectrometry results and as well better understand the profile of these factors during the aging process. These are just a few highlights of more exciting research to uncover, all of which resonates around the ultimate goal of developing an effective therapy for ischemic heart disease.

REFERENCES

1. Nabel EG, Braunwald E. A tale of coronary artery disease and myocardial infarction. *N Engl J Med*. Jan 2012;366(1):54-63. doi:10.1056/NEJMra1112570

2. Braunwald E. The war against heart failure: the Lancet lecture. *Lancet*. Feb 2015;385(9970):812-24. doi:10.1016/S0140-6736(14)61889-4

3. Organization WH. Cardiovascular Diseases. https://www.who.int/health-topics/cardiovascular-diseases/#tab=tab_1

4. Reinecke H, Minami E, Zhu WZ, Laflamme MA. Cardiogenic differentiation and transdifferentiation of progenitor cells. *Circ Res*. Nov 2008;103(10):1058-71. doi:10.1161/CIRCRESAHA.108.180588

5. Milavetz JJ, Giebel DW, Christian TF, Schwartz RS, Holmes DR, Gibbons RJ. Time to therapy and salvage in myocardial infarction. *J Am Coll Cardiol*. May 1998;31(6):1246-51. doi:10.1016/s0735-1097(98)00088-6

6. Ali MR, Salim Hossain M, Islam MA, et al. Aspect of thrombolytic therapy: a review. *ScientificWorldJournal*. 2014;2014:586510. doi:10.1155/2014/586510

7. Andersen HR, Nielsen TT, Rasmussen K, et al. A comparison of coronary angioplasty with fibrinolytic therapy in acute myocardial infarction. *N Engl J Med*. Aug 2003;349(8):733-42. doi:10.1056/NEJMoa025142

8. Zhang XL, Zhu QQ, Yang JJ, et al. Percutaneous intervention versus coronary artery bypass graft surgery in left main coronary artery stenosis: a systematic review and meta-analysis. *BMC Med*. Apr 21 2017;15(1):84. doi:10.1186/s12916-017-0853-1

9. Hillis LD, Smith PK, Anderson JL, et al. 2011 ACCF/AHA guideline for coronary artery bypass graft surgery: executive summary: a report of the American College of Cardiology Foundation/American Heart Association Task Force on Practice Guidelines. *J Thorac Cardiovasc Surg*. Jan 2012;143(1):4-34. doi:10.1016/j.jtcvs.2011.10.015

10. Velagaleti RS, Pencina MJ, Murabito JM, et al. Long-term trends in the incidence of heart failure after myocardial infarction. *Circulation*. Nov 2008;118(20):2057-62. doi:10.1161/CIRCULATIONAHA.108.784215

11. Ezekowitz JA, Kaul P, Bakal JA, Armstrong PW, Welsh RC, McAlister FA. Declining in-hospital mortality and increasing heart failure incidence in elderly patients with first myocardial infarction. *J Am Coll Cardiol*. Jan 2009;53(1):13-20. doi:10.1016/j.jacc.2008.08.067

12. Orlic D, Kajstura J, Chimenti S, et al. Bone marrow cells regenerate infarcted myocardium. *Nature*. Apr 5 2001;410(6829):701-5. doi:10.1038/35070587

13. Quaini F, Urbanek K, Beltrami AP, et al. Chimerism of the transplanted heart. *N Engl J Med*. Jan 3 2002;346(1):5-15. doi:10.1056/NEJMoa012081

14. Janssens S, Dubois C, Bogaert J, et al. Autologous bone marrow-derived stem-cell transfer in patients with ST-segment elevation myocardial infarction: double-blind, randomised controlled trial. *Lancet*. Jan 14 2006;367(9505):113-21. doi:10.1016/S0140-6736(05)67861-0

15. Wollert KC, Meyer GP, Lotz J, et al. Intracoronary autologous bone-marrow cell transfer after myocardial infarction: the BOOST randomised controlled clinical trial. *Lancet*. Jul 10-16 2004;364(9429):141-8. doi:10.1016/S0140-6736(04)16626-9

16. Strauer BE, Brehm M, Zeus T, et al. Repair of infarcted myocardium by autologous intracoronary mononuclear bone marrow cell transplantation in humans. *Circulation*. Oct 8 2002;106(15):1913-8. doi:10.1161/01.cir.0000034046.87607.1c

17. Assmus B, Honold J, Schachinger V, et al. Transcoronary transplantation of progenitor cells after myocardial infarction. *N Engl J Med*. Sep 21 2006;355(12):1222-32. doi:10.1056/NEJMoa051779

18. Murry CE, Soonpaa MH, Reinecke H, et al. Haematopoietic stem cells do not transdifferentiate into cardiac myocytes in myocardial infarcts. *Nature*. Apr 8 2004;428(6983):664-8. doi:10.1038/nature02446

19. Balsam LB, Wagers AJ, Christensen JL, Kofidis T, Weissman IL, Robbins RC. Haematopoietic stem cells adopt mature haematopoietic fates in ischaemic myocardium. *Nature*. Apr 8 2004;428(6983):668-73. doi:10.1038/nature02460

20. van Berlo JH, Molkentin JD. An emerging consensus on cardiac regeneration. *Nat Med*. Dec 2014;20(12):1386-93. doi:10.1038/nm.3764

21. van Berlo JH, Kanisicak O, Maillet M, et al. c-kit+ cells minimally contribute cardiomyocytes to the heart. *Nature*. May 15 2014;509(7500):337-41. doi:10.1038/nature13309

22. Eschenhagen T, Bolli R, Braun T, et al. Cardiomyocyte Regeneration: A Consensus Statement. *Circulation*. 07/06
06/16/nihms-submitted
08/15/pmc-release 2017;136(7):680-686. doi:10.1161/CIRCULATIONAHA.117.029343

23. Adelman ER, Huang HT, Roisman A, et al. Aging Human Hematopoietic Stem Cells Manifest Profound Epigenetic Reprogramming of Enhancers That May Predispose to Leukemia. *Cancer Discov*. Aug 2019;9(8):1080-1101. doi:10.1158/2159-8290.CD-18-1474

24. Burridge PW, Keller G, Gold JD, Wu JC. Production of De Novo Cardiomyocytes: Human Pluripotent Stem Cell Differentiation and Direct Reprogramming. *Cell Stem Cell*. 2012;10(1):16-28. doi:10.1016/j.stem.2011.12.013

25. Caspi O, Huber I, Kehat I, et al. Transplantation of human embryonic stem cell-derived cardiomyocytes improves myocardial performance in infarcted rat hearts. *J Am Coll Cardiol*. Nov 2007;50(19):1884-93. doi:10.1016/j.jacc.2007.07.054

26. Menasche P, Vanneaux V, Hagege A, et al. Human embryonic stem cell-derived cardiac progenitors for severe heart failure treatment: first clinical case report. *Eur Heart J*. Aug 7 2015;36(30):2011-7. doi:10.1093/eurheartj/ehv189

27. Skelton Rhys J, Brady B, Khoja S, et al. CD13 and ROR2 Permit Isolation of Highly Enriched Cardiac Mesoderm from Differentiating Human Embryonic Stem Cells. *Stem Cell Reports*. 01/12
06/19/received
11/14/revised
11/18/accepted 2016;6(1):95-108. doi:10.1016/j.stemcr.2015.11.006

28. Fernandes S, Chong JJH, Paige SL, et al. Comparison of Human Embryonic Stem Cell-Derived Cardiomyocytes, Cardiovascular Progenitors, and Bone Marrow Mononuclear Cells for Cardiac Repair. *Stem Cell Reports*. Nov 2015;5(5):753-762. doi:10.1016/j.stemcr.2015.09.011

29. Chong JJ, Yang X, Don CW, et al. Human embryonic-stem-cell-derived cardiomyocytes regenerate non-human primate hearts. *Nature*. Jun 2014;510(7504):273-7. doi:10.1038/nature13233

30. Kadota S, Tanaka Y, Shiba Y. Heart regeneration using pluripotent stem cells. *J Cardiol*. Nov 2020;76(5):459-463. doi:10.1016/j.jjcc.2020.03.013

31. Riegler J, Tiburcy M, Ebert A, et al. Human Engineered Heart Muscles Engraft and Survive Long Term in a Rodent Myocardial Infarction Model. *Circ Res*. Sep 25 2015;117(8):720-30. doi:10.1161/CIRCRESAHA.115.306985

32. Ardehali R, Ali SR, Inlay MA, et al. Prospective isolation of human embryonic stem cell-derived cardiovascular progenitors that integrate into human fetal heart tissue. *Proc Natl Acad Sci U S A*. Feb 2013;110(9):3405-10. doi:10.1073/pnas.1220832110

33. Ardehali R, Inlay MA, Ali SR, Tang C, Drukker M, Weissman IL. Overexpression of BCL2 enhances survival of human embryonic stem cells during stress and obviates the requirement for serum factors. 10.1073/pnas.1019047108. *Proceedings of the National Academy of Sciences*. 2011;108(8):3282.

34. Kehat I, Khimovich L, Caspi O, et al. Electromechanical integration of cardiomyocytes derived from human embryonic stem cells. *Nature Biotechnology*. 09/26/online 2004;22:1282. doi:10.1038/nbt1014
https://www.nature.com/articles/nbt1014#supplementary-information

35. Rubart M, Pasumarthi KBS, Nakajima H, Soonpaa MH, Nakajima HO, Field LJ. Physiological Coupling of Donor and Host Cardiomyocytes After Cellular Transplantation. *Circulation Research*. 2003;92:1217–1224.

36. Gepstein L, Ding C, Rehemedula D, et al. In Vivo Assessment of the Electrophysiological Integration and Arrhythmogenic Risk of Myocardial Cell Transplantation Strategies. *STEM CELLS*. 2010/12/01 2010;28(12):2151-2161. doi:10.1002/stem.545

37. Efe JA, Hilcove S, Kim J, et al. Conversion of mouse fibroblasts into cardiomyocytes using a direct reprogramming strategy. *Nat Cell Biol*. Mar 2011;13(3):215-22. doi:10.1038/ncb2164

38. Fu Y, Huang C, Xu X, et al. Direct reprogramming of mouse fibroblasts into cardiomyocytes with chemical cocktails. *Cell Res*. Sep 2015;25(9):1013-24. doi:10.1038/cr.2015.99

39. Ieda M, Fu JD, Delgado-Olguin P, et al. Direct reprogramming of fibroblasts into functional cardiomyocytes by defined factors. *Cell*. Aug 6 2010;142(3):375-86. doi:10.1016/j.cell.2010.07.002

40. Jayawardena TM, Egemnazarov B, Finch EA, et al. MicroRNA-mediated in vitro and in vivo direct reprogramming of cardiac fibroblasts to cardiomyocytes. *Circ Res*. May 25 2012;110(11):1465-73. doi:10.1161/CIRCRESAHA.112.269035

41. Jayawardena T, Mirotsou M, Dzau VJ. Direct reprogramming of cardiac fibroblasts to cardiomyocytes using microRNAs. *Methods Mol Biol*. 2014;1150:263-72. doi:10.1007/978-1-4939-0512-6_18

42. Yoo J, Chang Y, Kim H, et al. Efficient Direct Lineage Reprogramming of Fibroblasts into Induced Cardiomyocytes Using Nanotopographical Cues. *J Biomed Nanotechnol*. Mar 2017;13(3):269-79. doi:10.1166/jbn.2017.2347

43. Fu JD, Srivastava D. Direct reprogramming of fibroblasts into cardiomyocytes for cardiac regenerative medicine. *Circ J*. 2015;79(2):245-54. doi:10.1253/circj.CJ-14-1372

44. Takahashi K, Yamanaka S. Induction of pluripotent stem cells from mouse embryonic and adult fibroblast cultures by defined factors. *Cell*. Aug 25 2006;126(4):663-76. doi:10.1016/j.cell.2006.07.024

45. Eschenhagen T, Bolli R, Braun T, et al. Cardiomyocyte Regeneration: A Consensus Statement. *Circulation*. Aug 15 2017;136(7):680-686. doi:10.1161/CIRCULATIONAHA.117.029343

46. Cai CL, Molkentin JD. The Elusive Progenitor Cell in Cardiac Regeneration: Slip Slidin' Away. *Circ Res*. Jan 20 2017;120(2):400-406. doi:10.1161/CIRCRESAHA.116.309710

47. Vagnozzi RJ, Molkentin JD, Houser SR. New Myocyte Formation in the Adult Heart: Endogenous Sources and Therapeutic Implications. *Circ Res*. Jul 6 2018;123(2):159-176. doi:10.1161/CIRCRESAHA.118.311208

48. Jung JH, Fu X, Yang PC. Exosomes Generated From iPSC-Derivatives: New Direction for Stem Cell Therapy in Human Heart Diseases. *Circ Res*. Jan 20 2017;120(2):407-417. doi:10.1161/CIRCRESAHA.116.309307

49. Vandergriff A, Huang K, Shen D, et al. Targeting regenerative exosomes to myocardial infarction using cardiac homing peptide. *Theranostics*. 2018;8(7):1869-1878. doi:10.7150/thno.20524

50. Barile L, Moccetti T, Marban E, Vassalli G. Roles of exosomes in cardioprotection. *Eur Heart J*. May 7 2017;38(18):1372-1379. doi:10.1093/eurheartj/ehw304

51. Gallet R, Dawkins J, Valle J, et al. Exosomes secreted by cardiosphere-derived cells reduce scarring, attenuate adverse remodelling, and improve function in acute and chronic porcine myocardial infarction. *Eur Heart J*. 01 2017;38(3):201-211. doi:10.1093/eurheartj/ehw240

52. Ibrahim AG, Cheng K, Marban E. Exosomes as critical agents of cardiac regeneration triggered by cell therapy. *Stem Cell Reports*. May 6 2014;2(5):606-19. doi:10.1016/j.stemcr.2014.04.006

53. Eulalio A, Mano M, Dal Ferro M, et al. Functional screening identifies miRNAs inducing cardiac regeneration. *Nature*. Dec 20 2012;492(7429):376-81. doi:10.1038/nature11739

54. Gabisonia K, Prosdocimo G, Aquaro GD, et al. MicroRNA therapy stimulates uncontrolled cardiac repair after myocardial infarction in pigs. *Nature*. May 2019;569(7756):418-422. doi:10.1038/s41586-019-1191-6

55. Aguirre A, Montserrat N, Zacchigna S, et al. In vivo activation of a conserved microRNA program induces mammalian heart regeneration. *Cell Stem Cell*. Nov 6 2014;15(5):589-604. doi:10.1016/j.stem.2014.10.003

56. Soonpaa MH, Koh GY, Pajak L, et al. Cyclin D1 overexpression promotes cardiomyocyte DNA synthesis and multinucleation in transgenic mice. *J Clin Invest*. Jun 1 1997;99(11):2644-54. doi:10.1172/JCI119453

57. Chaudhry HW, Dashoush NH, Tang H, et al. Cyclin A2 mediates cardiomyocyte mitosis in the postmitotic myocardium. *J Biol Chem*. Aug 20 2004;279(34):35858-66. doi:10.1074/jbc.M404975200

58. Cheng RK, Asai T, Tang H, et al. Cyclin A2 induces cardiac regeneration after myocardial infarction and prevents heart failure. *Circ Res*. Jun 22 2007;100(12):1741-8. doi:10.1161/CIRCRESAHA.107.153544

59. Shapiro SD, Ranjan AK, Kawase Y, et al. Cyclin A2 induces cardiac regeneration after myocardial infarction through cytokinesis of adult cardiomyocytes. *Sci Transl Med*. Feb 19 2014;6(224):224ra27. doi:10.1126/scitranslmed.3007668

60. Mohamed TMA, Ang YS, Radzinsky E, et al. Regulation of Cell Cycle to Stimulate Adult Cardiomyocyte Proliferation and Cardiac Regeneration. *Cell*. Mar 22 2018;173(1):104-116 e12. doi:10.1016/j.cell.2018.02.014

61. Mahmoud AI, Kocabas F, Muralidhar SA, et al. Meis1 regulates postnatal cardiomyocyte cell cycle arrest. *Nature*. May 9 2013;497(7448):249-253. doi:10.1038/nature12054

62. Wei K, Serpooshan V, Hurtado C, et al. Epicardial FSTL1 reconstitution regenerates the adult mammalian heart. *Nature*. Sep 24 2015;525(7570):479-85. doi:10.1038/nature15372

63. Bersell K, Arab S, Haring B, Kuhn B. Neuregulin1/ErbB4 signaling induces cardiomyocyte proliferation and repair of heart injury. *Cell*. Jul 23 2009;138(2):257-70. doi:10.1016/j.cell.2009.04.060

64. D'Uva G, Aharonov A, Lauriola M, et al. ERBB2 triggers mammalian heart regeneration by promoting cardiomyocyte dedifferentiation and proliferation. *Nat Cell Biol*. May 2015;17(5):627-38. doi:10.1038/ncb3149

65. Cluzeaut F, Maurer-Schultze B. Proliferation of cardiomyocytes and interstitial cells in the cardiac muscle of the mouse during pre- and postnatal development. *Cell Tissue Kinet*. May 1986;19(3):267-74. doi:10.1111/j.1365-2184.1986.tb00679.x

66. Manasek FJ. Mitosis in developing cardiac muscle. *J Cell Biol*. Apr 1968;37(1):191-6. doi:10.1083/jcb.37.1.191

67. Porrello ER, Mahmoud AI, Simpson E, et al. Transient regenerative potential of the neonatal mouse heart. *Science*. Feb 25 2011;331(6020):1078-80. doi:10.1126/science.1200708

68. Bader D, Oberpriller JO. Repair and reorganization of minced cardiac muscle in the adult newt (Notophthalmus viridescens). *J Morphol*. Mar 1978;155(3):349-57. doi:10.1002/jmor.1051550307

69. Poss KD, Wilson LG, Keating MT. Heart regeneration in zebrafish. *Science*. Dec 13 2002;298(5601):2188-90. doi:10.1126/science.1077857

70. Bergmann O, Bhardwaj RD, Bernard S, et al. Evidence for cardiomyocyte renewal in humans. *Science*. Apr 3 2009;324(5923):98-102. doi:10.1126/science.1164680 324/5923/98 [pii]

71. Conese M, Carbone A, Beccia E, Angiolillo A. The Fountain of Youth: A Tale of Parabiosis, Stem Cells, and Rejuvenation. *Open Med (Wars)*. 2017;12:376-383. doi:10.1515/med-2017-0053

72. McCay C. Clive McCay Papers, 1920-1967. Division of Rare and Manuscript Collections. Accessed February 9, 2021. https://rmc.library.cornell.edu/EAD/htmldocs/RMA01087.html

73. Conboy IM, Conboy MJ, Wagers AJ, Girma ER, Weissman IL, Rando TA. Rejuvenation of aged progenitor cells by exposure to a young systemic environment. 10.1038/nature03260. *Nature*. 02/17/print 2005;433(7027):760-764. doi:http://www.nature.com/nature/journal/v433/n7027/suppinfo/nature03260_S1.html

74. Sinha M, Jang YC, Oh J, et al. Restoring systemic GDF11 levels reverses age-related dysfunction in mouse skeletal muscle. *Science (New York, NY)*. 05/05 2014;344(6184):649-652. doi:10.1126/science.1251152

75. Katsimpardi L, Litterman NK, Schein PA, et al. Vascular and neurogenic rejuvenation of the aging mouse brain by young systemic factors. *Science (New York, NY)*. 05/05 2014;344(6184):630-634. doi:10.1126/science.1251141

76. Villeda SA, Luo J, Mosher KI, et al. The aging systemic milieu negatively regulates neurogenesis and cognitive function. *Nature*. 08/31 2011;477(7362):90-94. doi:10.1038/nature10357

77. Loffredo FS, Steinhauser ML, Jay SM, et al. Growth Differentiation Factor 11 is a Circulating Factor that Reverses Age-Related Cardiac Hypertrophy. *Cell*. 2013;153(4):828-839. doi:10.1016/j.cell.2013.04.015

78. Senyo SE, Steinhauser ML, Pizzimenti CL, et al. Mammalian heart renewal by pre-existing cardiomyocytes. *Nature*. Jan 17 2013;493(7432):433-6. doi:10.1038/nature11682

nature11682 [pii]

79. Ali SR, Hippenmeyer S, Saadat LV, Luo L, Weissman IL, Ardehali R. Existing cardiomyocytes generate cardiomyocytes at a low rate after birth in mice. *Proceedings of the National Academy of Sciences of the United States of America*. 05/29 2014;111(24):8850-8855. doi:10.1073/pnas.1408233111

80. Kimura W, Xiao F, Canseco DC, et al. Hypoxia fate mapping identifies cycling cardiomyocytes in the adult heart. *Nature*. Jul 9 2015;523(7559):226-30. doi:10.1038/nature14582
nature14582 [pii]

81. Sturzu AC, Rajarajan K, Passer D, et al. Fetal Mammalian Heart Generates a Robust Compensatory Response to Cell Loss. *Circulation*. Jul 14 2015;132(2):109-21. doi:10.1161/CIRCULATIONAHA.114.011490
CIRCULATIONAHA.114.011490 [pii]

82. Stanley EG, Biben C Fau - Elefanty A, Elefanty A Fau - Barnett L, et al. Efficient Cre-mediated deletion in cardiac progenitor cells conferred by a 3'UTR-ires-Cre allele of the homeobox gene Nkx2-5. 20020726 DCOM- 20030226 (0214-6282 (Print))

83. Sung K, Ding Y, Ma J, et al. Simplified three-dimensional tissue clearing and incorporation of colorimetric phenotyping. *Scientific Reports*. 08/08 04/27/received
07/04/accepted 2016;6:30736. doi:10.1038/srep30736

84. Schindelin J, Arganda-Carreras I, Frise E, et al. Fiji - an Open Source platform for biological image analysis. *Nature methods*. 06/28 2012;9(7):10.1038/nmeth.2019. doi:10.1038/nmeth.2019

85. Thevenaz P, Ruttimann UE, Unser M. A pyramid approach to subpixel registration based on intensity. *IEEE Trans Image Process*. 1998;7(1):27-41.

86. Wu J, Anczuków O, Krainer AR, Zhang MQ, Zhang C. OLego: fast and sensitive mapping of spliced mRNA-Seq reads using small seeds. *Nucleic Acids Research*. 2013;41(10):5149-5163.

87. Liao Y, Smyth GK, Shi W. featureCounts: an efficient general purpose program for assigning sequence reads to genomic features. *Bioinformatics*. 2013;30(7):923-930. doi:10.1093/bioinformatics/btt656

88. Sahoo D, Dill DL, Tibshirani R, Plevritis SK. Extracting binary signals from microarray time-course data. *Nucleic Acids Research*. 2007;35(11):3705-3712.

89. Saga Y, Miyagawa-Tomita S, Takagi A, Kitajima S, Miyazaki Ji, Inoue T. MesP1 is expressed in the heart precursor cells and required for the formation of a single heart tube. *Development*. 1999;126(15):3437-3447.

90. Wu SM, Fujiwara Y, Cibulsky SM, et al. Developmental Origin of a Bipotential Myocardial and Smooth Muscle Cell Precursor in the Mammalian Heart. *Cell*. 2006;127(6):1137-1150.

91. Molkentin JD, Jobe SM, Markham BE. α-myosin Heavy Chain Gene Regulation: Delineation and Characterization of the Cardiac Muscle-specific Enhancer and Muscle-specific Promoter. *Journal of Molecular and Cellular Cardiology*. 1996;28(6):1211-1225.

92. Hirai M, Chen J, Evans SM. Tissue-Specific Cell Cycle Indicator Reveals Unexpected Findings for Cardiac Myocyte Proliferation. *Circ Res*. Oct 15 2015;doi:CIRCRESAHA.115.307697 [pii] 10.1161/CIRCRESAHA.115.307697

93. Soonpaa Mark H, Zebrowski David C, Platt C, Rosenzweig A, Engel Felix B, Field Loren J. Cardiomyocyte Cell-Cycle Activity during Preadolescence. *Cell*. 163(4):781-782. doi:10.1016/j.cell.2015.10.037

94. Alkass K, Panula J, Westman M, Wu T-D, Guerquin-Kern J-L, Bergmann O. No Evidence for Cardiomyocyte Number Expansion in Preadolescent Mice. *Cell*. 163(4):1026-1036. doi:10.1016/j.cell.2015.10.035

95. Chung K, Wallace J, Kim S-Y, et al. Structural and molecular interrogation of intact biological systems. Article. *Nature*. 05/16/print 2013;497(7449):332-337. doi:10.1038/nature12107 http://www.nature.com/nature/journal/v497/n7449/abs/nature12107.html#supplementary-information

96. Bersell K, Arab S, Haring B, Kühn B. Neuregulin1/ErbB4 Signaling Induces Cardiomyocyte Proliferation and Repair of Heart Injury. *Cell*. 2009;138(2):257-270.

97. Naqvi N, Li M, Calvert JW, et al. A Proliferative Burst During Preadolescence Establishes the Final Cardiomyocyte Number. *Cell*. 2014;157(4):795-807. doi:10.1016/j.cell.2014.03.035

98. Alkass K, Panula J, Westman M, Wu T-D, Guerquin-Kern J-L, Bergmann O. No Evidence for Cardiomyocyte Number Expansion in Preadolescent Mice. *Cell*. 11/5/ 2015;163(4):1026-1036. doi:http://dx.doi.org/10.1016/j.cell.2015.10.035

99. Dettman RW, Denetclaw Jr W, Ordahl CP, Bristow J. Common Epicardial Origin of Coronary Vascular Smooth Muscle, Perivascular Fibroblasts, and Intermyocardial Fibroblasts in the Avian Heart. *Developmental Biology*. 1998;193(2):169-181.

100. Zhou B, Ma Q, Rajagopal S, et al. Epicardial progenitors contribute to the cardiomyocyte lineage in the developing heart. 10.1038/nature07060. *Nature*. 2008;454(7200):109-113.

101. Porrello ER, Mahmoud AI, Simpson E, et al. Transient Regenerative Potential of the Neonatal Mouse Heart. *Science*. February 25, 2011 2011;331(6020):1078-1080.

102. Porrello ER, Mahmoud AI, Simpson E, et al. Regulation of neonatal and adult mammalian heart regeneration by the miR-15 family. *Proceedings of the National Academy of Sciences*. 2013;110(1):187-192.

103. Drenckhahn J-D, Schwarz QP, Gray S, et al. Compensatory Growth of Healthy Cardiac Cells in the Presence of Diseased Cells Restores Tissue Homeostasis during Heart Development. *Developmental Cell*. 2008;15(4):521-533.

104. Acharya S, Sahoo SK. PLGA nanoparticles containing various anticancer agents and tumour delivery by EPR effect. *Advanced Drug Delivery Reviews*. 2011/03/18/ 2011;63(3):170-183. doi:https://doi.org/10.1016/j.addr.2010.10.008

105. Peres C, Matos AI, Conniot J, et al. Poly(lactic acid)-based particulate systems are promising tools for immune modulation. *Acta Biomaterialia*. 2017/01/15/ 2017;48(Supplement C):41-57. doi:https://doi.org/10.1016/j.actbio.2016.11.012

106. Kamaly N, Xiao Z, Valencia PM, Radovic-Moreno AF, Farokhzad OC. Targeted polymeric therapeutic nanoparticles: design, development and clinical translation. 10.1039/C2CS15344K. *Chemical Society Reviews*. 2012;41(7):2971-3010. doi:10.1039/C2CS15344K

107. Locatelli E, Comes-Franchini M. *Biodegradable PLGA-b-PEG polymeric nanoparticles: Synthesis, properties, and nanomedical applications as drug delivery system*. vol 14. 2012.

108. Ratzinger G, Agrawal P, Körner W, et al. Surface modification of PLGA nanospheres with Gd-DTPA and Gd-DOTA for high-relaxivity MRI contrast agents. *Biomaterials*. 2010/11/01/ 2010;31(33):8716-8723. doi:https://doi.org/10.1016/j.biomaterials.2010.07.095

109. Panyam J, Zhou W-Z, Prabha S, Sahoo SK, Labhasetwar V. Rapid endo-lysosomal escape of poly(dl-lactide-co-glycolide) nanoparticles: implications for drug and gene delivery. *The FASEB Journal*. 2002;16(10):1217-1226.

110. Kocbek P, Obermajer N, Cegnar M, Kos J, Kristl J. Targeting cancer cells using PLGA nanoparticles surface modified with monoclonal antibody. *Journal of Controlled Release*. 2007/07/13/ 2007;120(1):18-26. doi:https://doi.org/10.1016/j.jconrel.2007.03.012

111. Hans ML, Lowman AM. Biodegradable nanoparticles for drug delivery and targeting. *Current Opinion in Solid State and Materials Science*. 2002/08/01/ 2002;6(4):319-327. doi:https://doi.org/10.1016/S1359-0286(02)00117-1

112. Gref R, Minamitake Y, Peracchia MT, Trubetskoy V, Torchilin V, Langer R. Biodegradable long-circulating polymeric nanospheres. 10.1126/science.8128245. *Science*. 1994;263(5153):1600.

113. Li Y-P, Pei Y-Y, Zhang X-Y, et al. PEGylated PLGA nanoparticles as protein carriers: synthesis, preparation and biodistribution in rats. *Journal of Controlled Release*. 2001/04/02/ 2001;71(2):203-211. doi:https://doi.org/10.1016/S0168-3659(01)00218-8

114. Avgoustakis K, Beletsi A, Panagi Z, et al. Effect of copolymer composition on the physicochemical characteristics, in vitro stability, and biodistribution of PLGA–mPEG nanoparticles. *International Journal of Pharmaceutics*. 2003/06/18/ 2003;259(1):115-127. doi:https://doi.org/10.1016/S0378-5173(03)00224-2

115. F Zambaux M, Bonneaux F, Gref R, Dellacherie E, Vigneron C. *MPEO-PLA nanoparticles: Effect of MPEO content on some of their surface properties*. vol 44. 1999:109-15.

116. Karra N, Nassar T, Ripin A, Schwob O, Borlak J, Benita S. Antibody Conjugated PLGA Nanoparticles for Targeted Delivery of Paclitaxel Palmitate: Efficacy and Biofate in a Lung Cancer Mouse Model. *Small*. 2013;(9):4221–4236.

117. Yang J, Lee C-H, Park J, et al. Antibody conjugated magnetic PLGA nanoparticles for diagnosis and treatment of breast cancer. 10.1039/B702538F. *Journal of Materials Chemistry*. 2007;17(26):2695-2699. doi:10.1039/B702538F

118. Zhang N, Chittapuso C, Ampassavate C, Siahaan TJ, Berkland C. PLGA Nanoparticle-Peptide Conjugate Effectively Targets Intercellular Cell-Adhesion Molecule-1. *Bioconjugate chemistry*. 11/13 2008;19(1):145-152. doi:10.1021/bc700227z

119. Vasconcelos A, Vega E, Pérez Y, Gómara MJ, García ML, Haro I. Conjugation of cell-penetrating peptides with poly(lactic-co-glycolic acid)-polyethylene glycol nanoparticles improves ocular drug delivery. *International Journal of Nanomedicine*. 01/27 2015;10:609-631. doi:10.2147/IJN.S71198

120. Mathew A, Fukuda T, Nagaoka Y, et al. Curcumin Loaded-PLGA Nanoparticles Conjugated with Tet-1 Peptide for Potential Use in Alzheimer's Disease. *PLoS ONE*. 03/05 09/28/received
01/31/accepted 2012;7(3):e32616. doi:10.1371/journal.pone.0032616

121. Jain SK, Gupta Y, Ramalingam L, et al. Lactose-Conjugated PLGA Nanoparticles for Enhanced Delivery of Rifampicin to the Lung for Effective Treatment of Pulmonary Tuberculosis. *PDA Journal of Pharmaceutical Science and Technology*. 2010;64(3):278-287.

122. Yin Y, Chen D, Qiao M, Lu Z, Hu H. Preparation and evaluation of lectin-conjugated PLGA nanoparticles for oral delivery of thymopentin. *Journal of Controlled Release*. 2006/12/01/ 2006;116(3):337-345. doi:https://doi.org/10.1016/j.jconrel.2006.09.015

123. Anselmo AC, Mitragotri S. Nanoparticles in the clinic. *Bioengineering & Translational Medicine*. 2016;1(1):10-29. doi:10.1002/btm2.10003

124. Lynch I, Dawson KA. Protein-nanoparticle interactions. *Nano Today*. 2008/02/01/ 2008;3(1):40-47. doi:https://doi.org/10.1016/S1748-0132(08)70014-8

125. Cedervall T, Lynch I, Lindman S, et al. Understanding the nanoparticle–protein corona using methods to quantify exchange rates and affinities of proteins for nanoparticles. 10.1073/pnas.0608582104. *Proceedings of the National Academy of Sciences*. 2007;104(7):2050.

126. Monopoli MP, Åberg C, Salvati A, Dawson KA. Biomolecular coronas provide the biological identity of nanosized materials. Review Article. *Nature Nanotechnology*. 12/05/online 2012;7:779. doi:10.1038/nnano.2012.207

127. Nguyen VH, Lee B-J. Protein corona: a new approach for nanomedicine design. *International Journal of Nanomedicine*. 04/18 2017;12:3137-3151. doi:10.2147/IJN.S129300

128. Conboy IM, Conboy MJ, Smythe GM, Rando TA. Notch-mediated restoration of regenerative potential to aged muscle. *Science*. Nov 28 2003;302(5650):1575-7. doi:10.1126/science.1087573

129. Fuller J. Hematopoietic stem cells and aging. *Sci Aging Knowledge Environ*. Jun 26 2002;2002(25):pe11. doi:10.1126/sageke.2002.25.pe11

130. Sigal SH, Brill S, Fiorino AS, Reid LM. The liver as a stem cell and lineage system. *Am J Physiol*. Aug 1992;263(2 Pt 1):G139-48. doi:10.1152/ajpgi.1992.263.2.G139

131. Kuhn HG, Dickinson-Anson H, Gage FH. Neurogenesis in the dentate gyrus of the adult rat: age-related decrease of neuronal progenitor proliferation. *J Neurosci*. Mar 15 1996;16(6):2027-33.

132. Morrison SJ, Wandycz AM, Akashi K, Globerson A, Weissman IL. The aging of hematopoietic stem cells. *Nat Med*. Sep 1996;2(9):1011-6. doi:10.1038/nm0996-1011

133. Fuchs E, Blau HM. Tissue Stem Cells: Architects of Their Niches. *Cell Stem Cell*. Oct 1 2020;27(4):532-556. doi:10.1016/j.stem.2020.09.011

134. Yutzey KE. Cardiomyocyte Proliferation: Teaching an Old Dogma New Tricks. *Circ Res*. Feb 17 2017;120(4):627-629. doi:10.1161/CIRCRESAHA.116.310058

135. He L, Nguyen NB, Ardehali R, Zhou B. Heart Regeneration by Endogenous Stem Cells and Cardiomyocyte Proliferation: Controversy, Fallacy, and Progress. *Circulation*. Jul 21 2020;142(3):275-291. doi:10.1161/CIRCULATIONAHA.119.045566

136. Dennis M, Spiegler BJ, Juranek JJ, Bigler ED, Snead OC, Fletcher JM. Age, plasticity, and homeostasis in childhood brain disorders. *Neurosci Biobehav Rev*. Dec 2013;37(10 Pt 2):2760-73. doi:10.1016/j.neubiorev.2013.09.010

137. Villeda SA, Luo J, Mosher KI, et al. The ageing systemic milieu negatively regulates neurogenesis and cognitive function. *Nature*. 08/31/online 2011;477:90. doi:10.1038/nature10357
https://www.nature.com/articles/nature10357#supplementary-information

138. Villeda SA, Plambeck KE, Middeldorp J, et al. Young blood reverses age-related impairments in cognitive function and synaptic plasticity in mice. Letter. *Nat Med*. 06//print 2014;20(6):659-663. doi:10.1038/nm.3569
http://www.nature.com/nm/journal/v20/n6/abs/nm.3569.html#supplementary-information

139. Baruch K, Deczkowska A, David E, et al. Aging. Aging-induced type I interferon signaling at the choroid plexus negatively affects brain function. *Science (New York, NY)*. 08/21 2014;346(6205):89-93. doi:10.1126/science.1252945

140. Castellano JM, Mosher KI, Abbey RJ, et al. Human umbilical cord plasma proteins revitalize hippocampal function in aged mice. *Nature*. 04/19 2017;544(7651):488-492. doi:10.1038/nature22067

141. Ruckh JM, Zhao J-W, Shadrach JL, et al. Rejuvenation of regeneration in the aging central nervous system. *Cell stem cell*. 2012;10(1):96-103. doi:10.1016/j.stem.2011.11.019

142. Schneider CA, Rasband WS, Eliceiri KW. NIH Image to ImageJ: 25 years of image analysis. *Nat Methods*. Jul 2012;9(7):671-5. doi:10.1038/nmeth.2089

143. Zhou Y, Zhou B, Pache L, et al. Metascape provides a biologist-oriented resource for the analysis of systems-level datasets. *Nat Commun*. 04 2019;10(1):1523. doi:10.1038/s41467-019-09234-6

144. Yang YR, Kabir MH, Park JH, et al. Plasma proteomic profiling of young and old mice reveals cadherin-13 prevents age-related bone loss. *Aging (Albany NY)*. May 12 2020;12(9):8652-8668. doi:10.18632/aging.103184

145. Cardoso-Moreira M, Halbert J, Valloton D, et al. Gene expression across mammalian organ development. *Nature*. 2019/07/01 2019;571(7766):505-509. doi:10.1038/s41586-019-1338-5

146. Wang X, Guo Z, Ding Z, Mehta JL. Inflammation, Autophagy, and Apoptosis After Myocardial Infarction. *J Am Heart Assoc*. Apr 21 2018;7(9)doi:10.1161/JAHA.117.008024

147. Thapa P, Farber DL. The Role of the Thymus in the Immune Response. *Thorac Surg Clin*. May 2019;29(2):123-131. doi:10.1016/j.thorsurg.2018.12.001

148. Hinkel R, Klett K, Bahr A, Kupatt C. Thymosin beta4-mediated protective effects in the heart. *Expert Opin Biol Ther*. Jul 2018;18(sup1):121-129. doi:10.1080/14712598.2018.1490409

149. Banerjee I, Zhang J, Moore-Morris T, et al. Thymosin beta 4 is dispensable for murine cardiac development and function. *Circ Res*. Feb 3 2012;110(3):456-64. doi:10.1161/CIRCRESAHA.111.258616

150. Pipes GT, Yang J. Cardioprotection by Thymosin Beta 4. *Vitam Horm*. 2016;102:209-26. doi:10.1016/bs.vh.2016.04.004

151. Haynes BF, Markert ML, Sempowski GD, Patel DD, Hale LP. The role of the thymus in immune reconstitution in aging, bone marrow transplantation, and HIV-1 infection. *Annu Rev Immunol*. 2000;18:529-60. doi:10.1146/annurev.immunol.18.1.529

152. Cannavo A, Rengo G, Liccardo D, et al. Prothymosin alpha protects cardiomyocytes against ischemia-induced apoptosis via preservation of Akt activation. *Apoptosis*. Oct 2013;18(10):1252-61. doi:10.1007/s10495-013-0876-9

153. Madhunapantula SV, Mosca PJ, Robertson GP. The Akt signaling pathway: an emerging therapeutic target in malignant melanoma. *Cancer Biol Ther*. Dec 15 2011;12(12):1032-49. doi:10.4161/cbt.12.12.18442